UNIVERSITÁ DEGLI STUDI DI TRIESTE

XXXI CICLO DEL DOTTORATO DI RICERCA IN FISICA

DOCTORAL THESIS

Combined tumour treatment by coupling conventional radiotherapy to an additional dose contribution from thermal neutrons

Academic discipline: Fisica Nucleare e Subnucleare

Ph.D. Student:
Katia ALIKANIOTIS

Ph.D. Coordinator:
Prof. Livio LANCERI

Thesis Supervisor:
Prof. Gianrossano GIANNINI

Thesis co-Supervisor:
Prof. Francesco LONGO

ACADEMIC YEAR 2017/2018

UNIVERSITÁ DEGLI STUDI DI TRIESTE

XXXI CICLO DEL DOTTORATO DI RICERCA IN FISICA

DOCTORAL THESIS

Combined tumour treatment by coupling conventional radiotherapy to an additional dose contribution from thermal neutrons

---

Academic discipline: Fisica Nucleare e Subnucleare

Ph.D. Student:
Katia ALIKANIOTIS

Ph.D. Coordinator:
Prof. Livio LANCERI

Thesis Supervisor:
Prof. Gianrossano GIANNINI

Thesis co-Supervisor:
Prof. Francesco LONGO

ACADEMIC YEAR 2017/2018

"Dedicato ai miei genitori, a mio fratello, alla mia nonna,
e al mio caro nonno che non c'e' piu'. "

UNIVERSITÁ DEGLI STUDI DI TRIESTE
XXXI CICLO DEL DOTTORATO DI RICERCA IN FISICA

Doctoral Thesis

Abstract

Combined tumour treatment by coupling conventional radiotherapy to an additional dose contribution from thermal neutrons

by Katia ALIKANIOTIS

Aim: To employ the thermal neutron background in conventional X-rays radiotherapy treatments in order to add a localized neutron dose boost to the patient, enhancing the treatment effectiveness.

Background: Conventional linear accelerators for radiotherapy produce fast secondary neutrons with a mean energy of about 1 MeV due to (γ, n) reaction. This neutron field, isotropically distributed, is considered as an extra unaccounted dose during the treatment. Moreover, considering the moderating effect of human body, a thermal neutron field is localized in the tumour area: this neutron background could be employed for Boron Neutron Capture Therapy (BNCT) by previously administering a boron (^{10}B enriched) carrier to the patient, acting as a localized radiosensitizer. The thermal neutron absorption in the ^{10}B enriched tissue will improve radiotherapy effectiveness.

Materials and Methods: The feasibility of the proposed method was investigated by using simplified tissue-equivalent phantoms with cavities in correspondence of relevant tissues or organs, suited for dosimetric measurements. A 10 cm $\times$ 10 cm square photon field with different energies was delivered to the phantoms. Additional exposures were implemented, using a compact neutron photo-converter-moderator assembly, with the purpose of modifying the mixed photon-neutron field in the treatment region. Doses due to photons and neutrons were both measured by using radiochromic films and superheated bubble detectors, respectively, and simulated with Monte Carlo codes.

Results: For a 10 cm $\times$ 10 cm square photon field with accelerating potentials 6 MV, 10 MV and 15 MV, the neutron dose equivalent in phantom was measured and its values was 0.07 mGy/Gy (neutron dose equivalent / photon absorbed dose at isocentre), 0.99 mGy/Gy and 2.22 mGy/Gy, respectively.
For a 18 MV treatment, simulations and measurements quantified the thermal neutron field in the treatment zone in 1.55×10^7 cm^{-2} Gy^{-1}. Assuming a BNCT-standard ^{10}B concentration in tumour tissue, the calculated additional BNCT dose at 4 cm depth in phantom would be 1.5 mGy-eq/Gy. This ratio would reach 43 mGy-eq/Gy for an intensity modulated radiotherapy treatment (IMRT).
When a specifically designed compact neutron photo-converter-moderator assembly is applied to the LINAC to enhance the thermal neutron field, the photon field is modified. Particularly, a 15 MV photon field produces a dose profile very similar to that would be produced by a 6 MV field in absence of the photo-converter-moderator assembly. As far as the thermal neutron field is concerned, more thermal neutrons are present, and thermal neutrons per photon increase of a factor 3 to 12 according to the depth in phantom and to different photoconverter geometries. By contrast, the photo-converter-moderator assembly was found to reduce fast neutrons of a factor 16 in the direction of the incident beam.

Conclusions: The parasitic thermal neutron component during conventional high-energy radiotherapy could be exploited to produce additional therapeutic doses if the ^{10}B-carrier was administered to the patient. This radiosensitization effect could be increased by modifying the treatment field by using the specifically designed neutron photo-converter-moderator assembly.

Acknowledgements

A conclusione di questo ciclo di studi di Dottorato sento il dovere e il piacere di ringraziare tutti coloro che mi hanno sostenuto e accompagnato durante questo percorso con i loro consigli, la loro saggezza e il loro affetto.

Il mio supervisore per avermi dato la possibilita' e la spinta di condurre un percorso di studi e ricerca in proseguimento agli anni di laurea.

Il mio co-supervisore per essere stato anche un amico, dandomi consigli quando credevo di non farcela.

La dottoressa Mara Severgnini, sempre gentile e disponibile nel permettermi di effettuare le misure sperimentali in ospedale anche dopo l'orario lavorativo o di sabato.

Lo staff dell'officina, non solo per aver contribuito alla realizzazione della parte sperimentale del lavoro, ma anche per le lunghe chiaccherate e il fatto di esserci quando avevo bisogno di aiuto nella vita quotidiana. Soprattutto grazie a Stefano e la moglie Elena, che sono diventati i miei genitori triestini.

Non potro' mai dimenticare gli appuntamenti del mercoledi' a pranzo all'ICTP e quelli del giovedi' in Area di Ricerca con tutti i miei colleghi-amici.

Un grazie speciale a Laura, che e' stata con me ogni giorno in questi tre anni, e a Valeria, che dalla laurea magistrale rimane la mia compagna di viaggi di studio e lavoro, ai miei amici della piscina e della ginnastica per lo svago serale post-lavorativo, in particolare a Chiaretta con cui si e' creato un forte legame.

...mi avete ben accolto a Trieste e fatto sentire in famiglia.

Grazie alla mia famiglia che continua a credere in me, a sostenermi in ogni mia decisione e a starmi vicino.

Infine, vorrei ringraziare anche i miei revisori, che con molto impegno e dedizione hanno letto ogni singola parola scritta in questa lunga tesi.

Grazie di cuore a tutti,

Katia

Contents

List of Figures

List of Tables

List of Abbreviations

3D-CRT	**3** **D**imensional - **C**onformal **R**adiation **T**herapy
BBB	**B**lood **B**rain **B**arrier
BDT	**B**ubble **D**etector for **T**hermal neutrons
BD-PND	**B**ubble **D**etector - **P**ersonal **N**eutron **D**osimeter
BNCT	**B**oron **N**eutron **C**apture **T**herapy
BPA	**B**oron **P**henyl **A**lanine
BTI	**B**ubble **T**echnology **I**ndustries
DNA	**D**eoxyribo**N**ucleic **A**cid
DSB	**D**ouble **S**trand **B**reak
GDR	**G**iant **D**ipole **R**esonance
GEANT	**GE**ometry **AN**d **T**racking
e-LiBANS	**e**lectron **Li**NAC **B**ased **A**ctively monitored **N**eutron **S**ource
ICRP	**I**nternational **C**ommission on **R**adiological **P**rotection
ICRU	**I**nternational **C**ommission on **R**adiation **U**nits and Measurements
IMRT	**I**ntensity **M**odulated **R**adiation **T**herapy
INFN	**I**stituto **N**azionale di **F**isica **N**ucleare (National Institute of Nuclear Physics)
LET	**L**inear **E**nergy **T**ransfer
LINAC	**LIN**ear **AC**celerator
LNT	**L**inear **N**on**T**hreshold model
LQ	**L**inear **Q**uadratic model
MCNP	**M**onte **C**arlo **N**-**P**article
MLC	**M**ulti**L**eaf **C**ollimator
MU	**M**onitor **U**nits
PDD	**P**ercentage **D**epth **D**ose
PhoNeS	**Pho**to **Ne**utron **S**ource

RBE	**R**elative **B**iological **E**ffectiveness
RGB	**R**ed **G**reen **B**lue
ROI	**R**egion **O**f **I**nterest
ROS	**R**eactive **O**xygen **S**pecies
SSB	**S**ingle **S**trand **B**reak
SSD	**S**ource to **S**urface **D**istance
TPR	**T**issue **P**hantom **R**atio
TMR	**T**issue **M**aximum **R**atio
VMAT	**V**olumetric **M**odulatec **A**rc **T**herapy

List of Symbols

Am	Americium nucleus
B	Boron nucleus
Be	Beryllium nucleus
C	Carbon nucleus
Ca	Calcium nucleus
Co	Cobalt nucleus
H	Hydrogen nucleus
He	Helium nucleus
I	Iodine nucleus
Ir	Iridium nucleus
Li	Lithium nucleus
N	Nitrogen nucleus
O	Oxygen nucleus
P	Phosphorus nucleus

w_R	Radiation weighting factor
w_T	Tissue weighting factor

D	Absorbed dose	[Gy] = [joule/kg]
E	Effective dose	[Sv] = [joule/kg]
H_T	Equivalent dose	[Sv] = [joule/kg]

Introduction

Three are the methods to fight cancer, namely surgery, chemotherapy and radiotherapy. Although these treatment modalities are generally used in combination, almost two-thirds of cancer patients (that is more than 15 millions per year, worldwide) receive some form of radiation therapy during their treatment. Considering the ten most frequent cancer pathologies (prostate, female breast, lung, colorectal, bladder, non-Hodgkin lymphoma, skin melanoma, kidney, ovarian, and uterine), it has been estimated that at least 50% of them are treated with radiotherapy as a part or the totality of the treatment. Although the number of patients treated with protons or carbon ions is increasing (from 8000 patients worldwide in 2007 to 20000 in 2016), the conventional radiotherapy with electron linear accelerators (LINACs) still remains the option for the large majority of these patients.

Thanks to modern treatment techniques (IMRT, tomotherapy, VMAT...), the effectiveness of conventional radiotherapy improved in last two decades. However, there are still tumours with high fatality rate. This is the case of the Glioblastoma Multiforme, characterized by high radioresistance and extensive hypoxia, for which only 27% of the patients are expected to survive more than two years [1]. Consequently, the need exists for alternative treatment modalities and new radiosensitizers, "intended to enhance tumour cell killing while having much less effect on normal tissues" (deterministic or second cancers) [2].

Boron Neutron Capture Therapy (BNCT) is a highly selective radiotherapy [3]. BNCT selectively targets tumour cells with high-LET (LET = Linear Energy Transfer) heavy charged particles. The conditions to achieve this selective treatment are:

- Load the tumour tissue with a ^{10}B-rich compound, also called tumour-seeking compound, usually 10-Boron-Phenyl-Alanine, ^{10}BPA.
- Expose the tissue to a thermal neutron field.

Due to the very large ^{10}B(n, α)^{7}Li neutron capture cross section at slow energies (3843 barns at 0.025 eV) [4], the tumour tissue will be exposed to a field of α particles (energy 1.5 MeV) and ^{7}Li nuclei (0.8 MeV). Owing on the short range in tissue, comparable with the cell size, these particles selectively destroy tumour cells [5].

BNCT is usually performed at dedicated facilities like nuclear reactors or ^{7}Li(p, n)^{7}Be based particle accelerators, not in conventional medical electron LINACs. Nevertheless, the parasitic neutron field produced in these machines (when operating at 10 MV or more) could be used to deliver a BNCT-boost to the tumour, in addition and simultaneously, to the conventional treatment.

Photo-neutrons, produced in medical LINACs through giant dipole resonance (GDR) γ-n reactions, are a parasitic effect in conventional radiotherapy, as they expose the patient to an extra neutron dose, potentially leading to second cancers [6].

The photo-neutron field, especially generated in heavy elements (such as lead, tungsten, iron) in the LINAC target and surrounding materials, is almost isotropically produced at an average energy of about 1 MeV [7]. Due to the moderation effect of the patient [8], a large fraction of these neutrons get thermalized before reaching internal organs/tissues.

If this neutron field was adequately shaped in intensity and spatial distribution, and a ^{10}B-carrier was administered to the patient, an additional BNCT therapeutic dose could be delivered in addition to the therapeutic photons. BNCT could thus act as a localized radiosensitizer, improving the radiotherapy effectiveness.

The subject of this research work, developed in the framework of the INFN e-LiBANS project, is to study this in-phantom neutron field and possible field modifications, oriented to improve the thermal field at the tumour place. The work includes a numerical part, aimed at simulating the in-phantom field and dosimetric quantities, as well as an experimental one, where in-phantom measurements were performed by using photon (radiochromic films) and neutron (superheated drop dosimeters) detectors.

The chapters from 1 to 6 give basic elements of radiotherapy, radiobiology, BNCT, cancer radiosensitizers, medical linear accelerators and neutron contamination in radiotherapy.
Chapters 7 and 8 describes the experimental and computational framework.
Chapter 9 report neutron measurements performed in a radiotherapy treatment room by using a tissue-equivalent anthropomorphic phantom.
Chapter 10 describes, via MCNP simulations, the potential BNCT dose contribution in a direct single-field conventional radiotherapy treatment.
Chapter 11 treats the case of a simplified photon/neutron treatment, where the radiation field was modified with a compact neutron photo-converter-moderator assembly (device specially designed to improve the thermal field in the treatment region, without compromising the therapeutic photon beam).

Chapter 1

Cancer treatment techniques

The meaning of the word *cancer* refers to an abnormal growth of cells which tend to proliferate in an uncontrolled way and, in some cases, to metastasize. Cancer can involve any tissue of the body and have many different forms in each body area.
Cancer is not one disease: it is a group of more than 100 different and distinctive diseases, named in different ways based on the type of cell or organ in which it starts.

Giving a brief biological introduction, in normal cells the cell cycle (2.2.1) is tightly regulated by a number of proteins. However, if a critical number of DNA mutations in the corresponding genes has accumulated in a single cell, these control mechanisms can fail. The resulting cancer cells usually proliferate at a much higher rate and have lost the ability to eliminate themselves by apoptosis. They take up nutrients and space that normal cells need. This uncontrolled growth can damage tissues and organs, disseminate over the entire body by forming metastases, and finally lead to death.

Almost every second, people (in western countries) dealt with a cancer diagnosis during their lifetime [9]. On the one hand, this is a consequence of the increase of life expectancy during the last century - many types of cancer are "disease of age", since a longer life span increases the time over which random mutations in normal stem cells can accumulate and eventually lead to carcinogenesis [10]. On the other hand, the incidence of many cancer types is correlated with habits like smoking and alcohol abuse or exposition to certain environmental factors (e.g., ultraviolet radiation, some chemicals like asbestos...). Behind cardiovascular diseases, cancer ranks second in the causes of death.

The main cancer treatment techniques are here described.

1.1 Types of cancer treatment

There are many types of cancer treatment, that depend on the kind of tumour and how advanced it is.
Currently, more than 50% of cancer patients receive radiotherapy, making it one of the three cornerstones of cancer treatment along with surgery and chemotherapy.

- Surgery: Cancer surgery removes the tumor and nearby tissue during an operation. It is a localized treatment, it can thus lead to recovery when a solid tumor is confined to a single site and anatomical area. If the tumour can be completely removed, surgery is the unique needed treatment; otherwise, it may be combined with chemotherapy and/or radiation therapy to increase the possibility of a complete neoplastic cells removal.

- Chemotherapy: It is a type of cancer treatment that uses drugs to kill cancer cells, administered as primary treatment or together with other treatments. In case of non-localized tumours, chemotherapy becomes the main treatment because the drug can reach all parts of the body.

- Radiotherapy: The goal of radiotherapy treatment is to kill all tumour cells (curative treatment) or at least reduce symptoms such as pain (palliative treatment). This must go along with a tolerable level of damage to the surrounding normal tissue, which inevitably receives some dose.

The different radiation modalities and techniques used in radiotherapy are described in the next sections.

1.1.1 Radiation modalities

A first classification of the different techniques used in radiotherapy can be made according to the type of radiation (photons, charged particle, neutrons), as well as the nature of the radiation source and its location relative to the patient:

- **Teletherapy** (or external beam radiation therapy): The prefix *tele* means *far from*, that is the radiation source is well separated from the patient.
  The workhorse of contemporary radiation therapy is the linear accelerator (LINAC), in which electrons reach energies of several MeV before hit a target and generate bremsstrahlung, which shows a pronounced dose build-up[1] effect and it is only slightly attenuated by typical patient dimensions (Figure 1.1, blue and pink curves). The distance of the source (where electrons hit the target) and the center of rotation of the LINAC (where the patient is positioned) is usually 100 cm. By moving the target from the beam, electrons can be directly used for the treatment of superficial regions due to their different depth dose characteristics (Figure 1.1 red curve). With dimensions of few meters, medical LINACs can be installed in every hospital. They have largely superseded the ^{60}Co machines, which use large amounts of this radioisotope (Figure 1.1, green dashed curve).
  Protons can be advantageous in many cases due to the narrow maximum of their percentage depth dose (PDD) curve[2] (Figure 1.1, black curve), but require considerably higher technical effort [11], and they are currently only available at a few facilities worldwide. This applies even more to heavy ion therapy (e.g., with carbon ions), which has an even sharper Bragg peak.

- **Brachytherapy** (or internal beam radiation therapy): In contrast, the prefix *brachy* means *short* or *close*. Radioactive sources contained in a protective capsule are placed either very close to or even within the tumour. Radiation can escape from the capsule, but the radioisotope itself remains separated from the organism. The energy of the emitted radiation is usually considerably lower compared to teletherapy, which allows good sparing of healthy tissue. Due to the small distances between source and irradiated tissue, dose gradients are steeper and dose inhomogeneity is higher compared to teletherapy. Some isotopes commonly used in brachyterapy are given in Table 1.1.

[1] *Build-up*: The maximum point of the deposited energy as a function of distance in depth from the patient surface.

[2] *Percentage depth dose*: it relates the absorbed dose deposited by a radiation beam into a medium as it varies with depth along the beam axis. The dose values are divided by the maximum dose, referred to as d_{max}, yielding a plot in terms of percentage of the maximum dose.

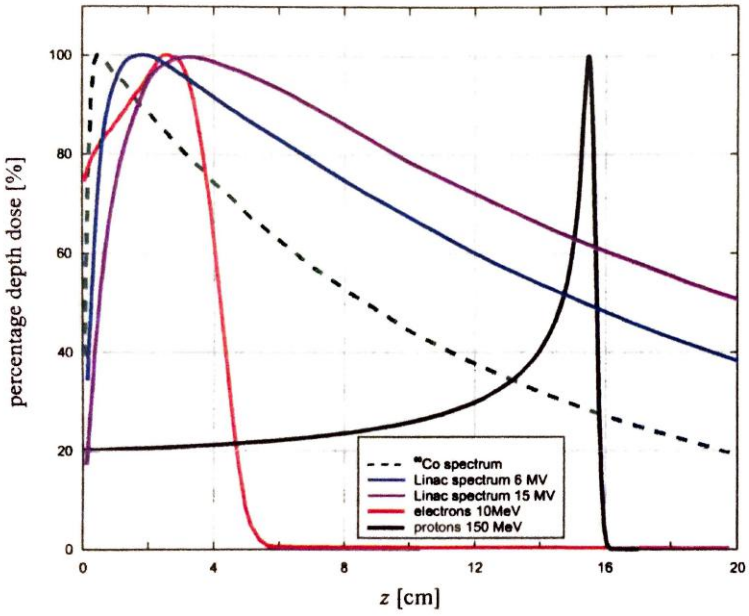

FIGURE 1.1: Characteristic percentage depth dose (PDD) curves of different types of radiation. Location and extent of the tumour determine which type of radiation at which energy is suited best. In addition, high LET radiation like protons, carbon ions or neutrons can be advantageous for radiobiological reasons. Electrons have got a short path in tissue, therefore they are used for skin tumours; X-rays penetrate deeper, but the dose absorbed by the tissue shows a typical exponential decay as the thickness increases. Instead, for protons and heavy ions the dose increases as the thickness increase up to the Bragg peak, that is at the path end of the particle where the treatment target is; after the Bragg peak the dose drops down to zero.

1.1.2 Treatment techniques

Radiotherapy

Teletherapy with photon radiation from a linear accelerator, which outnumbers all other form of radiotherapy, achieves high conformality (i.e., spatial agreement of the high dose region and the target volume to be irradiated) by superimposition of radiation beams from several directions.
It can be further subdivided into four different techniques:

- **Conventional radiotherapy**: each beam has a simple rectangular shape (Figure 1.2a). For a long time, further modulation could only be achieved by additional devices like blocks, wedges or compensators.

- **3D conformal radiotherapy** (3D-CRT): The shape of each beam is adapted to the contour of the tumor by a multileaf collimator (MLC) (Figure 1.2b). This yields better spatial agreement of the resulting dose distribution with the target volume, which is called *conformality*.

- **Intensity modulated radiotherapy** (IMRT): The intensity within each beam is modulated using MLC (figure 1.2c). This allows to achieve even better dose conformality, also for concave and very complex target volume shapes.

TABLE 1.1: Some radionuclides commonly used in brachyterapy. Only the emitted γ radiation can pass through the encapsulation and generate a dose distribution to treat the patient.

Isotope	**Half-life time** $T_{1/2}$	**Energy** E_γ [MeV]
Co-60	5.27 y	1.173 - 1.332
Ir-192	73.82 d	0.296 - 0.612
I-125	59.41 d	0.035

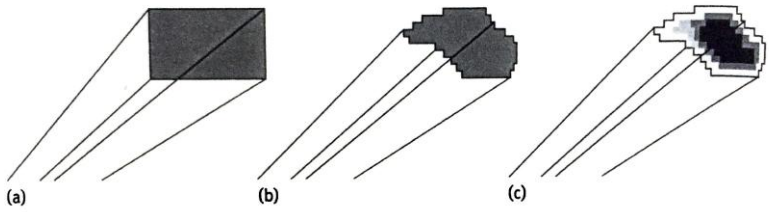

FIGURE 1.2: Illustration of the differences between different radiotherapy beams: (a) conventional radiotherapy beams (rectangular shape, constant photon fluence), (b) conformal radiotherapy beams (fields shaped by an MLC matching the target volume region, constant photon fluence) and (c) intensity modulated radiotherapy beams (IMRT, conformal fields with additional variation of photon fluence across the field).

Hadrontherapy

Hadrontherapy is a specific type of oncological teletherapy which makes use of fast hadrons to obtain better dose depositions when compared with the ones of X-rays used in conventional radiotherapy. It increases the local tumour control, safeguarding the surrounding healthy tissues and reducing the occurrence of late complications, thus enhancing the quality of life during and after cancer treatment.
Today only two types of hadrons are used to treat solid tumours - protons and fully stripped carbon ions - but other hadrons such as neutrons, charged pions, alpha particles and other light ions nuclei (like lithium, oxygen, up to silicon ions) have been either used or planned to be used for the treatment of cancer [12].
The strength of hadrontherapy lies in the unique physical and radiobiological properties of these particles, sometimes allowing to destroy radioresistant tumours.
Hadrons can penetrate the tissues with little diffusion and deposit the maximum energy just before stopping (as seen in Figure 1.1). This allows a precise definition of the specific region to be irradiated. The peaked shape of the hadron energy deposition is called Bragg peak and it has become the symbol of hadrontherapy.

Chapter 2

Elements of Radiobiology and Dosimetry

Ionizing radiation can cause considerable harm to living cells and tissues. The main target for radiation causing biological effects is the carrier of the genetic information, deoxyribonucleic acid (DNA), which in eukaryotic organisms it is located within the nucleus of cells. Radiation induced DNA damage can kill cells, induce mutations and cause carcinogenesis. Since the human body is constantly exposed to radiation of cosmic and terrestrial origin, a variety of DNA repair mechanisms to cope with radiation damage have evolved.
The medical use of X-rays has become the most important source of man made radiation exposure, therefore the risks of ionizing radiation must be carefully assessed and balanced against its possible benefits. This requires precise knowledge about the biological response of different tissues to ionizing radiation, as well as the ability to conform a dose distribution inside the patient body that closely matches the tumour, while healthy and normal tissue is spared.
This chapter addresses some fundamental physics principles required for a quantitative description of these processes.

2.1 Introductory remarks on the interactions of ionizing particles with matter

This section gives some introductory remarks on the photon interactions with matter.
Typical photon energies used in X-ray imaging are on the order of about 10 keV, in medical diagnostics of about 100 keV and in radiotherapy of few MeV. In contrast, only few eV are usually required for ionization of the low Z elements of biological tissues.
The energy transfer from high energy photons to matter (e.g., a patient's body) is a two step procedure:

1. The primary photon interactions with matter - photoelectric effect, Compton effect and pair production - trigger secondary charged particles.

2. These are much more likely to interact with matter (per unit path length) since they are subject to the Coulomb force and lose their kinetic energy in numerous collision events, foremost with atomic electrons of the absorber.

In addition, the emission of secondary charged particles can produce photons again in the form of bremsstrahlung, fluorescence and annihilation radiation.
At energies used in diagnostic radiology, the range of secondary electrons is below

1 mm, while it can reach several cm in the MeV range used in radiotherapy. Since the energy of high energy photons is transferred to an absorbing medium almost exclusively by secondary charged particles, photon radiation is classified as indirectly ionizing radiation. Charged particle radiation, in contrast, is called directly ionizing radiation.

It can be assumed that the effects of radiation to a certain volume element dV of an irradiated absorbing medium, for example, the fraction of cells killed if the medium is living tissue, are determined by the amount of energy $d\epsilon$ deposited per mass $dm = \rho \cdot dV$. This leads to the definition of the **absorbed dose**, which is the central quantity in radiobiology, as well as in radiotherapy:

$$D = \frac{d\bar{\epsilon}}{dm} = \frac{1}{\rho}\frac{d\bar{\epsilon}}{dV} \tag{2.1}$$

While the energy deposited per unit mass $d\epsilon/dm$ in a small volume is subject to statistical fluctuations due to the discrete character of photons and charged particles, the absorbed dose is a nonstochastic quantity and it is defined as the corresponding expectation value, as denoted by the bar. The unit of absorbed dose is 1 J/kg = 1 Gray [Gy], in honor of L.H. Gray, who estalbished the field of radiobiology. An older unit is the radiation absorbed dose [rad], where 1 rad = 0.01 Gy.

Only if the range of secondary electron is negligibly small, the distribution of absorbed dose can be assumed to be proportional to the primary photon fluence. In the MeV range used in radiotherapy, however, this is no longer possible, since secondary electrons travel macroscopic distances of several cm from the site of the primary interaction. Therefore, to calculate the dose distribution resulting from high energy X-rays must include not only the primary interactions, but also the subsequent interaction of secondary charged particles and matter, as well as photons resulting from the Compton effect, electron-positron annihilation, bremsstrahlung and fluorescence.

2.2 Radiobiology

In radiotherapy and radiation protection, it is important to know about the effects of ionizing radiation on living organisms. The main references for the following brief account of radiobiology are [13], [14], and [15].

2.2.1 The cell cycle

Most cells in our body do not exist over our entire lifetime, but are replaced with a characteristic period ranging from a few days to several years [16]. I Each tissue contains a small fraction of stem cells, which are able to undergo, under special conditions, an unlimited number of cell divisions and provide replacement for old, worn out cells as long as the organism is still alive.
Cell division proceeds by the so called *cell cycle*, a sequence of molecular processes (see Figure 2.1). Five phases are distinguished:

- G_1: After cell division, each daughter cell is concerned with protein synthesis and growth to perform its specific task and prepare for replication of the DNA, the carrier of all genetic information.

- S: DNA replication leads to chromosomes consisting of two sister chromatids with identical base sequence that are held together in a region called *centromere*.
- G_2: Proteins that are required to perform the subsequent cell division are synthesized. Complex mechanisms check if complete DNA replication has been achieved and repair possible errors.
- M: The cell division, i.e. the formation of two nuclei each one containing the full genetic information, is known as the *mitosis* phase. It can be further subdivided into *prophase*, *metaphase*, *anaphase* and *telophase*. Only in the metaphase, the chromosomes are fully condensed and show the typical X like shape. Mitosis is usually followed by cytokinesis, the division of the cell body, resulting in two separate and genetically identical daughter cells.
- G_0: Cells can leave the cell cycle and enter a quiescent phase, in which they continue their specific tasks with no proliferation.

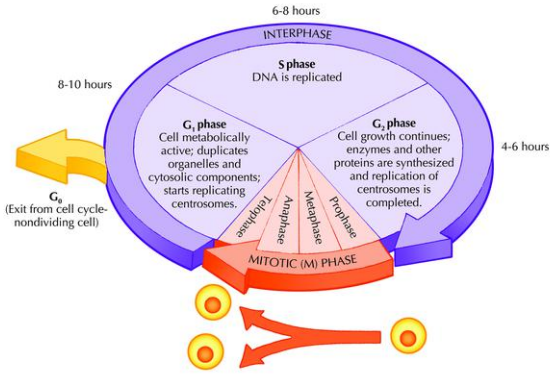

FIGURE 2.1: Schematic of the cell cycle. The interphase comprises G_1, S, and G_2 phases, in which the cell grows, replicates its DNA and prepares for division. Subsequently, in the M phase, the cell divides into two genetically identical daughter cells. For different mammalian cell types, the length of the phase G_1 can vary considerably, while the duration of the other phases show only little variation. Typical durations for human cells are indicated. Cells that do not show any proliferative activity are said to be in the G_0 phase. In cancerous cells, the molecular mechanisms controlling the cell cycle are insufficient, leading to an autonomous proliferation. Radiosensitivity is highest during M phase, followed by the G_2 phase: cells that proliferate quickly are thus typically more sensitive to radiation.

In normal and healthy tissue, the cell cycle is tightly controlled to maintain the cell number at a constant level adjusted to the requirements of the organism. the radiation sensitivity of cells shows some characteristic variations with the cell cycle phases, as will be discussed in chapter 6.

2.2.2 Ionizing radiation and biological organisms

The events in a biological organism that follow irradiation with high energy photons or charged particles can be divided into three stages:

1. The physical stage (time scale about 10^{-16} s to 10^{-13} s) comprises the excitation and ionization events in which energy is transferred from the incident radiation to the molecules of the biological organism. Note that the energy of a single photon with a energy range between 10 keV to 10 MeV, as used in radiological diagnostics or radiotherapy, is several orders of magnitude higher than the typical excitation and ionization energies of biomolecules.

2. In the chemical stage (time scale about 10^{-13} s to 10^{-2} s), the absorbed energy leads to changes in the structure of the four classes of biomolecules - nucleic acids (DNA and RNA), proteins, carbohydrates and lipids. The result can be ionization, formation of radicals, disruption of covalent or hydrogen bonds, etc. However, since approximately the 80% of a cell's content is water, the most frequent event is the radiolysis of water:

$$\begin{aligned} H_2O &\rightarrow H\cdot + OH\cdot \\ H_2O &\rightarrow H_2O^+ + e^- \end{aligned} \tag{2.2}$$

   This is immediately followed by further reactions, like:

$$\begin{aligned} H_2O^+ &\rightarrow H^+ + OH\cdot \\ OH\cdot + OH\cdot &\rightarrow H_2O_2 \\ O_2 + e^- &\rightarrow O_2^- \\ O_2^- + H_2O &\rightarrow H_2O_2 + 2OH^- + O_2 \end{aligned} \tag{2.3}$$

   which produce so called **reactive oxygen species** (ROS). The hydroxyl radical $OH\cdot$ with an unpaired electron, hydrogen peroxide H_2O_2 and the superoxide anion O_2^- are chemically highly reactive and can cause modifications of biomolecules, including several types of DNA damage.
   In irradiation with photons and electrons, the **indirect action of radiation** via radicals and ROS created from water and molecular oxygen accounts for about 70% of radiation induced cell death, whereas with **direct action of radiation**, the immediate damage of DNA by the primary radiation or secondary electrons dominates in the case of massive charged particles (protons, α-particle, heavy ions). The two different mechanisms are sketched in Figure 2.2.

3. In the biological stage (10^{-2} s to years), the chemical modifications of biomolecules result in a cellular response by stopping the cell cycle and the DNA repair processes, by changing the cellular metabolism or, if the damage is severe, by leading the cell to death. If a proliferating cell survives despite damage to its DNA, the DNA mutations are passed on to subsequent cell generations. When a certain number of mutations has accumulated, this can lead to the transformation into a cancer cell (carcinogenesis).

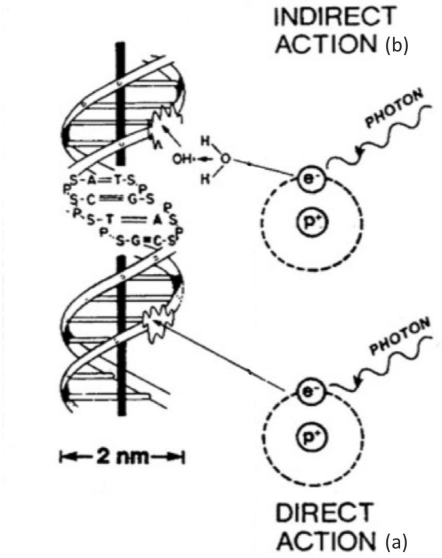

FIGURE 2.2: Direct and indirect action of radiation. A secondary electron released by an energy rich photon, for example, can (a) directly cause DNA damage or (b) create ROS, here a hydroxyl radical OH·, which subsequently reacts with DNA and thus indirectly leads to DNA damage.

2.2.3 Radiation damage to DNA

Different types of DNA damage can be caused by ionizing radiation (Figure 2.3):

- base or sugar (deoxyribose) damage
- covalent cross links between two DNA strands or DNA and proteins
- single strand breaks (SSBs)
- double strand breaks (DSBs)
- clustered lesions, i.e. combinations of the above types in close proximity

It has been estimated that an X-ray dose of 1Gy causes about 1000 base damages, 1000 SSBs and 20-40 DSBs in a typical, sufficiently oxygenated mammalian cell [17]. Several DNA repair mechanisms, each one specialized for a certain type of damage, have evolved to cope with the inevitable natural levels of ionizing radiation, warranting the genetic material integrity. In brief, base damage and SSBs can be repaired more reliably and with fewer error than DSBs, since the intact complementary DNA strand can be used as a template. Therefore, it is generally accepted that only DSBs are the principal lesions leading to the following radiation induced biological effects:

- **Genomic instability and carcinogenesis**: If repair mechanisms fail, but the cell survives, radiation damage can modify the DNA base sequence and cause thus genetic mutations. With regard to cancer, mutations in DNA regions that encode for proteins involved in cell cycle control or DNA repair are critical. If sufficiently many of these mutations (the exact number depends on the type of cancer) have accumulated in a single (stem) cell, the result can be unrestricted

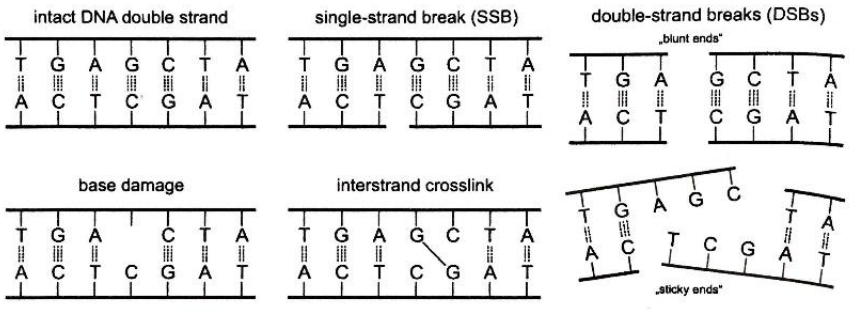

FIGURE 2.3: Schematic representation of several types of damage that can be inflicted on DNA by ionizing radiation, either by direct hit or indirectly by ROS. A number of highly efficient repair mechanisms exist. The biological effects of ionizing radiation are attributed to DSBs.

cell proliferation and invasive growth: the cell has transformed into a malignant cancer cell [18].

- **Cell death**: Ionizing radiation can kill cells. Different pathways are distinguished:

  1. *Mitotic or clonogenic* cell death: if DNA repair mechanisms fail, that can lead to errors in next of the subsequent cell divisions, triggering the cell death. This is considered the most important form of cell death from irradiation.
  2. *Apoptosis*: A "programmed cell death" triggered by a failure of DNA repair mechanism; a cell senses that something has seriously gone wrong with its DNA and, as a safeguard to protect the entire organism, it undergoes a defined sequence of morphological changes and finally dies. Note that one of the main characteristics of cancer cells is their increased resistance to pro-apoptotic signals, which promotes the tumour growth [18].
  3. *Necrosis*: High radiation doses can cause a massive loss of the function many proteins and damage membranes, leading to immediate cell death. In contrast to apoptosis, where the cell content remains separated from the extracellular space, here the cell leaks into the extracellular space causing an inflammatory reaction.

In summary, ionizing radiation is a sort of "double edged sword" [17] can both cause and cure cancer. On the one hand, it can induce genetic mutations leading to unrestricted cell division and tumor growth; on the other hand, large radiation doses targeted at tumour cells can kill these by inducing massive DNA damage, especially DSBs. The former effect is the reason for measures of radiation protection, while the latter is applied in radiotherapy.

2.2.4 Linear energy transfer and relative biological effectiveness

On the microscopic scale, the energy imparted to a biological system by ionizing radiation is not deposited uniformly. Energy transfer takes place in discrete ionization events, which are associated to the tracks of charged particles. For example: In two volume elements of equal size, the same absorbed dose D (total energy deposited in the volume divided by its mass) is deposited either by several ionizing particles tracks, or by a single track of a different particle that produces more ion pairs per unit path length[1], as shown in Figure 2.4.
Therefore, the absorbed dose D alone is not sufficient to characterize the effect of different types of ionizing radiation on living organisms. In fact, the probability of the generation of DNA DSBs also depends on the spatial distribution of ionization events, since one DSB requires two ionization events in close proximity and within a sufficiently short period of time. This is quantify by the **relative biological effectiveness** (RBE), defined as the radio between the dose of a reference spectrum (often 250 kV X-rays) and the dose of the test radiation that produces the same biological effect (e.g., the same survival probability of cells):

$$RBE = \frac{D(ref - radiation)}{D(test - radiation)} \tag{2.4}$$

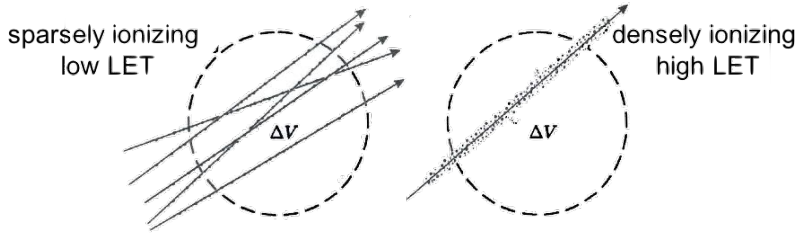

FIGURE 2.4: Microscopic energy deposition pattern of two different types of charged particles. Each black dot symbolizes an ionization event. In both volume elements ΔV, the same absorbed dose D is generated. On the *left*, D results from several incident charged particles with low ionization density along their track. On the *right*, an identical value D is created by a single charged particle that produces considerably more ionization event per unit path length (e.g., a proton or carbon ion).

The higher RBE, the more efficient the test radiation in production of DSBs compared to the reference radiation.

A frequently used quantity to characterize the microscopic pattern of dose deposition is the so called **linear energy transfer** (LET), which is usually given in units of [keV/μm]. It is defined as a fraction of the electronic stopping power[2] S_{el} due to

[1] The theoretical and experimental methods to quantify such dose inhomogeneities on the microscopic level is know as *microdosimetry*.

[2] When the term LET is used to characterize photon radiation, it actually refers to the secondary electrons released by the photons. The same applies to the case of neutrons, where LET refers to recoil protons released in collisions with atomic nuclei.

ionization events in which the kinetic energy transferred to an atomic electron of the medium is below a cutoff value Δ [19]:

$$LET_{\Delta} = S_{el,\Delta} = S_{el} - \frac{dE_{k.e.<\Delta}}{dl} \tag{2.5}$$

This way, energy rich knock on electrons that lead to energy dissipation away from the primary particle track are excluded. For given Δ, a *high LET* implies that ionization events resulting from a primary particle are "densely concentrated" along its track. Thus, LET_{Δ} can be interpreted as a measure of how "dense" the ionization track of a given type of radiation is.
In radiobiology, the LET concept is often used to distinguish between two categories of ionizing radiation:

- Densely ionizing radiation or **high-LET radiation**: Two subsequent events of a single incident particle are often close enough to induce DNA DBSs. Protons and heavy ions (i.e., α particles) usually are into this category, especially towards the end of their track in the region of Bragg peak. Also neutrons (which interact with atomic nuclei and produce recoil protons) belong to this class.

- Sparsely ionizing radiation or **low-LET radiation**: The typical distance between two interaction events is much larger than the diameter of the DNA molecule (2 nm). Creation of DSBs usually requires that two different particle tracks happen to cross the same DNA region. This category comprises photons and electrons.

The LET of a given type of radiation is fully characterized only if its spectral distribution is known [20]. However, values averaged over the track of known initial energy (or initial energy spectrum) are usually used as an approximation. The border line between the two categories is fixed around (30 - 50) keV/μm.
In general, for a given type of radiation, LET increases if the kinetic energy of charged particles decreases. In the case of photon radiation, LET refers to the released secondary electrons; while, for neutrons it refers to recoil protons.

Note that LET and RBE are related each other, as shown in Figure 2.5. It has been demonstrated that the maximum RBE for mammalian cells is reached around LET $\sim$ 100 keV/μm. This "optimal" LET corresponds to a mean distance between ionization events along a charged particle's track which is on the order of the diameter of a DNA molecule, i.e., the energy is spent most efficiently for DBS production. At still higher LET, energy is deposited inefficiently in ionization events that are too close together, and RBE decreases again.
In radiation protection (see Section 2.3), LET is used to determine quality factors for the risk assessment of different types of radiation.

2.2.5 Fractionation of radiation dose

In most cases, the total dose D that is considered sufficient to achieve tumour control (i.e., eradicate all tumour cells) at an accetable level of damage to normal tissue is not given in a single treatment, but in smaller portions called fractions. Standard radiation therapy thus delivers a dose of 2 Gy to the tumour at each fraction, 5 times a week during several weeks. This traditional fractionation regimen is aimed at maximizing the local control of the tumour while minimizing the toxicity to other healthy tissues based on radiobiology models. However, such fractionation regimen might

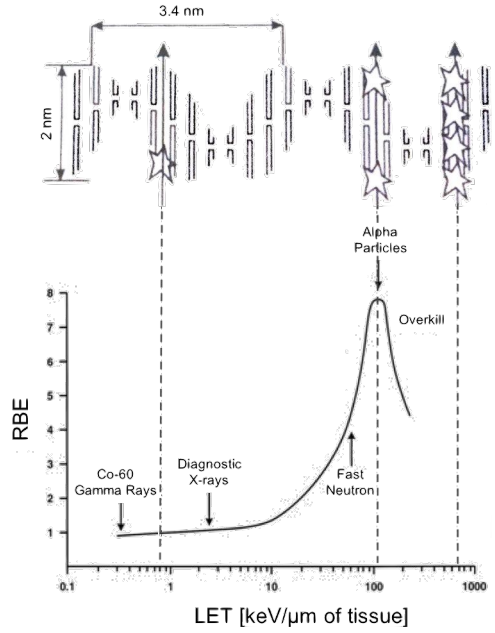

FIGURE 2.5: Plot of (average) LET vs RBE in cell killing. The curve reaches a peak at about 100 keV/μm, where the energy deposited in the medium is used most efficiently to induce DNA DSBs. Note that the absolute value of RBE is not unique, but it depends on the chosen biological effect [14].

not be beneficial for all tumours, in which case the dose per fraction can be increased without lowering the quality of the treatment [21]. Hypofractionated radiotherapy is increasingly being used to treat cancer. For this radiation treatment, the total dose of radiation is divided into large doses and treatments are given once a day or less often.
Research nowadays is ongoing to work out how low the fractions can go, but still be effective and safe, taking always into account the so called **4 R's of radiobiology** [14]

- *Repopulation*
- *Redistribution*
- *Repair of sublethal damage*
- *Reoxygenation*

both for tumoral and healthy cells, including also the new member of R's: the *Radiosensitivity*, which reminds that there is an intrinsic radiosensitivity or radioresistance in different cell types.

2.3 Radiation-induced effects

2.3.1 Deterministic and stochastic effects

Ionizing radiation has detrimental effects on living organisms, especially by damaging DNA, the carrier of the genetic information, as said in par. 2.2.2.
Based on the relation ship between dose and effect, the biological effects of radiation can be categorized as follows [22], [14], [23]:

- **Deterministic effects** (or tissue reactions) results from radiation induced cell killing. The loss of a small fraction of cells in an organ or tissue does not usually effect its function. However, if this fraction increases further, a clinically observable impairment of organ function will occur. The corresponding dose is called the threshold dose: above it, the probability of damage to an organ rapidly increases to 100%. In radiotherapy planning, dose limits to organs at risk are used to avoid these deterministic effects. The threshold doses are usually on the order of several tens of Gy for a fractionated treatment (as reporter in a recent summary [24]).

- **Stochastic effects**, in contrast, are not due to loss of cells, but result from radiation induced DNA mutations. It is custom that there is no threshold dose for stochastic effects, but different approaches are recently taken into account by the scientific community [25].

The differences between determinist and stochastic effects are summarized in Table 2.1. Their probability increases with the total dose an individual has received. However, in contrast to determinist effects, the severity for stochastic effects is dose independent: a malignant cancer resulting from mutations induced by a few high energy photons is as severe as if it was induced by a much higher radiation dose. It is thus very important to quantify the exact functional dependence of low doses of ionizing radiation and stochastic effects. Examples are the limits for occupational dose exposure, or screening tests like mammography, etc. Even if the risk may appear small, a large number of cases of, for example, carcinogenesis can result if large numbers of healthy individuals are deliberately exposed to ionizing radiation [26].

The so called **linear nonthreshold** (LNT) model assumes strict proportionality between dose and incidence of stochastic effects of radiation, without a threshold dose (Figure 2.6). Various other types of extrapolation from measured risks down to very small doses are represented also in Figure 2.6. Based on biophysical arguments, the LNT model is considered a conservative choice and it is, therefore, used as the basis of radiation protection.

TABLE 2.1: Comparison of deterministic and stochastic effects of ionizing radiation [14].

	Deterministic effects	**Stochastic effects**
Mechanism	cell killing	DNA mutation
Threshold dose	yes	no
Probability	increases with dose	increases with dose
Severity	increases with dose	independent of dose
Mathematical model	LQ model	LNT model

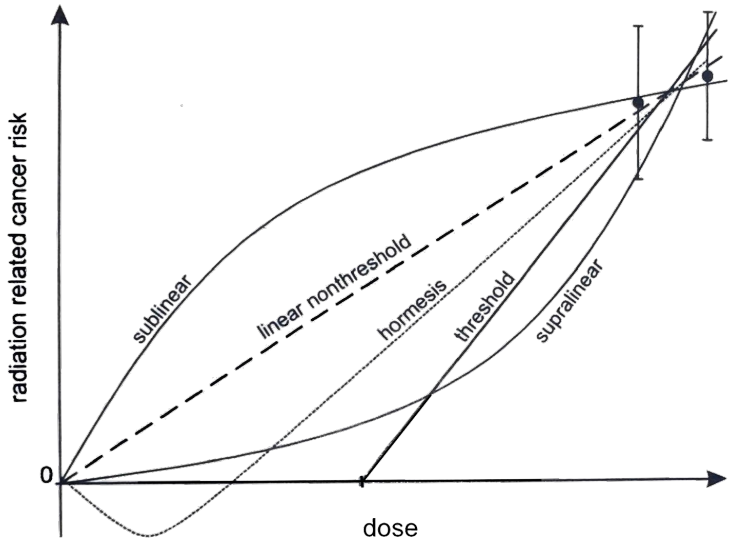

FIGURE 2.6: Schematic illustration of different possible extrapolations of the probability of stochastic radiation effects down to very low doses. The LNT model is considered as a plausible choice and used as the basis of radiation protection. However other models cannot be ruled out [26].

2.3.2 Equivalent and effective dose

The number of cells in an organ or tissue T that may be affected by radiation induced mutations is proportional to the absorbed dose $\bar{D}_T$ averaged over T. In addition, as discussed in par. 2.2.4, not only the absorbed dose alone, but also the RBE of the radiation determines the probability of radiation induced DNA mutations, depending on the type and energy spectrum of the chosen radiation.
For the purpose of radiation protection, approximative values, the **radiation weighting factors** w_R (Tab. 2.2) are used to determine the radiation weighted **equivalent dose**:

$$H_T = w_R \cdot \bar{D}_T \tag{2.6}$$

generated by radiation of type R in an organ or tissue T. The unit of the equivalent dose is 1 J $\cdot$ kg^{-1}, which is called 1 Sievert [Sv] in demarcation to the absorbed dose $D = d\bar{\epsilon}/m$ measured in Gray [Gy].

If an individual is exposed to different types of radiation, the equivalent dose for organ or tissue T is given by the sum:

$$H_T = \sum_R w_R \cdot \bar{D}_{T,R}. \tag{2.7}$$

The central quantity in radiation protection is the **effective dose**, which is given by the weighted sum of the equivalent doses of all organs and tissues in the human body:

$$E = \sum_T w_T \cdot H_T = \sum_T w_T [\sum_R w_R \cdot \bar{D}_{T,R}]. \tag{2.8}$$

Like the equivalent dose, also the effective dose is given in units of Sv. The weights w_T are called the **tissue weighting factors**[3] (Tab. 2.3).

TABLE 2.2: Radiation weighting factors w_R according to current recommendations of the ICRP 103 [22]. The values are based on the RBE (par. 2.2.4). Except for the case of neutrons, energy independent values are used as an approximation.

Radiation	w_R
Photons	1
Electrons and Muons	1
Protons and charged pions	2
Neutrons	continuous function of kinetic energy *
α particles, heavy ions, fission fragment	20

* The radiation weighting factor for neutrons with kinetic energy E is given by the continuous function:

$$w_R(E) = \begin{cases} 2.5 + 18.2exp[-\frac{1}{6}ln^2(E)], & E < 1 \text{ MeV} \\ 5.0 + 17.0exp[-\frac{1}{6}ln^2(2E)], & 1 \text{ MeV} < E < 50 \text{ MeV} \\ 2.5 + 3.25exp[-\frac{1}{6}ln^2(0.04E)], & E > 50 \text{ MeV} \end{cases} \tag{2.9}$$

Finally, the different dose concepts used in dosimetry and in radiation protection are summarized in Tab. 2.4.

Equivalent dose and dose equivalent

"Equivalent dose" and "Dose equivalent" are not the same quantities. Equivalent dose was introduced the first time in ICRP 60 [27] (1990), replacing the Dose Equivalent of ICRU concept as the quantity to be adopted in radiation protection activities. But there is still confusions and misuses in applying them.

The dose equivalent is evaluated at a specific point in the tissue-equivalent phantom; the equivalent dose is determined by averaging dose over the mass of a receptor tissue of interest in the medium of interest [28].

[3] Each w_T factor used in the calculation of the effective dose is based on the nominal risk coefficients R_T (cases per 10000 persons per Sv), which are weighted by the lethality fraction k_T, the relative life lost l_T and the reduction in file quality, as deeper described in [22]

TABLE 2.3: Tissue weighting factors w_T according to current recommendations of the ICRP 103 [22].

Organ / Tissue T	w_T
Gonads	0.08
Bone marrow	0.12
Colon	0.12
Lung	0.12
Stomach	0.12
Breast	0.12
Other solid	0.12
Bladder	0.04
Liver	0.04
Oesophagus	0.04
Thyroid	0.04
Skin	0.01
Bone	0.01
Brain	0.01
Salivary glands	0.01
Σ	1.00

However, the current ICRP recommends evaluating only equivalent doses in a tissue H_T from the absorbed dose in this tissue D_T and the radiation weighting factors w_R. Unfortunately, experimentally, the absorbed dose is extremely difficult in practice to measure in some cases, like when dealing with neutron irradiation, because of the complexity of neutrons interaction mechanisms with matter: all secondary charged particles originating around the volume of interest would have to be considered and their energy deposition inside the region of interest would have to be evaluated. A paper by Sanchez-Doblado et al. [29] tried to establish a methodology to correlate the readings of the detectors to the neutron equivalent doses in specific organs of patients undergoing external photon beam radiotherapy. From the work it emerges that, for experimental measurements, equivalent dose is a good estimator of the dose equivalent, with an overall uncertainty of the order of 30%.

TABLE 2.4: Summary of different dosimetric quantities.
The absorbed dose is the fundamental physical quantity in dosimetry and in radiotherapy; equivalent and effective dose are mainly used in the context of radiation protection.

Quantity	Definition	Used in
absorbed dose	energy deposited per mass element of a medium (usually water) $D = \frac{d\bar{\epsilon}}{dm} = \frac{1}{\rho}\frac{d\bar{\epsilon}}{dV}$ $[D] = 1\frac{J}{kg}$ = [1 Gy] (Gray)	dosimetry, radiotherapy
equivalent dose	mean absorbed dose in a certain organ/tissue T multiplied by radiation weighting factor (Tab. 2.2) $H_T = w_R \cdot \bar{D}_T = \sum_R w_R \bar{D}_{T,R}$ $[H_T] = 1\frac{J}{kg}$ = [1 Sv] (Sievert)	radiation protection
effective dose	sum of equivalent doses weighted according to risk of stochastic effects (Tab. 2.3) $E = \sum_T w_T \cdot H_T = \sum_T w_T [\sum_R w_R \bar{D}_{T,R}]$ $[E] = 1\frac{J}{kg}$ = [1 Sv] (Sievert)	radiation protection

Chapter 3

Electron linear accelerators for radiotherapy

Medical electron linear accelerators (LINAC) have been started to be employed in clinical applications since the fifties. In contrast to LINACs used for high-energy physics research, medical LINACs are compact machines mounted isocentrically so to allow practical radiation treatment aiming the beam toward the patient from various directions to concentrate the dose in the tumor and spare healthy tissues as much as possible. In fact, the main goal of modern oncological radiotherapy is to increase the treatment therapeutic index, intended as a progressive increase in the total radiation dose to the target volume safeguarding healthy surrounding tissues, by intensifying the beam energy and by diversifying its section.

Medical LINACs accelerate electrons to kinetic energies from 4 MeV to 22 MeV. Then, the electron beam can be converted to X-rays or can alternatively be directly used for the treatment.
Various types of LINACs are available for clinical use: a typical modern high-energy LINAC provide photon with accelerating potentials of 6 MV, 10 MV, 15 MV and/or 18 MV, and several electron energies in the range from 4 MeV to 22 MeV.

This chapter describes the structure of a typical medical linear accelerator and the different types of collimation and beam shaping systems for the control of the tumour. Moreover, the last section gives a brief overview of the radiation treatment parameters.

3.1 Principles of linear accelerators

In a linear accelerator (LINAC) designed for radiotherapy, electrons are generated by thermionic effect in the *gun*. Bunches of these electrons are injected into an accelerating structure, in synchronism with the pulsed microwave radiation inside it, gaining thus energy by interacting with the synchronised radio-frequency electromagnetic field (typical value 3 GHz). The accelerating *waveguide* (the accelerator structure) consists of a long cylindrical tube, containing a series of circular baffles. These are designed so that speed of propagation of the microwaves increases in the first part of the accelerating tube until it eventually reaches velocities close to the light speed.
The microwaves are generated by a *magnetron* or *klystron*, by applying high voltage pulses (about 50 kV), lasting only a few microseconds, coming from a *modulator*. The electron gun and the accelerating waveguide are kept at low pressure, so that the mean free path of electrons for atomic collisions is long.

The energy an electron can acquire from the radio-frequency field in the waveguide depends on the electric field amplitude, which in turn depends on the instantaneous power of the microwave generator. The required power is a few megawatts. The microwave generators, for thermal reasons, cannot work continuously at these power levels: that's why the electrons are produced in bunches.

The accelerated electrons tend to diverge, both by the mutual repulsion due to the Coulomb's force and because the electric field in the waveguide has also a radial component. For this reason, a coaxial magnetic field in the waveguide is used to focus the beam. Moreover, at the exit of the accelerating area, other coils (the *steering coils*) are present to direct the beam, so that it has the desired position and direction.

The LINACs can work in two different modalities:

1. *Electron mode*: the high energy electron beams, typically from 6 MeV to 22 MeV, can be directly used for therapy. Their depth dose curves are characterized by initial skin sparing followed by several centimeters of uniform dose (depending on energy) and then a rapid fall-off in dose as shown in Figure 3.1. Electron beams from linear accelerators are useful for the treatment of tumours up to about 7 cm deep, due to their low penetrating power being low-LET particles (par. 2.2.4); thus, for more deep-seated tumours, it is better to use photon beams.

2. *Photon mode*: the electrons are focused onto a high-atomic-number thick target, and their energy loss is converted into bremsstrahlung radiation in order to have a more penetrating beam in tissue, reaching deeper-seated tumours (see depth dose curves, Fig. 3.8). At megavoltage energies, like the ones used in radiotherapy, the principal direction of bremsstrahlung emission is in the forward direction. In the simplest accelerators, the target is fixed and the accelerating structure is coaxial with the emerging X-ray beam (i.e. it is parallel to the direction of travel of the electrons so that no bending of the electrons takes place) and it is perpendicular to the cranio-caudal[1] axis of the patient. However, for energies above 6 MeV, the length of the accelerator tube is such that it makes this impracticable. In order for the radiation beam to be brought in to irradiate the patient from any angle, it becomes necessary to bend the beam: electrons are easily deflected through a magnetic field, bending them of 270°. A schematic representation of a LINAC working in photon mode is shown in Figure 3.2.

The challenge for accelerator design is to produce a stable monoenergetic high current electron beam concentrated onto a small focal spot that will ensure that a sharply focussed X-ray beam can be produced. The X-ray beam must be modified to allow uniform irradiation of the intended treatment area of the patient, which can vary from a very small area up to a maximum of about (40×40) cm^2. Moreover, it's possible to choose the beam energy to suit the tumour being treated.

3.1.1 Components of modern LINACs

A schematic diagram of a typical modern medical LINAC is shown in Figure 3.3. Also shown are the connections and relationships among the various LINAC components; however, there are significant variations from one commercial machine to

[1] *Cranio-caudal*: direction from head to foot. The X-ray beam enters at the cranial end of the part being examined and exits at the caudal end.

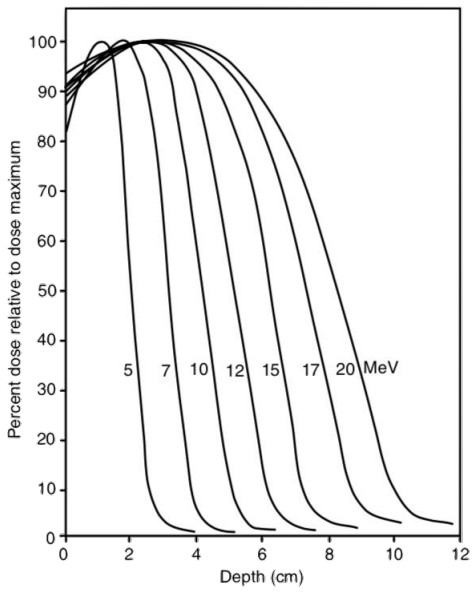

FIGURE 3.1: Electron-beam depth-dose curves. Representative central axis percentage depth-dose curves for electron beam energies from 5 MeV to 20 MeV. (Picture from [30]).

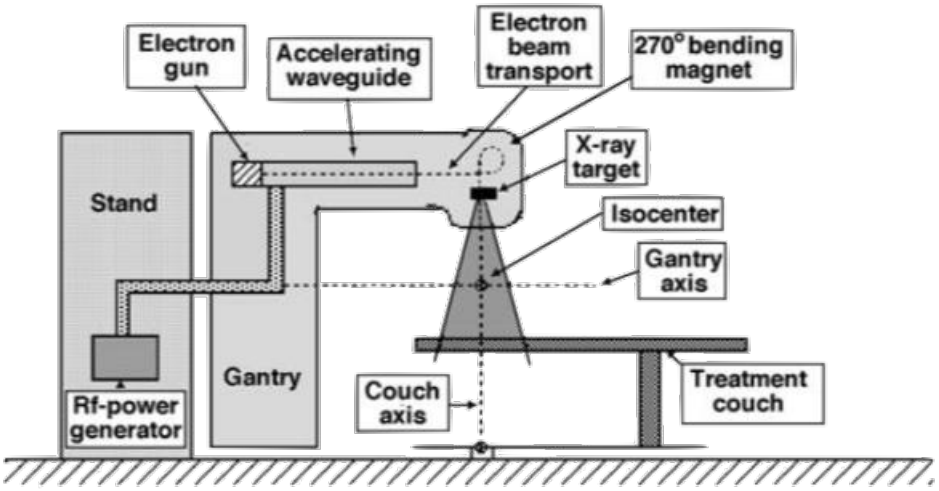

FIGURE 3.2: Design configurations for isocentric medical LINACs working in photon mode. The accelerating waveguide is in the gantry parallel to the isocenter axis; electrons are brought to the movable target through a beam transport system; the RF-power generator is located in the gantry stand; the machine produce megavoltage X-rays.

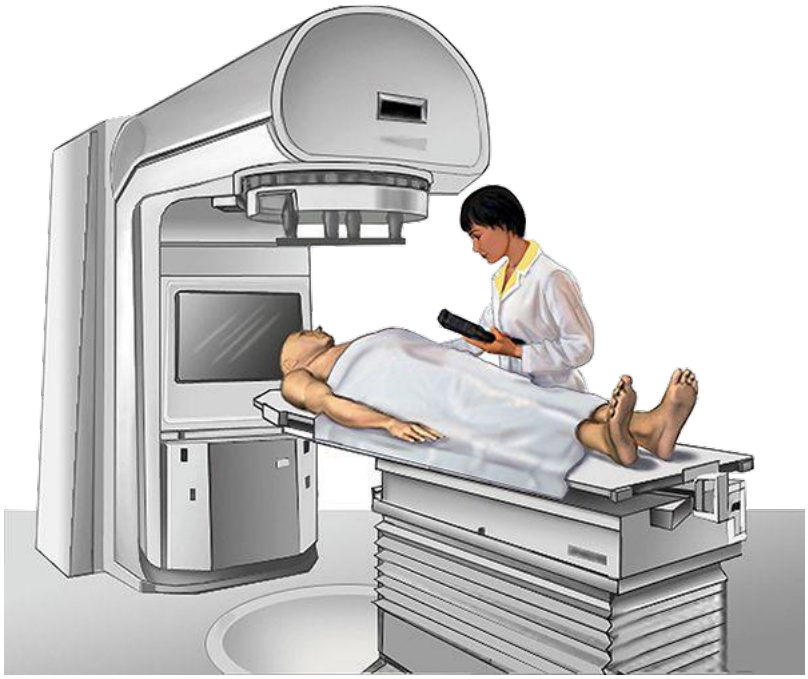

(A) Outer view.

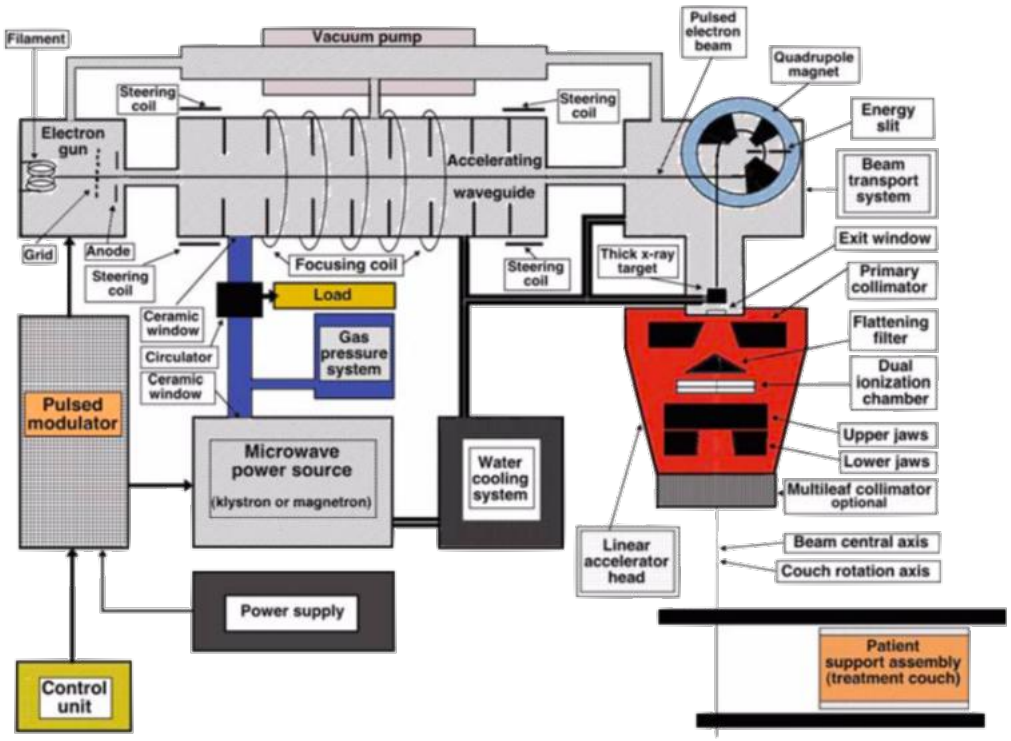

(B) Inner view. (Reproduced from [31])

FIGURE 3.3: Schematic representation of a typical medical linear accelerator: inner and outer view.

another, depending on the final electron beam kinetic energy as well as on the particular design used by the manufacturer: for example, the length of the accelerating waveguide depends on the final electron kinetic energy, and ranges from ∼30 cm at 4 MeV to ∼150 cm at 22 MeV.

The beam-forming components of medical LINACs are usually grouped into six classes:

1. *Injection system*
2. *RF power generation system*
3. *Accelerating waveguide*
4. *Auxiliary system*
5. *Beam transport system*
6. *Beam collimation and beam monitoring system*.

1. The *injection system* is the source of electrons, essentially a simple electrostatic accelerator called "electron gun". Electrons are thermionically emitted from the heated cathode, focused into a pencil beam and accelerated toward the perforated anode through which they drift into the accelerating waveguide.

2. The *radiofrequency (RF) power generating system* produces the high power microwave radiation used for electron acceleration in the accelerating waveguide and consists of two components: the RF power source and the pulsed modulator. The RF power source is either a magnetron or a klystron in conjunction with a low power RF oscillator. Both devices use electron acceleration and deceleration in vacuum for production of the high power RF fields. The pulsed modulator produces the high voltage, high current, short duration pulses required by the RF power source and the electron injection system.

3. Electrons are accelerated in the *accelerating waveguide* by means of an energy transfer from the high power RF field which is set up in the accelerating waveguide and produced by the RF power generator. The accelerating waveguide is in principle obtained from a cylindrical uniform waveguide by adding a series of disks with circular holes at the center, positioned at equal distances along the tube.

4. The *auxiliary system* consists of several basic systems that are not directly involved with electron acceleration, yet they make the acceleration possible and the LINAC viable for clinical operation. These systems are: the vacuum-pumping system, the water-cooling system, the air-pressure system, and the shielding against leakage radiation.

5. The *electron beam transport system* brings the pulsed high-energy electron beam from the accelerating waveguide onto the target in the X-ray therapy mode and onto the scattering foil in the electron therapy mode.

6. The *beam monitoring system* and the *beam collimation system* ensure that the radiation dose is delivered to the patient as prescribed, with a high numerical and spatial accuracy.

3.1.2 The LINAC treatment head

The LINAC head contains several components, which influence the production, shaping, localizing, and monitoring of the clinical photon and electron beams. Electrons, originating in the electron gun, are accelerated in the accelerating waveguide to the desired kinetic energy and then brought, in the form of a pencil beam, through the beam transport system into the LINAC treatment head, where the clinical photon and electron beams are produced.

The important components found in a typical head of a modern LINAC (see Fig. 3.4) operating in photon mode include:

1. X-ray targets
2. Flattening filters and electron scattering foils
3. Primary and secondary collimators
4. Dual transmission ionization chambers
5. Field defining light and range finder
6. Optional retractable wedges or full dynamic wedges
7. Optional multileaf collimator (MLC).

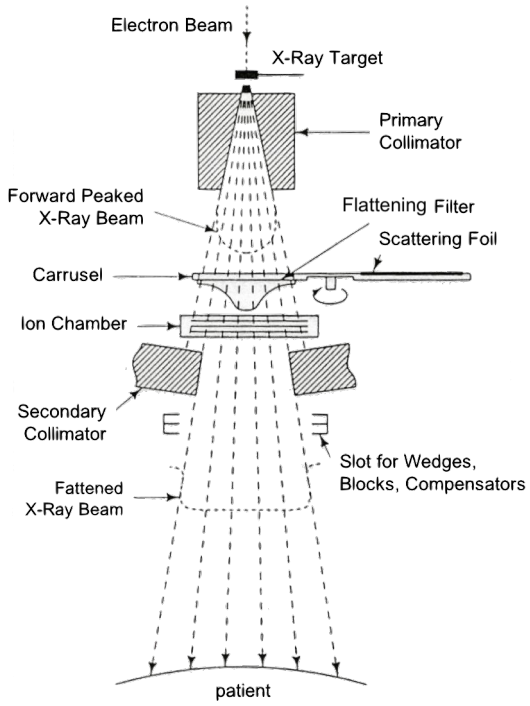

FIGURE 3.4: Schematic representation of a typical LINAC head operating in photon mode. The z-axis is directed downward.

1 + 2. Clinical photon beams are produced in an X-ray *target* and flattened with a *flattening filter*. Each clinical photon beam has its own target-flattening filter combination. Optimal targets have a high atomic number Z and the flattening filters are mounted on a rotating carousel for ease of mechanical positioning into the beam. The photon maximum energy is equal to the energy of the electrons striking on the target, and its mean energy is equal to 1/3 of the maximum one. Since the clinical photon beam is not a monoenergetic beam, it's usual to refer to it giving the electron accelerating potential rather than an energy value.

3. The *primary collimator* defines the largest available circular field size and is a conical opening machined into a tungsten shielding block, with the sides of the conical opening projecting on to edges of the target on one end of the block and on to the flattening filter on the other end.
The *secondary beam defining collimators* consist of four blocks, two forming the upper and two forming the lower jaws of the collimator. They can provide rectangular or square fields with a maximum dimension of (40 $\times$ 40) cm^2 at the LINAC isocentre.

4. *Dual transmission ionization chambers* are used for monitoring the photon radiation beam output as well as the radial and transverse beam flatness. The customary position of the dose monitor chambers is between the flattening filter or scattering foil and the photon beam secondary collimator. For patient safety, the linac dosimetry system usually consists of two separately sealed ionization chambers with completely independent biasing power supplies: if the primary chamber fails during patient treatment, the secondary chamber will terminate the irradiation.
The primary ionization chamber measures the Monitor Units (MUs). Typically, the sensitivity of the chamber is adjusted in such a way that 1 MU corresponds to a dose of 1 cGy delivered in a water phantom at the depth of dose maximum (buid-up) on the central beam axis when irradiated in standard conditions[2].

5. *The field defining light* and *the range finder* provide convenient visual methods for correctly positioning the patient for treatment using reference marks. The field light illuminates an area that coincides with the radiation treatment field on the patient's skin, while the range finder is used to place the patient at the correct treatment distance by projecting a centimeter scale whose image on the patient's skin indicates the vertical distance from the LINAC isocentre.

6. *Wedges* are accessories placed on the proper support below the secondary collimators. The wedge are used to make the dose distribution at the target volume more homogeneous. They induce a beam attenuation and a hardening of the spectrum, cutting the low energy component and thus increasing the main photon energy.

7. *Multileaf collimators* (MLCs), represented in Figure 3.5, are a relatively recent addition to LINAC dose delivery technology. The number of leaves in commercial MLCs is steadily increasing, and models with 120 leaves (60 pairs) are currently available. This system allows to contour the photon field, personalizing its shape according to the target volume shape. The customary position of MLC is below the secondary collimators.

[2] *Irradiation in standard conditions*: irradiation set-up with a field size of (10 $\times$ 10) cm^2 at isocentre and a source to surface distance SSD of 100 cm

Notice that:

- the LINAC head can rotate in the orizzontal plane of 360° in order to irradiate the patient in all the directions;
- the **isocentre** is the intersection point between the couch and gantry axes;
- the distance from the beam source to isocentre is called **SAD (Source to Axis Distance)**;
- the distance from the beam source to the patient surface is called **SSD (Source to Surface Distance)**.

These reference radiation treatment parameters are shown in Figure 3.6.

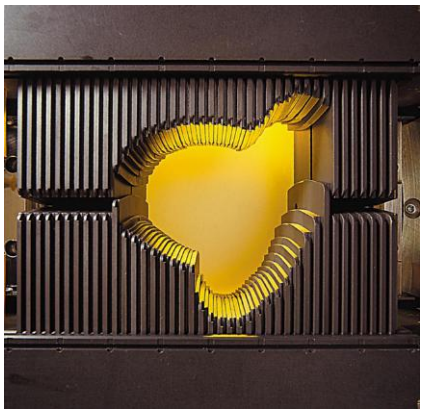

FIGURE 3.5: Detail of the multileaf collimator.

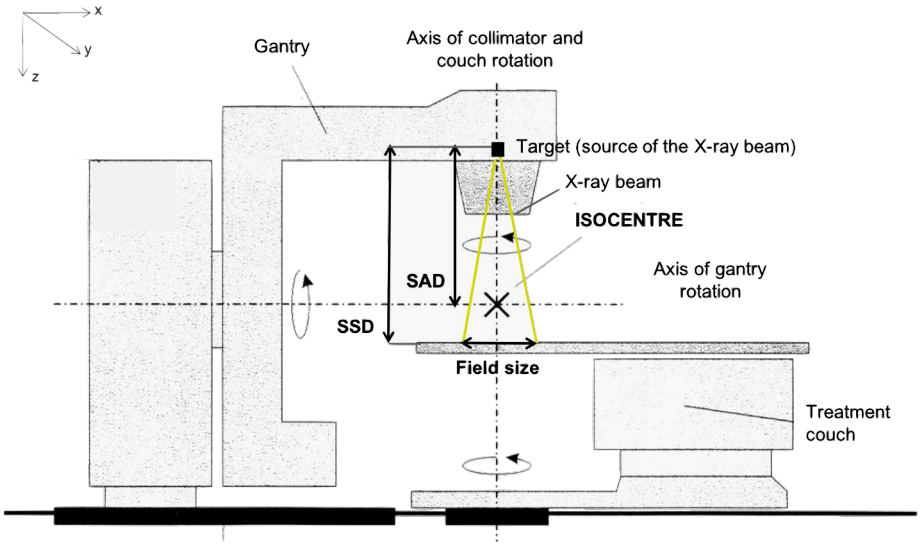

FIGURE 3.6: Reference parameters used in radiotherapy. The isocentre, the field size, the source to axis (SAD) and source to surface (SSD) distances are shown.

3.2 Radiation treatment parameters

The main parameters in external beam dose delivery with photon beams are:

- the depth of treatment;
- the field size:
- the SSD in SSD set- ups (or SAD in SAD isocentric set-ups);
- the photon beam energy.

All these parameters are given before starting a treatment.
In this work all measurements and simulations were carried out in SSD set-ups, and the radiation treatment parameters are always reported.

3.2.1 Central axis depth doses: source to surface distance set-up

Percentage depth dose

Central axis dose distributions inside the patient or phantom are usually normalized to D_{max} = 100% at the depth of dose maximum z_{max} and then referred to as the PDD distributions (Percentage Depth Dose).
The PDD is thus defined as follows:

$$PDD(z, A, f, h\nu) = 100\frac{D_Q}{D_P} \tag{3.1}$$

where D_Q is the dose at point Q at depth z on the central axis of the phantom and D_P is the dose at point P at z_{max} on the central axis of the phantom.

The geometry for PDD definition is shown in Figure 3.7. Point Q is an arbitrary point at depth z on the beam central axis; point P represents the specific dose reference point at z = z_{max} on the beam central axis.
The PDD depends on four parameters: depth in a phantom z, field size A, SSD (often designated with f) and photon beam energy $h\nu$. The PDD ranges in value from 0 at $z \to \infty$ to 100 at z = z_{max}.
An example of PDD distributions for (10 $\times$ 10) cm^2 fields and various megavoltage photon beams is given in Figure 3.8. The size of the build-up region increases with beam energy and the surface dose decreases with beam energy.

Tissue-phantom ratio or tissue-maximum ratio

Tissue-phantom ratio (TPR) is defined as follows:

$$TPR(z, A_Q, h\nu) = \frac{D_Q}{D_{Qref}} \tag{3.2}$$

where D_Q is the dose in a phantom at arbitrary point Q on the beam central axis, and D_{Qref} is the dose in a phantom at a reference depth z_{ref} (typically 10 cm) on the beam central axis.

The geometry for the measurement of doses D_Q and D_{Qref} is shown in Figure 3.9.

A special TPR is defined for the reference depth z_{ref} equal to the depth of dose

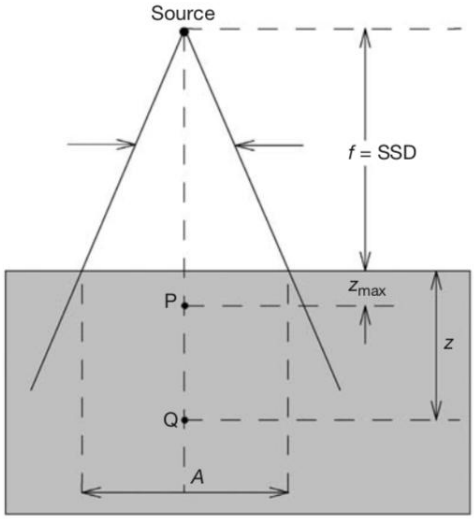

FIGURE 3.7: Geometry for PDD measurement and definition . Point Q is an arbitrary point on the beam central axis at depth z, point P is the point at z_{max} on the beam central axis. The field size A is defined on the surface of the phantom.

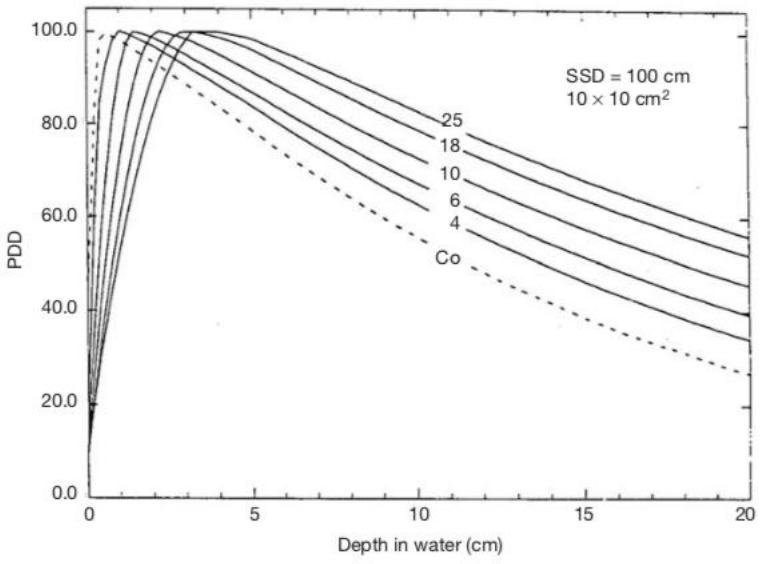

FIGURE 3.8: PDD curves in water for a (10 $\times$ 10) cm^2 field at an SSD of 100 cm for various megavoltage photon beams ranging from 60Co γ-rays to 25 MV X-rays (Picture from [30]).

maximum z_{max}, which is referred to as the tissue-maximum ratio (TMR), defined as follows:

$$TMR(z, A_Q, h\nu) = \frac{D_Q}{D_{Qmax}} \tag{3.3}$$

where D_Q is the dose in a phantom at point Q at a depth z in a phantom D_{Qmax} is the dose at point Q at z_{max}.
The geometry for the definition of TMR is the same as in Figure 3.9, except that z_{ref} is now z_{max}.

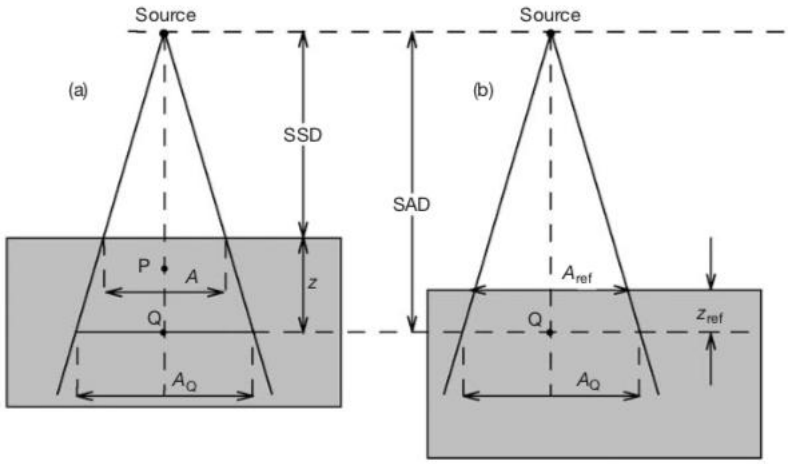

FIGURE 3.9: Geometry for the measurement of TPR. (a) Geometry for the measurement of D_Q at depth z in a phantom; (b) the geometry for the measurement of D_{Qref} at depth z_{ref} in a phantom. The distance between the source and the point of measurement, as well as the field size at the point of measurement, is the same for (a) and (b).

Relationship between TPR and PDD

As shown in Figure 3.10 a relationship may be derived between TPR and the corresponding PDD from the definitions governing the two functions.
In the first approximation:

$$TPR(z, A_Q, h\nu) \approx \frac{PDD(z, A, f, h\nu)}{100} \left(\frac{f+z}{f+z_{max}}\right)^2 \tag{3.4}$$

where, remembering, z is the depth in a phantom, A the field size, f the SSD and $h\nu$ the photon beam energy.

However, an analytical expression is more often used in clinical application for speed up the calculations. Knowing the value of the PDD at 20 cm and 10 cm, it's possible to found the corresponding TPR as:

$$TPR_{20,10} = 1,2661 \times \left(\frac{D_{20}}{D_{10}}\right) - 0,0595 \tag{3.5}$$

All the relationships between depth-doses at different megavoltage photon beam are reported inTable 3.1.

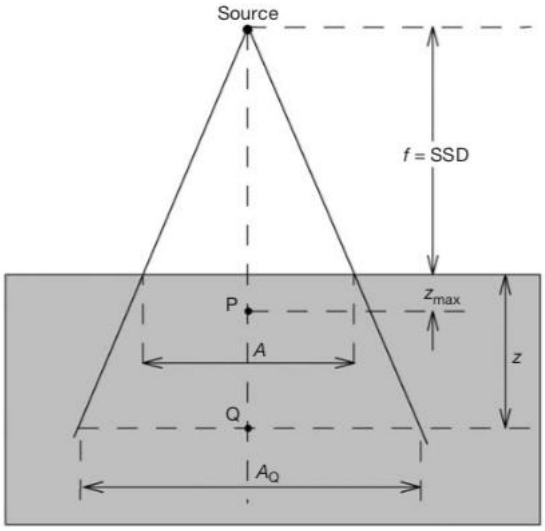

FIGURE 3.10: Geometry for derivation of the relationship between PDD and TPR.

TABLE 3.1: Photon beam quality: relationship between depth-doses at different megavoltage photon beam [32].

Beam	**z-max** [cm]	$\mathbf{PDD}_{(10cm)}$	$\mathbf{TPR}_{20/10}$
6 MV	1.7	67.8	0.679
10 MV	2.5	73.2	0.713
18 MV	3.5	78.8	0.774
25 MV	4.0	81.9	0.801

Chapter 4

Neutron contamination from medical accelerators

Medical LINACs for radiotherapy produce fast secondary neutrons due to photonuclear (γ, n) reactions. Neutron production can result in doses to patients and to operating personnel from direct exposure both to neutrons and to the resulting residual radioactivity.
The minimum energy required to remove one neutron from a nucleus lies between 6 and 20 MeV for most stable nuclei heavier than carbon. A nucleus can absorb energy from high-energy photon and it can emit a neutron if the photon energy exceed the minimum energy.
Above the neutron separation energy, the cross section for neutron production increases with the photon energy E_γ, reaches a maximum value, and then decreases with further increases of E_γ. The shape of this peak is characteristic of resonance reactions and it is called *giant dipole resonance* (GDR).
In summary, the potential sources of neutron contamination are any materials on which the X-ray beam is incident, such as target, scattering foils, collimators, jaws, etc., in addition to being produced in the bunker walls, floor and ceiling or directly inside the human body; while, the potential sources of residual radioactivity are any places where neutrons are produced or absorbed.
Before starting to discuss the physics of photoneutrons and their consequences in radiotherapy, it's important to give a general description of the photon interactions with matter.

4.1 General aspects of photon interactions with matter

Photons are indirectly ionizing radiation and they deposit energy in the matter through a two-step process:

1. in the first step energy is transferred to an energetic light charged particle;
2. in the second step energy is deposited in the absorbing medium by the charged particle.

The energy transferred to charged particles from the interacting photon generally exceeds the energy subsequently deposited in the absorbing medium by the charged particles, because some of the transferred energy may be radiated from the charged particles in the form of photons.
Depending on their energy and the atomic number of the absorber, photons may interact with an absorber atom as a whole, with the nucleus of an absorber atom, or with an orbital electron of the absorber atom.

As far as the photon fate after the interaction with an atom is concerned there are two possible outcomes:

1. Photon disappears (i.e., is absorbed completely) and a portion of its energy is transferred to light charged particles (electrons and positrons).
2. Photon is scattered and two outcomes are possible:
   a The resulting photon has the same energy as the incident photon and no light charged particles are released in the interaction.
   b The resulting scattered photon has a lower energy than the incident photon and the energy excess is transferred to a light charged particle (electron).

The light charged particles (electrons and positrons) released or produced in the absorbing medium through photon interactions will:

1. Either deposit their energy to the medium through Coulomb interactions with orbital electrons of the absorbing medium (collision loss also referred to as ionization loss)
2. Or radiate their kinetic energy away in the form of photons through Coulomb interactions with the nuclei of the absorbing medium (radiation loss)

The probability of a particular interaction to occur depends on the photon energy, as well as on the density and atomic number of the absorber, and it is generally expressed in the form of a cross section.

In penetrating an absorbing medium, photons may experience various interactions with the atoms of the medium. These interactions involve either the nuclei of the absorbing medium or the orbital electrons of the absorbing medium:

- The interactions with nuclei may be direct photon-nucleus interactions (*photodisintegration*) or interactions between the photon and the electrostatic field of the nucleus (*pair production*).
- The photon - orbital electron interactions are characterized as interactions between the photon and either (1) a loosely bound electron[1] (*Thomson scattering, Compton effect, triplet production*) or (2) a tightly bound electron[2] (*photoelectric effect, Rayleigh scattering*).

4.1.1 Classification of photon interactions with absorber atoms

As seen in the above section, photons with energy in the ionizing radiation category have several options for interacting with matter. The seven interactions of importance in medical physics and radiation dosimetry are summarized in Table 4.1, and they can be classified according to:

- Type of target (orbital electron or nucleus), as shown in Table 4.2.

[1] *Loosely bound electron*: It is an electron whose binding energy E_B is small in comparison with photon energy $h\nu$, i.e., $E_B << h\nu$. An interaction between a photon and a loosely bound electron is considered as an interaction between a photon and a "free" (i.e., unbound) electron.

[2] *Tightly bound electron* is an electron whose binding energy E_B is comparable to, or larger than the photon energy $h\nu$, i.e., $E_B \simeq h\nu$. An interaction between a photon and a tightly bound electron is considered an interaction between a photon and the atom as a whole.

- Type of interaction (photon disappearance or photon scattering), as shown in Table 4.3.
- Type of particle released (electron or positron), as shown in Table 4.4.

TABLE 4.1: Most important photon interactions with atoms of the absorber.

	Interaction
1.	Thomson scattering
2.	Rayleigh scattering
3.	Compton scattering
4.	Photoelectric effect
5.	Nuclear pair production
6.	Triplet production
7.	Photodisintegration

TABLE 4.2: Types of targets in photon interactions with atoms (orbital electrons or nuclei).

Photon-orbital electron interactions	**Photon-nucleus interactions**
With bound electrons: - Photoelectric effect - Rayleigh scattering	With nucleus directly: - Photodisintegration
With "free electrons" - Thomson scattering - Rayleigh scattering	With Coulomb field of nucleus - Nuclear pair production
With Coulomb field of electron - Triplet productions	

As far as importance to medical physics and radiation dosimetry is concerned, photon interactions with atom of absorber are classified into four categories:

1. *Interactions of major importance:*
   - Photoelectric effect
   - Compton scattering by "free" electron
   - Pair production in the field of nucleus
2. *Interactions of moderate importance:*
   - Rayleigh scattering
3. *Interactions of minor importance:*
   - Photonuclear reaction (also known as photonuclear effect)
   - Thomson scattering by "free" electron

TABLE 4.3: Types of photon-atom interactions (complete photon absorption or photon scattering).

Complete absorption of photon	**Photon scattering**
Photoelectric effect	Thomson scattering
Nuclear pair production	Rayleigh scattering
Triplet production	Compton scattering
Photodisintegration	

TABLE 4.4: Release and production of charged particles in photon interactions with absorber atoms.

Result of interaction	**Interaction event**
1. No charged particles released or produced	Thomson scattering Rayleigh scattering
2. Only electrons released	Photoelectric effect Compton scattering
3. Electrons and positrons produced and released	Nuclear pair production Triplet production

4. *Negligible interactions:*

   - Thomson scattering by the nucleus
   - Compton scattering by the nucleus

Regarding the interactions of major importance (photoelectric effect, Compton scattering and pair produtcion), the relative importance between these three different mechanisms depends both on the energy of the incident photon E and on the atomic number Z of the absorber, as shown in Figure 4.1. In the photoelectric effect, the cross section is characterized by a strong dependence on the atomic number Z, and it mainly contributes to the total cross section for energies smaller than 300 keV. The Compton cross section, instead, depends linearly on Z and it became relevant in the energy range between 0.1 MeV and 2 MeV. By increasing the photon energy, for energies higher than 10 MeV, the emission of electron-positron pairs becomes possible: in this case the cross section is proportional to the square of the atomic number of the absorber medium.
The other types of radiation interaction with matter are characterized by cross sections much smaller than those of the three dominant effects mentioned above, of about two order of magnitude (see Figure 4.2), and they became relevant at higher photon energies.

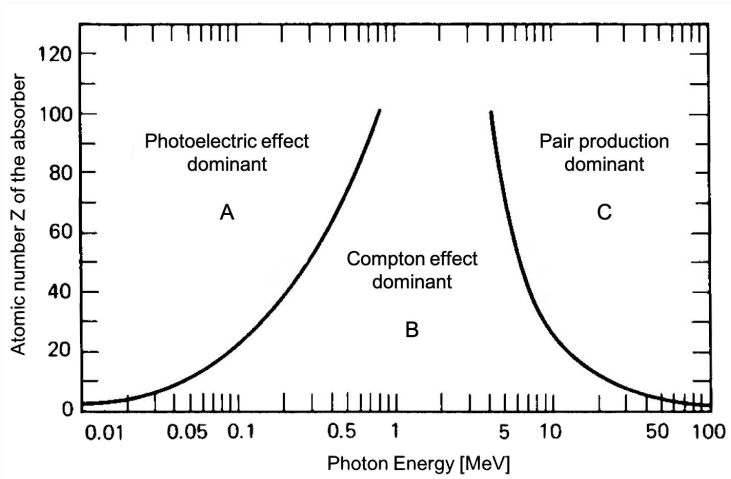

FIGURE 4.1: Representation of the relative predominance of the three main processes of photon interaction with absorber atom: photoelectric effect, Compton scattering and pair production (from [33]). The two curves connect points where photoelectric and Compton cross sections are equally probable shown by the curve on the left, and Compton and pair production cross sections are equally probable shown by the curve on the right. The photoelectric effect is dominant for low photon energies (region A), the Compton effect is dominant in the central area (region B), while pair production becomes important at higher energies (region C).

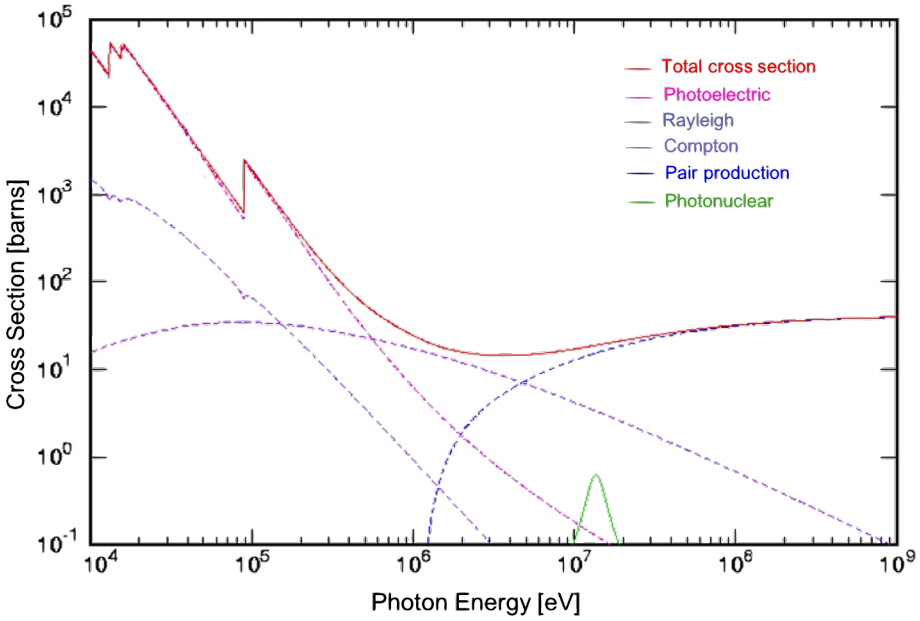

FIGURE 4.2: Cross sections of the different types of radiation interaction with matter for Pb-208 (from [34]). The photonuclear cross section, green line, is about two orders of magnitude lower than the dominant ones.

4.2 Photonuclear reactions (Photodisintegration)

Photonuclear reaction occurs in a direct interaction between an energetic photon and an absorber nucleus causing nuclear disintegration:

$$A^*(Z,N) \rightarrow A_1(Z-x, N-y) + A_2(x,y) \tag{4.1}$$

Two other names are often used for the effect: "photodisintegration" and "nuclear photoelectric effect".
In photonuclear reaction the nucleus absorbs a photon and the most likely result of such an interaction is the emission of:

- a single neutron through a (γ, n) reaction
- charged particles, such as protons or alpha particles
- gamma rays
- more than one neutron, or fission fragments (photofission), but much less likely to occur.

Neutrons produced in photonuclear reactions are referred to as *photoneutrons*.

Photonuclear reactions are endothermic[3], thus for the reaction to occur the incident photon must possess minimum or threshold energy to be able to trigger the reaction:

$$E_{th} = (M_{A_1}c^2 + M_{A_2}c^2) - M_A c^2 \tag{4.2}$$

The threshold energy represents the separation energy of a neutron from the nucleus that is of the order of 8 MeV or more for most nuclei, except for the deuteron (^{2}H) and berillium-9 (^{9}Be) where it is at 2.225 MeV and 1.665 MeV, respectively [35].

Cross section and threshold energy for photonuclear reaction

The cross sections for photonuclear reactions vary as a function of photon energy as well as the absorber nucleus, as described by the Levinger and Bethe formula [36]:

$$\int_0^\infty \sigma(E)dE = \frac{2\pi^2 e^2 \hbar}{Mc}\frac{NZ}{A} = 60\frac{NZ}{A} \tag{4.3}$$

where σ is the cross section expressed in [mbarn]; E is the incident photon energy in [MeV]; $\hbar$ is the reduced Planck's constant [eV s]; M is the mean nucleon mass (Mc^2= 938.926 MeV); c is the speed of light [cm s^{-1}]; N the neutron number; Z the proton number; A=N+Z is the number of nucleons in a nuclide.

The most notable features of the cross section for nuclear absorption of energetic photons are the reaction threshold and the so-called "giant resonance", both depending on the absorbing material.
The giant resonance is due to the acquisition of an electric dipole moment induced at high frequency by the nucleus. This dipole is generated by the absorption of photons with energies range between 10 MeV and 30 MeV, inducing a relative displacement of protons and neutrons enclosed in the nucleus itself, as shown in Figure 4.3.

[3] A collision is termed *endothermic* if the so-called *Q-value* of the reaction is < 0. To take place, the collision requires an energy transfer from the projectile to the target.
Notice that if the neutron energy $E_n \ll Q$, the momentum of the produced particle is $p_1 \approx$ -p_2 and E_1+$E_2 \sim Q$.

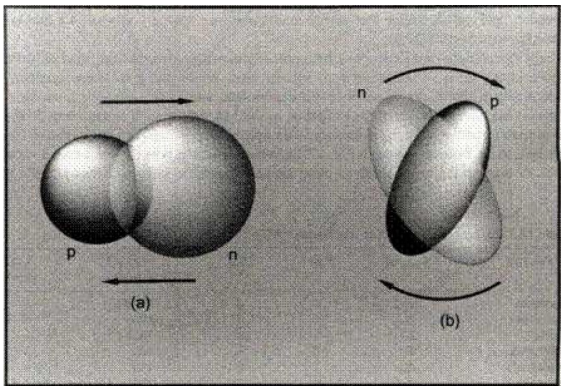

FIGURE 4.3: Electric dipole oscillation of the nucleus. The neutron and the proton oscillate relative to each other translationally (a) or rotationally (b).

For heavy nuclei, the giant resonance decays predominantly with the emission of a neutron; for higher incident photon energies it is also possible the (γ, 2n) reaction. The (γ, p) is instead strongly depressed due to the high value of the Coulomb barrier, which exceeds the giant resonance threshold of heavy nuclei.
For light nuclei, on the other hand, the (γ, p) and the (γ, n) reactions are equally probable: this is due to the compensation between the reduction of the Coulomb barrier and the partial increase of the neutron separation energy.

Neutrons from giant resonance are isotropically emitted, they have a mean energy of about 1 MeV and a maximum energy of the order of 10 MeV [37].

The photonuclear absorption cross section is proportional to the atomic number Z of the target nucleus, as seen in equation 4.3. Above the photon threshold energy the cross section gradually increases, reaches a broad peak referred to as giant resonance, and then decreases with a further increase in photon energy. The giant resonance peak is centered at about 23 MeV for low atomic number Z absorbers and at about 12 MeV for high Z absorbers. Figure 4.4 shows the cross section trend of the reaction (γ, n) on two different materials, with high and low atomic number, Tungsten-186 (a) and Carbon-12 (b), respectively [38].
The full-width-at-half-maximum (FWHM) in the giant resonance cross sections typically ranges from about 3 MeV to 9 MeV and it depends on the detailed properties of absorber nuclei.
Table 4.5 provides various parameters of the "giant (γ, n) resonance" cross section for selected absorbers, for those of interest in radiotherapy.
The threshold energy for the photoneutron reaction is lower for heavy elements, the giant resonance peak is reached at lower energies and it is about twenty times higher than light elements. The (γ, n) reaction is therefore more important for high-Z nuclei.

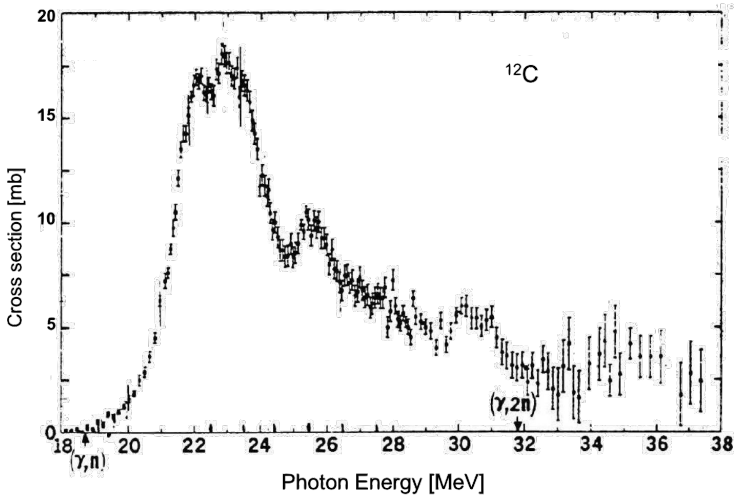

(A) Photoneutron cross section for ^{12}C. The giant dipole resonance is at 23 MeV, in which the resonance peak value is 20 mb. The vertical small arrows point out the threshold energies for the (γ, n) and (γ, 2n) reactions, respectively. The threshold energy for the (γ, n) reaction is 18.7 MeV.

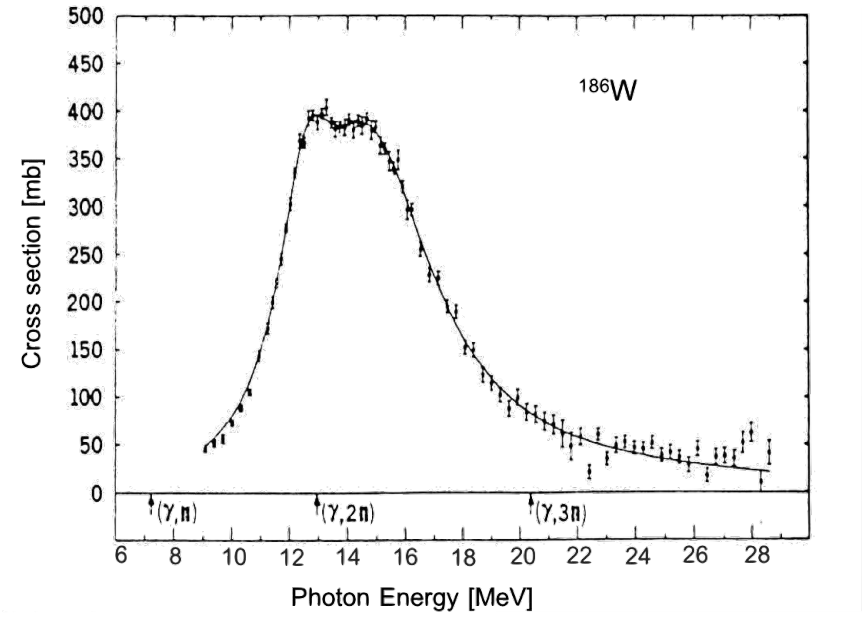

(B) Photoneutron cross section for ^{186}W. The giant dipole resonance is at 13.5 MeV, in which the resonance peak value is 400 mb. The vertical small arrows point out the threshold energies for the (γ, n), (γ, 2n) and (γ, 3n) reactions, respectively. The threshold energy for the (γ, n) reaction is 7.42 MeV.

FIGURE 4.4: Cross section of the photoneutron production reaction for two different nuclides: Carbon-12 and Tungsten-186. [38]. The threshold energy for the photonuclear reaction is lower for heavy nuclei, and the resonance peak is about twenty times higher than light elements, and it is reached at lower energies: the photonuclear reaction is more relevant for high atomic number of absorbers.

TABLE 4.5: Photonuclear (γ,n) giant resonance cross section parameters for selected absorbers [39].

High-Z absorber σ_{max} ~400 mb	**Threshold energy** [MeV]	**Low-Z absorber** σ_{max} ~ 20 mb	**Threshold energy** [MeV]
Pb-208	7.41	C-12	18.7
W-184	7.42	O-16	15.7
Cu-63	9.00	Ca-40	15.6
Fe-56	10.9	P-31	12.3

4.3 Interactions of neutrons with matter

Neutrons are indirectly ionizing radiation exhibiting a quasi-exponential penetration into an absorber and depositing energy in the absorber through a two-step process:

1. energy transfer to heavy charged particle
2. energy deposition in the absorber through Coulomb interactions of these charged particles with atoms of the absorber.

As they penetrate into matter, neutrons may undergo elastic and inelastic scattering as well as trigger nuclear reactions, such as neutron capture, spallation, and fission.

4.3.1 General aspects of neutron interactions with absorbers

Neutrons, similarly to photons, may penetrate an absorber without interacting or they may undergo various interactions with the absorber. In contrast to photons, however, neutrons interact mostly with the nuclei of the absorber and have only minor interactions with orbital electrons of the absorber.
Neutron beams, similarly to photon beams, belong to the category of indirectly ionizing radiation beams, both types transferring energy to absorbing medium through an intermediate step in which energy is transferred to a charged particle (protons and heavier nuclei in the case of neutrons; electrons and positrons in the case of photons).
The secondary heavy charged particles released in a medium traversed by neutrons have a very short range in the medium.

In terms of their kinetic energy E_K, neutrons are classified into several categories:

1. *Ultracold neutrons* with $E_K < 2 \times 10^{-7}$ eV
2. *Very cold neutrons* with 2×10^{-7} eV $\leq E_K \leq 5 \times 10^{-5}$ eV
3. *Cold neutrons* with 5×10^{-5} eV $\leq E_K \leq 0.025$ eV
4. *Thermal neutrons* with $E_K \approx 0.025$ eV
5. *Epithermal neutrons* with 1 eV $< E_K <$1 keV
6. *Intermediate neutrons* with 1 keV$< E_K <$ 1 MeV
7. *Fast neutrons* with $E_K >$ 1 MeV.

Of the seven categories listed above, only thermal, epithermal, and fast neutrons are used in medicine and are thus of interest in medical physics[4].

In this work, neutrons are named:

- **THERMAL** if their energy is up to 0.4 eV;
- **EPITHERMAL** if 0.4 eV $< E <$100 keV;
- **FAST** for energies greater than 100 keV.

4.3.2 Neutron interactions with nuclei of the absorber

Neutrons can approach a target nucleus without any interference from a Coulomb repulsive or attractive force, since they, unlike protons and electrons, are not affected by electric charge. Once in close proximity to the target nucleus, neutrons can interact with it through the short range attractive nuclear potential and trigger various nuclear reactions.
There are five principal processes by which neutrons interact with the nuclei of the absorber:

1. Elastic scattering
2. Inelastic scattering
3. Neutron capture
4. Nuclear spallation
5. Nuclear fission

In general, it is possible to describe the interaction of a neutron with a nucleus A(Z, n) like the formation of an excited nucleus A*(Z, N + 1):

$$A(Z,N) + n \rightarrow A^*(Z,N+1) \tag{4.4}$$

After a typical time of the order of (10^{-12} - 10^{-13}) s the nucleus A*(Z, N + 1) is de-energized by the emission of one or more particles.
The probability (cross section) for these different types of interactions varies with the kinetic energy of the neutron and with the physical properties of the nuclei of the absorber.

Elastic scattering

In elastic scattering a neutron collides with a nucleus of mass M that recoils with an angle ϕ with respect to the neutron initial direction of motion, as shown schematically in Figure 4.5 for general two-particle elastic scattering. Kinetic energy and momentum are conserved in the interaction.

[4]Note that the velocity of an ultracold neutron with a kinetic energy of 2 $\times 10^{-7}$ eV is $\sim$ 6 m/s; of a thermal neutron with a kinetic energy of 0.025 eV it is $\sim$ 2200 m/s; and of a fast neutron it is 1.4 $\times 10^{7}$ m/s.

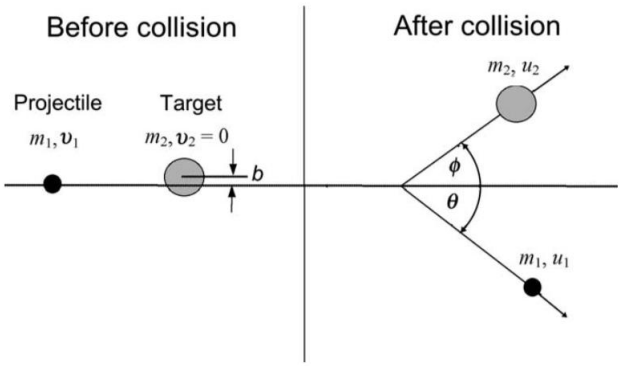

FIGURE 4.5: Schematic diagram of an elastic collision between a projectile with mass m_1 and velocity v_1 striking a stationary target m_2. The projectile is scattered with a scattering angle θ; the target recoils with a recoil angle ϕ. The impact parameter is b. After the collision the velocity of the projectile m_1 is u_1; the velocity of the target m_2 is u_2.

For a neutron with mass m_n and initial kinetic energy $(E_K)_i$, the kinetic energy ΔE_K transferred to the nucleus is in general given by:

$$(\Delta E_K)_{max} = E_K \frac{4m_n M}{(m_n + M)^2} \cos^2 \phi \tag{4.5}$$

The maximum possible energy transfer (ΔE_K) is attained in a head-on collision for which ϕ = 0°C

$$(\Delta E_K)_{max} = |\Delta E_K|_{\phi=0} = (E_K)_i \frac{4m_n M}{(m_n + M)^2} \tag{4.6}$$

The average kinetic energy $\Delta \bar{E}_K$ transferred to the recoil nucleus is

$$\Delta \bar{E}_K = \frac{1}{2}(\Delta E_K)_{max} = \frac{1}{2}(E_K)_i \frac{4m_n M}{(m_n + M)^2} = 2(E_K)_i \frac{m_n M}{(m_n + M)^2} \tag{4.7}$$

The kinetic energy of the scattered neutron, $(E_K)_f$, in a head-on collision is equal to

$$(E_K)_f = (E_K)_i - (\Delta E_K)_{max} = (E_K)_i (\frac{m_n - M}{m_n + M})^2 \tag{4.8}$$

while $(\bar{E}_K)_f$, the average energy attained by the scattered neutron, is

$$(\bar{E}_K)_f = (E_K)_i - (\Delta \bar{E}_K)_{max} = (E_K)_i \frac{m_n^2 + M^2}{(m_n + M)^2} \tag{4.9}$$

Thus, for example, if the target nucleus is hydrogen (nucleus is a proton with mass m_p), then $M = m_p \approx m_n$ and the neutron will transfer on the average one half of its initial kinetic energy to the proton [see Eq. 4.6], while the maximum energy transferred to the proton equals to the initial neutron energy $(E_K)_i$ [see Eq. 4.9]. The recoil proton will then travel a short distance through the absorbing medium and rapidly transfer its kinetic energy to the medium through Coulomb interactions with the nuclei and orbital electrons of the medium. This interaction could thus be used for moderating fast neutron.

The transfer of neutron energy to the absorbing medium is much less efficient when $m_n \ll M$; the larger is M, the less efficient is the energy transfer, as evident from Eq. 4.6. For example, Eq. 4.6 predicts an only 2% fractional energy transfer from a neutron colliding head-on with a lead nucleus, compared to a 100% energy transfer in a head-on neutron-proton collision.

Except for some resonance peaks, at low energies the cross sections decrease rapidly as the energy of the neutrons increases, while they decrease more slowly at higher neutron energies, as shown for example in Figure 4.6, green solid curve, for hydrogen.

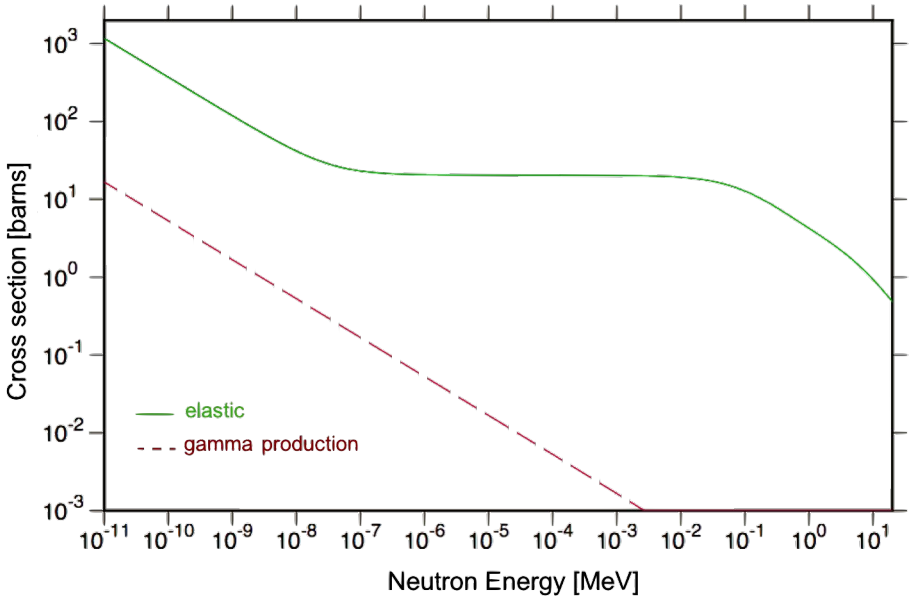

FIGURE 4.6: Cross section of the ${}^1H(n,n'){}^1H$ reaction (green solid curve) and of the ${}^1H(n,\gamma){}^2H$ reaction (red dashed curve) [38].

Inelastic scattering

In inelastic scattering the neutron n is first captured by the nucleus and then re-emitted as neutron n' with a lower energy and in a direction that is different from the incident neutron direction. The nucleus is left in an excited state and will de-excite by emitting high-energy γ rays. This process is illustrated by the following relationship

$$n + {}^A_Z X \rightarrow {}^{A+1}_Z X^* \rightarrow {}^A_Z X^* + n' \Rightarrow {}^{A+1}_Z X^* + \gamma \tag{4.10}$$

where:
${}^A_Z X$ is the stable target nucleus
${}^{A+1}_Z X^*$ is an unstable compound nucleus
${}^A_Z X^*$ is an excited target nucleus.

Neutron capture

Neutron capture is a term used to describe a nuclear reaction in which a thermal neutron bombards a nucleus leading to the emission of a proton, γ ray, as well as deuterons, tritons, ^{3}He, alphas... Two of these interactions are of particular importance in tissue: $^{14}N(n,p)^{14}C$ and$^1H(n,\gamma)^2H$, in which the last one emits γs at 2.2 MeV.
In Figure 4.6 it is also shown the neutron capture cross section trend as a function of the incident neutron energy (red curve). Decreasing the energy, the cross section is inversely proportional to the neutron velocity.

Spallation

Spallation is in general defined as fragmentation of a target into many smaller components as a result of impact or stress. Consequently, nuclear spallation is defined as disintegration of a target nucleus into many small residual components such as αparticles and nucleons (protons and neutrons) upon bombardment with a suitable projectile such as light or heavy ion beams or neutrons.
An example of spallation is as follows

$$^{16}_{8}O + n \rightarrow 3\alpha + 2p + 3n \tag{4.11}$$

Most of the energy released from the spallation process is carried away by the heavier fragments that deposit their energy in the absorber locally. On the other hand, neutrons and de-excitation γ rays produced in spallation carry their energy to a remote location. Spallation can be used for production of radionuclides and for generation of neutron beams in spallation neutron generators.
This process becomes important at neutron energies higher than 20 MeV. Considering that in radiotherapy the neutron spectrum for giant resonance does not exceed energies of 10 MeV (see par. 4.2), it is here reported only for completeness.

4.4 Neutron dosimetry

Neutron dosimetry is a particularly challenging pursuit and it is important in many exposures of human health, both in the medical and environmental fields. The most important interactions of neutrons with elements that mainly constitute the human body (H, C, N, O) are described here, in order to evaluate the risk patients are exposed during radiotherapy.

4.4.1 Neutron riskiness for human tissues and organs

The fundamental interaction for neutrons with energies range between 100 keV and 20 MeV is the elastic scattering with hydrogen nuclei.
Soft tissues consist of 0.10 hydrogen mass fraction. The dominant reaction is $^1H(n,n)^1H$, contributing for the 97% to the neutron dose with initial energy of 10 keV, for the 87% to 8 MeV and for the 70% to 18 MeV. The involved processes, in order of importance, are the elastic scattering with oxygen, carbon and nitrogen nuclei. The inelastic and capture processes equal these ones in importance only when neutrons reach energies of about 10 MeV.

The emitted charged particles by the interaction of neutrons have a high LET. For example, the mean energy of a recoil proton produced by a 20 MeV neutron is worth

about 10 MeV, and its mean path in water is 1.2 mm: the energy transferred from the initial neutron will be absorbed very close to the interaction point when compared to typical cells sizes (a few tens of μm). The neutron interactions with matter thus regulate energy depositions in small volumes of tissue.

Diffuse neutrons suffer multiple collisions with the human body, and they are thermalized at the end. Once they are moderated the capture reaction on nitrogen $^{14}N(n,p)^{14}C$ occurs, emitting a 0.62 MeV proton.
Another important low-energy reaction is $^{1}H(n,\gamma)^{2}H$, that emits a 2.2 MeV photon. This is to be added to the gammas of de-energization resulting from inelastic scattering and capture reaction produced by high energy neutrons. With considerable tissue thicknesses like those in humans, γ rays tend to be absorbed.

Water-rich tissues are very sensitive to neutron action. Hydrogen nuclei, elastically diffused by the incident neutron, acquire a certain kinetic energy causing an intense ionization. This implicates a production of free radicals[5].
Free radicals, with high chemical aggressiveness, react with others stable molecules of the organism and increase the presence of hydrogen peroxide, which is also particularly reactive, so that its presence inside tissues is deleterious.
The incident radiation alters the molecules by activating an interaction process chain with other molecules.
The events that contribute to the damage of biological system are essentially:

- the breakdown of molecular bonds;
- the transport of energy;
- the transmission to macromolecules of the damage suffered by small molecules.

Moreover, for the biological effectiveness, it's important the spatial distribution of the produced ions: a higher ionization density implies a greater biological damage.

Therefore, it is of crucial importance to estimate the neutron dose which patients are exposed, in order to achieve radiation protection. Radiation protection problems related to neutron production are many:

- Neutrons are generally accompanied by intense photon fields, and it is so necessary to use detectors that discriminate between the two types of radiation.
- The intense electromagnetic field provided by accelerators imply off-line and passive measurements.
- The neutron energy spectrum covers several orders of magnitude, from 0.025 eV (thermal neutrons) to tens of MeV (fast neutrons): different interaction mechanisms occur and, thus, different detectors for different energies are necessary.
- The relative biological effectiveness, RBE, strongly depends on the neutron energy: it is so necessary to know the neutron spectrum in order to use the

[5]Free radicals are atoms or groups of atoms with an odd (unpaired) number of electrons and they can be formed when oxygen interacts with certain molecules. Once formed, these highly reactive radicals can start a chain reaction. Their chief danger comes from the damage they can do when they react with important cellular components such as DNA, or the cell membrane. Cells may function poorly or die if this occurs.

correct fluence - dose conversion factors, tabulated in ICRP 116 [40] for the ambient dose equivalent, and in NCRP 38 for the dose equivalent in tissue [41].

4.4.2 Characteristics of neutron dosimeters

As mentioned in the previous section, it is essential to understand the properties of not only the detector, but also the neutron field being measured in order to perform neutron dosimetry correctly. Most importantly, neutron detectors are sensitive to neutrons only in a particular energy range. Because detector responses to different neutron energies often varies by several orders of magnitude, it is critical to know the detector response function and how it is related to the neutron spectrum being measured. Moreover, because the primary photon beam is pulsed, passive detectors are generally preferred for measurements [42]

Basic features of a good dosimeter, taking into account the issues concerning neutron dosimetry listed above, are:

- dose-response linearity;
- independence from the incident radiation energy;
- high repeatability and great possibility of use;
- low loss of information over time, also according to the environmental conditions;
- low influence of background radiation.

In the case of personal dosimeters it must be added:

- handiness to use, in terms of shape and lightness;
- cost-effectiveness;
- coverage of a wide measurement range in terms of equivalent dose (from 0.1 mSv to 10 Sv);
- isotropic angular response;
- independence from the dose rate;
- response accuracy in order to meet the recommendations of the international commissions.

In this work thesis, neutron passive bubble dosimeters were employed to detect the neutron dose equivalent (see section 7.2).

4.5 Neutron photoproduction consequences

Undesirable radiation doses, delivered to patients during radiotherapy treatments, have been studied since the 1950s. In particular, the NCRP Report No. 79 [43], regarding the neutron contamination provided by medical linear accelerators, states that in the case of irradiation with X-ray there are several sources of absorbed doses outside the target volume. These sources must be added to the dose due to the primary beam and considered in the total risk to the patient.
For this reason, several studies have been addressed to the investigation of parasitic neutrons during radiotherapy treatments, with different dosimetric system (such as bubble detectors, polycarbonate film, activation detectors, thermoluminescance dosemeters), both in-field and out-of-field, especially in high-energy medical linear accelerators (25 MV, 18 MV, 15 MV) [44], [45], [46]. However, there is sparse information about photoneutrons provided in lower energies, near the GDR reaction threshold, at 10 MV and 6 MV.
Part of the thesis work (Chapter 9) was thus dedicated to performing measurements of the parasitic neutrons at low-energy LINAC. Considering the last developments in radiotherapy in performing more and more lower energy treatments, for example the 6 MV IMRT or VMAT treatments, also the 6 MV LINAC was taken into account, giving so a contribution to the present literature in this field [47].

4.5.1 Unaccounted neutron dose during radiotherapy

The undesirable dose components are not completely independent each other and, from a medical point of view, it must be considered the total risk to the patient.
Sources of extra doses are:

1. photons escaping from the shielding of the accelerator head
2. photons diffused outside the treatment volume
3. neutrons produced by the (γ, n) reaction on high Z elements constituting the LINAC head
4. neutrons produced by the (γ, n) reaction on light elements constituting the human body in the treatment area.

The first point is the best known: the problem of photon diffused from the accelerator head already existed, since the radiotherapy pioneers. The request made by the International Commission was to obtain a maximum level of diffused photon equal to 0.1% of the beam dose rate.
The second point, instead, depends on the field size: the component of photons diffused outside the treatment area is from 5 to 28 times greater than the value of photons escaping from the accelerator head.

The neutron issue arose when high energy accelerators were employed in radiotherapy for treating deeper tumours. Looking at the trend of the absorbed dose as a function of the depth in tissue, it varies according to the photon energy (see Fig. 1.1 or Fig. 3.8): the build-up moves towards greater distances by increasing the photon energy (2-4 cm for energies range 6-25 MeV).
The side effect of the use of high energy beams is, however, the neutron photoproduction, already described in par. 4.2. The neutron production results from the interaction of bremsstrahlung photons both (1) with high Z nuclei constituting the

LINAC head (lead, tungsten, iron..) and (2) with light elements constituting the human body (mainly on carbon, nitrogen and oxygen nuclei).
In the first case, neutrons are produced inside the LINAC gantry, with an isotropic angular distribution. These neutrons interact then with the human body, without any discrimination between healthy and sick tissues. While, in the second case, both the neutron production and transport take place inside the patient body.
Moreover, the photoneutron cross sections reach values of the order of hundreds of millibarn for heavy elements, and only up to a few tens of millibarn for light elements (see Fig. 4.4 for photoneutron cross sections and Tab. 4.5 for the (γ, n) threshold energies). As a matter of fact, the predominant neutron dose contribution is this due to the LINAC head: only 10% of the neutrons are directly produced inside the patient body in the treatment area.
According to the NCRP report No. 79, the neutron component is been estimated to be 0.1% - 0.3% of the photon dose.

4.5.2 Relationship between monitor units and unaccounted neutron dose

Photon beam collimation techniques, such as multileaf collimator (MLC), aim at increasing the local tumour control but require a longer time to deliver a certain dose to the target volume, increasing considerably the number of monitor units.

The Monitor Unit (MU) represents the request time for the LINAC to deliver a certain dose to the target volume. The monitor unit settings on the LINAC are calibrated in order to achieve an output of:

$$1cGy = 1MU \tag{4.12}$$

for a standard field size of (10 $\times$ 10) cm^2 at 100 cm SSD in a water phantom at build-up.

When the conditions differ from the reference ones, an accurate evaluation of the *output factor* (OF) has to be made:

$$OF = \frac{D_{abs}}{D_{ref}} \tag{4.13}$$

where D_{abs} is the photon dose absorbed by the patient at build-up, and D_{ref} is the reference dose.

In this way, the new MU can be calculated as:

$$MU = \frac{D_{pr}}{D_r \cdot OF} \tag{4.14}$$

where D_{pr} is the prescription dose for the treatment, and $D_r = cGy/MU$

For example, 100 MU are necessary to deliver a dose of 1 Gy at build-up for a photon field size of (10 $\times$ 10) cm^2; to deliver the same dose, keeping opened the secondary collimators at (10 $\times$ 10) cm^2 and by using MLCs in clinical configuration, 103 MU are necessary because multileaf collimators shield the primary photon beam.

This is what happens during an intensity modulated radiation therapy IMRT, where the dose is delivered in little segments and the photon beam is semi-shielded by

the leaves. Therefore, to deliver the prescription dose to the patient by covering the whole target volume many segments are necessary: this requires a longer treatment time and, consequently, more MU.

It's important to point out that monitor units are also related to the parasitic neutron dose: in fact, MLCs are made by high Z elements, increasing thus the neutron photoproduction.

In Table 4.6 the necessary MUs to deliver 1 Gy at build-up for different kinds of treatment for a photon field size of (10×10) cm^2 are reported.

TABLE 4.6: Monitor units per Gy of photon dose delivered at build-up for a photon field size of (10×10) cm^2.

Treatment	**Total dose** [Gy]	**Monitor Unit** [MU/Gy]
Traditional	70	100
Traditional + blocks	70	100
Traditional + MLC	60-80	185-290
IMRT	70	1815

Chapter 5

The Boron Neutron Capture Therapy

During radiotherapy, a large radiation dose is delivered to a tumour aiming at destroying or damaging cancer cells, while the dose to the surrounding healthy tissues must be limited to a tolerable level. The effectiveness of the treatment depends on the radiation dose delivered to the tumor target and on the dose accuracy.

One of the technique of high-selectivity radiotherapy is the Neutron Capture Therapy (NCT): the idea behind this therapy is to selectively target tumour cells by high linear energy transfer (high-LET) heavy particle radiation, which is released when a tumor-seeking compound is exposed to a neutron field [48].

This chapter gives an overview of the neutron capture therapy on boron-10, describing its physical, chemical and biological characteristics.

5.1 Therapy of the neutron capture on boron-10

It was the physicist G.L. Locher who proposed the idea of using neutron capture reactions, in which a ^{4}He nucleus (alpha particle) and ^{7}Li nucleus are emitted when ^{10}B reacts with thermal neutrons, to destroy cancer cells in cancer treatment. It was 1936, four years after the discovery of the neutron. This is the origin of the Boron Neutron Capture Therapy (BNCT).

BNCT is a two-step procedure:

1. a boron-10 enriched compound is administrated to the patient;
2. the target volume is irradiated by slow neutrons (thermals or epithermals) because of their high absorption cross section on boron-10.

After losing energy as they penetrate tissue, the neutrons are absorbed by the capture agent, which subsequently emits high-energy charged particles that can selectively kill tumor cells that have taken up sufficient amounts of boron-10, [49].

The nuclear reaction

Thermal neutrons are captured by a variety of nuclei, but the probability of capture by a ^{10}B nucleus (expressed in terms of the capture cross-sectional area in cm^2) is much higher than other elements constituting human tissue, such as hydrogen, oxygen, and nitrogen, since its cross-section (3843 barns at 0.025 eV) is, for example, about 2.000 times larger than the nitrogen one [4].

During the neutron irradiation, a nuclear reaction takes place

$$n + {}^{10}B \rightarrow {}^{11}B^* \rightarrow \alpha + {}^{7}Li + 2.79MeV \quad [6\%] \tag{5.1}$$

$$n + {}^{10}B \rightarrow {}^{11}B^* \rightarrow \alpha + {}^{7}Li + \gamma(0.48MeV) + 2.31MeV \quad [94\%] \tag{5.2}$$

producing high-LET heavy fragments from ^{10}B, an α particle (^{4}He) and a 7-lithium (^{7}Li) nucleus (Figure 5.1).
The track ranges of the two emitted particles are extremely short (of the order of few μm) and do not exceed the diameter of a typical cell (see Figure 5.2): the destructive effects are limited to boron-containing cells, thereby selectivity destroying only tumour cells during neutron irradiation if the carrier transporting boron is selective. [50].

The ionization density produced by the α particle along the path inside the cell gives birth to an electric field: it segments the two DNA helices at the same height, inactivating the cell itself. Despite the high-LET of ^{7}Li, it rarely causes serious damage to the nucleus. The destructive effects are thus due to α particles.

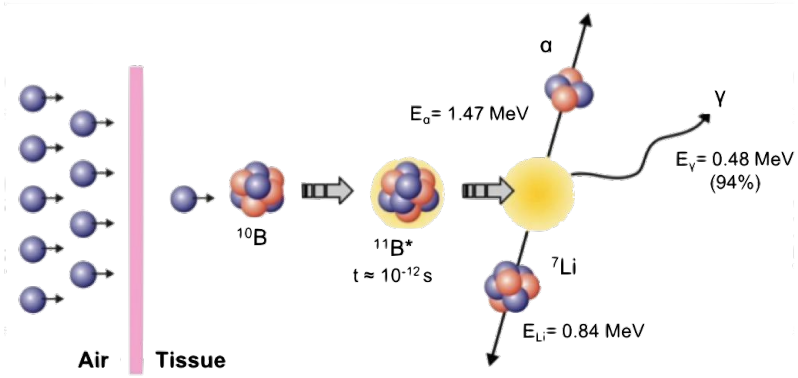

FIGURE 5.1: Nuclear reaction in BNCT. Boron neutron capture therapy is based on the nuclear capture and fission reactions that occur when non-radioactive boron-10, a constituent of natural elemental boron, 80% of which is in the isotopic form of ^{11}B and 20% as ^{10}B, is irradiated with low-energy (0.025 eV) thermal neutrons or, alternatively, higher-energy (10 keV) epithermal neutrons. The latter become thermalized as they penetrate tissues. The resulting ^{10}B(n,α)^{7}Li capture reaction yields high linear energy transfer α particles and recoiling lithium-7 atoms, emitted in opposite directions.

The nuclear reaction in BNCT is so favourable in radiotherapy because of:

- the high capture cross section for thermal neutrons (3843 barns at 0.025 eV)
- the positive Q-value (Q = 2.792 MeV)
- the reaction products release their energy inside the cell where they have been created.

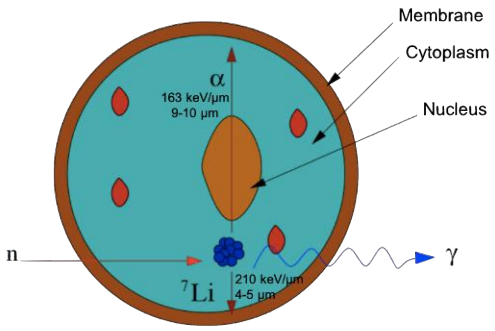

FIGURE 5.2: Schematic representation of the boron fission reaction inside the cell. α particle: LET of 163 keV/μm and pathlength of 9-10 μm; ^{7}Li: LET of 210 keV/μm and pathlength of 4-5 μm. The α particles destructive effects are limited to boron-containing cell. Notice also that a sufficient amount of ^{10}B must be delivered selectively to the tumor (∼20-50 μg/g or $\sim 10^9$ atoms/cell) in order for BNCT to be successful.

- the boron-10 concentration ratio in tumour cells is higher than healthy ones (typically 3:1, even if it can reach higher uptake values [51]), thanks to the high boron carrier absorption for cells which replicate faster.

Radiobiological considerations

The radiation doses delivered to tumour and normal tissues during BNCT are due to energy deposition from three types of directly ionizing radiation, that differ in their LET (the rate of energy loss along the path of an ionizing particle):

1. low LET gamma rays, resulting primarily from the capture of thermal neutrons by normal tissue hydrogen atoms

$$n + {}^{1}H \rightarrow {}^{2}H + \gamma \tag{5.3}$$

2. high LET protons, produced by the scattering of fast neutrons and from the capture of thermal neutrons by nitrogen atoms

$$n + {}^{14}N \rightarrow p + {}^{14}C \tag{5.4}$$

3. high LET, heavier charged alpha particles (stripped down helium [^{4}He] nuclei) and lithium-7 ions, released as products of the thermal neutron capture and fission reactions with ^{10}B

$$^{10}B(n,\alpha)^{7}Li \tag{5.5}$$

Since both tumour and surrounding normal tissues are present in the radiation field, there will be an unavoidable, nonspecific background dose, consisting of both high and low LET radiation. However, a higher concentration of ^{10}B in the tumour will result in it receiving a higher total dose than that of adjacent normal tissues, which is the basis for the therapeutic gain in BNCT [52]. The total radiation dose in Gy delivered to any tissue can be expressed in photon-equivalent units as the sum of each of the high LET dose components multiplied by weighting factors, which depend

on the increased radiobiological effectiveness of each of these components (see par. 5.2.1)

Boron delivery agents

Research in the area of development of boron-containing delivery agents for BNCT started ∼50 years ago with the investigation of a large number of low molecular weight boron compounds.
The most important requirements for a BNCT delivery agent are [53]:

1. low toxicity and normal tissue uptake, with a tumor:normal tissue and tumor:blood boron concentration ratios of >3:1
2. tumor boron concentration of ∼20 μg ^{10}B/g tumor
3. relatively rapid clearance from blood and normal tissues, and persistence in tumour during neutron irradiations.

The only two BNCT delivery agents currently used in clinical trials are sodium *mercaptoundecahydro-closo-dodecaborate*, commonly known as sodium borocaptate (BSH), and the boron-containing amino acid *(L)-4-dihydroxy-borylphenylalanine*, known as boron-phenyl-alanine or BPA [54].
However, with the development of new synthetic techniques and increased awareness of the biochemical requirements needed for effective boron containing agents and their modes of delivery, a number of new boron agents are emerging: the so-called "third generation agents". The major challenge in the development of such agents is the requirement for selective tumour cell targeting, the delivery of therapeutic boron levels with minimal normal tissue toxicity, and the ability to exceed the biological barrier, the blood-brain barrier (BBB), that BPA cannot do.

5.2 Overview of BNCT dosimetry

5.2.1 Dose components

The typical BNCT radiation field produced in normal and tumour tissues consists of a mixture of several particles, such as neutrons, protons, photons, α particles and ^{7}Li particles.

In the physical dose estimation, these particles are categorized into four major dose components [55]:

1. GAMMA DOSE
$$^{1}H + n \longrightarrow {}^{2}H + \gamma + 2.2MeV \tag{5.6}$$
The gamma dose consists of two components: primary photons accompanying the neutron beam and secondary photons produced by the thermal neutron capture reaction on hydrogen in tissue. The gamma dose is written as D_γ.

2. BORON DOSE
$$^{10}B + n \longrightarrow {}^{11}B \longrightarrow {}^{7}Li(0.84MeV) + \alpha(1.47MeV) + \gamma(0.48MeV)(94\%)$$
$$^{10}B + n \longrightarrow {}^{11}B \longrightarrow {}^{7}Li(1.01MeV) + \alpha(1.78MeV)(6\%) \tag{5.7}$$

The boron dose is due to the neutron capture reaction by ^{10}B that absorbs a thermal neutron. The energetic emitted α particle and the recoil ^{7}Li ion result in locally deposited energy averaging about 2.34 MeV. About 94% of the times the recoiling ^{7}Li ion is produced in an excited state and de-excites emitting a 480 keV gamma ray. In the remaining events, the ^{7}Li is emitted in the ground state with no gamma ray emission. The boron dose is written as D_B.

3. NITROGEN DOSE or THERMAL NEUTRON DOSE

$$^{14}N + n \longrightarrow {}^{14}C + p + 0.66MeV \tag{5.8}$$

The nitrogen dose consists of a locally deposited dose from energetic protons (660 keV) and recoiling ^{14}C nuclei from the thermal neutron absorption reaction on nitrogen nuclei in tissue. The nitrogen dose is written as D_N.

4. HYDROGEN DOSE or FAST NEUTRON DOSE

The hydrogen dose is mainly due to proton recoil reactions at higher neutron energies (>10 keV) in the tissue. Protons, produced by ^{1}H(n,n')p reaction, deposit their energy locally. This dose component is the highest one at the skin surface and decreases exponentially with depth. The hydrogen dose is written as D_H.

The boron dose accounts for the majority of the biological effect in tumor tissues [56]. The other dose components deliver background doses to both normal and tumor tissues [57]. The minimum requirement for effective BNCT has been estimated to be 10^9 - 10^{10} boron atoms distributed uniformly throughout a tumour cell [58].

The BNCT dosimetry, therefore, requires a careful analysis of the different components of the radiation field.
In order to compare the BNCT dose with the fractionated absorbed dose in photon radiotherapy, the physical dose needs to be converted to biological dose: each of the four major dose components is so multiplied by their *relative biological effectiveness* (RBE)[1] using a *weighting factor* (w_i).

The total BNCT *weighted absorbed dose* in photon dose equivalent units, *weighted Gray* [Gy-eq] can be defined as follows:

$$D_W = w_\gamma D_\gamma + w_B D_B + w_N D_N + w_H D_H \tag{5.9}$$

The w_i are energy and dose rate-dependent and thus, are also dependent on individual beam characteristics and scattering conditions (location in the body). In addition, the biological effectiveness is dependent on the tissue. Moreover, synergy between the various radiation components is indicated, which results in a greater biological effect than would be in the case of the independent action of the various radiation types [59].
Nonetheless, constant values for the w_i values are commonly applied, regardless of the tissue: w_γ =1[2], w_H and w_N = 3.2 [58], [61].

[1] RBE is defined as the ratio of doses of a reference radiation (currently cobalt-60 gamma rays) to a test radiation that will produce the same biological endpoint in a given system.

[2] In other works [60] for long irradiation times (2-3 hours) w_γ is assumed 0.5 because a cell survival probability can be enhanced from repair of sublethal damage.

The w_i for D_B is called the *compound biological effectiveness* factor (CBE), since it is not only dependent on the radiosensitivity of the tissue, but also on the boron carrier applied and its micro-distribution inside the cell. In fact, the boron located in the nucleus is more effective than boron distributed in the cytoplasm, which is in turn more effective than boron attached to the cell membrane. The CBE factors or w_B usually employed are: 3.8 in the tumor tissue, 1.3 in healthy tissues and 2.5 for skin, measured by Coderre et al. [58].

Regarding the physical dose components, D_H and D_N are dependent on the hydrogen and nitrogen mass fraction and the mass density of the tissue (most commonly, elemental compositions of tissues are defined according to ICRU Report 46 [62]). While for calculation of the physical D_B, the boron concentration of tissue needs to be evaluated: the blood boron concentration during neutron irradiation is commonly from about 11 parts per million (ppm) to 30 ppm, depending on the BPA infusion dose [63].

5.2.2 Dose calculation

The absorbed dose in BNCT is due to nuclear interactions and thus the computational approximations in use for photon and electron therapy cannot be adopted for BNCT dose planning. To calculate the neutron interactions within the body, the elemental composition of organs needs to be modeled.

One of the recommended codes for BNCT dosimetric calculations is the Monte Carlo N-Particle (MCNP) radiation transport code [64].
The dose components are calculated by integrals such as:

$$D_{n,B} = \frac{1}{\rho_m \cdot V} K_{n,B} \int dV \int dE \cdot E_{coll} \cdot \phi(E) \cdot \rho_a \cdot \sigma_a \tag{5.10}$$

where:

- V is the cell volume in [cm^3], ρ_m is the biological tissue density in [$g \cdot cm^{-3}$]. Their product is the cell mass expressed in [g];
- $K_{n,B}$ is a constant depending on the particle type (neutron here) and on the biological material (normal or borated tissue);
- E_{coll} is the energy deriving from the collision inside the biological tissue: for example for (n,α) reactions with ^{10}B the mean high LET energy released per event is 2.34 MeV

$$\frac{[^7Li(0.84MeV) + \alpha(1.47MeV)] \cdot 94\% + [^7Li(1.01MeV) + \alpha(1.78MeV)] \cdot 6\%}{100\%} \tag{5.11}$$

  assumed to be deposited locally;
- $\phi(E)$ is the neutron fluence in the examined cell in [cm^{-2} MeV^{-1}];
- ρ_a is the biological tissue density in [atoms $barn^{-1}$ cm^{-1}]. The unit choice derives from the eq. (5.10) where the cross section σ_a is espressed in [barn] and the neutron fluence $\phi(E)$ in [cm^{-2} MeV^{-1}];

- σ_a is the microscopic cross section expressed in [barn]

The value of the constant $K_{n,B}$ is connected to several parameters: kerma factors, source intensity, RBE and CBE factors, unit of integral $D_{n,B}$ in [Gy-eq min^{-1}].
The following value for $K_{n,B}$ is used:

$$K_{n,B} = NS \cdot 60 \cdot K_2 \cdot E_{eff} \tag{5.12}$$

where:

- NS is the neutron source intensity in [s^{-1}];
- 60 represents [s min $^{-1}$];
- K_2 is a proportional constant equal to $1.602 \cdot 10^{-10}$ in order to change the energy and the mass units from [MeV g^{-1}] to [J Kg^{-1} = Gy];
- E_{eff} is the biological effectiveness (numerically expressed by RBE and CBE factors) in order to obtain the dose units [Gy-eq].

The dose due to ^{10}B(n, α)^{7}Li in the tumour tissue can be derived from the boron dose in healthy tissue multiplied by the concentration ratio between tumour and healthy tissues and then by combining the physical dose with the proper CBE factor.
The biological dose to healthy tissue due to gamma radiation is calculated by an expression such as:

$$D_\gamma = \frac{1}{M} K_\gamma \int dV \int dE \cdot E_{coll} \cdot \phi(E) \cdot \rho_a \cdot \sigma_a \tag{5.13}$$

where:

- M is the cell mass in [g];
- K_γ is a constant depending on the particle type;
- V, E_{coll}, $\phi(E)$, ρ_a and σ_a have the same meaning of the equation (5.10).

In order to obtain D_γ in [Gy-eq min^{-1}], the value of K_γ is fixed at:

$$K_\gamma = NS \cdot 60 \cdot K_2 \cdot E_{eff} \tag{5.14}$$

where E_{eff} is 1 for gamma rays and the other terms are the same as those that appear in equation (5.12) for $K_{n,B}$.

The MCNP code allows to calculate the integrals in the eq. (5.10) and (5.13) in a separate way for the four dose components.
The boron dose cannot be determined or evaluated directly, therefore this component is evaluated assuming a homogeneous distribution of the boron in the tissue of interest. The ^{10}B concentration in tissues is included in the Monte Carlo transport simulations.
For these reasons, only Monte Carlo-based software programs have been applied in clinical BNCT.

5.3 Considerations

The success of BNCT is dependent upon the selective delivery of sufficient amounts of ^{10}B to the tumour, with only small amounts localized in the surrounding normal tissues [49]. Thus, normal tissues, if they have not taken up sufficient amounts of boron-10, can be spared from the nuclear capture and fission reactions.
In theory BNCT is a highly selective type of radiation therapy that can target tumour cells without causing radiation damage to the adjacent normal cells and tissues. Doses up to 60-70 Gy can be delivered to the tumor cells in one or two applications compared to 6-7 weeks for conventional fractionated external beam photon irradiation.

Chapter 6

Radiosensitizers in the treatment of cancer

Radiation therapy has been the mainstay of nonsurgical treatment of cancer for over a century, while the classic chemotherapy drugs such as cisplatin and 5-fluorouracil (5-FU) have been in clinical use for almost 50 years. The combination of these modalities is a more recent event that continue to evolve, and it has become the standard of care for most patients with solid tumours based on improvements in loco-regional disease control and survival. This effect is known as *radiosensitization*.

An interpretation of radiosensitization stressed the importance of a differential effect between tumours and normal tissues, and suggested that only two types of sensitizers found practical use in clinical radiotherapy [14]:

1. the pyrimidines, based on the premise that tumour cells proliferate more rapidly and, therefore, incorporate more pyrimidine analogues than the surrounding normal tissues;

2. hypoxic cell sensitizer, which increase the radiosensitivity of cells lacking in molecular oxygen, based on the premise that hypoxic cells occur only in tumours and not in normal tissue.

Although both of these premises were sound, these two classes of drugs turned out to be less than effective in the clinic for reasons that are probably connected with pharmacokinetics and drug delivery issues. In fact, the hypoxic cell sensitizers (e.g., misonidazole), and thymidine analogues (e.g., bromodeoxyuridine) are examples of "true" radiosensitizers in that they have no inherent cytotoxicity[1]. However, the most commonly used radiosensitizers (cisplatin and 5-FU) do have inherent cytotoxic activity and can increase damage to normal tissues, with a "true" benefit achieved only if the increase in antitumor effect is larger than the normal tissue damage. The result of the combined treatment is at least an additive effect of the two modalities and at best a synergism effect.

[1] *Cytotoxicity*: It is the quality of being toxic to cells. A treatment of cancer often relies on the ability of cytotoxic agents to kill or damage cells which are reproducing; this preferentially targets rapidly dividing cancer cells.

6.1 Combining two agents together: additivity and synergy

A common definition of synergy is that the effect of two agents given together is more effective than would be predicted based on their individual activity. Thus, if agent 1 alone causes the surviving fraction to be reduced to 0.5, and agent 2 used alone also reduces survival to 0.5, then the effect of agents 1 and 2 combined will be to reduce survival to 0.25 if the effect is additive and to less than 0.25 if the effect is synergistic. This will only be correct if the survival curves generated by agents 1 and 2, when used separately, are both exponential.
If the response curves are shouldered, more than one scenario is possible. If the agents are used, both of which have a survival curve with a shoulder followed by an exponential slope, then there are three possibilities (Figure 6.1):

1. if there is no overlap of damage and the shoulder representing the accumulation of sublethal damage is retained for the second agent;

2. if cells have accumulated maximum sublethal damage from agent 1, the shoulder of the survival curve is lost for the second agent;

3. if the final slope of the survival curve is altered, that is, becomes steeper, for the combined effect of two drugs.

The relationships described imply that there is a range over which two agents can produce additive effects.

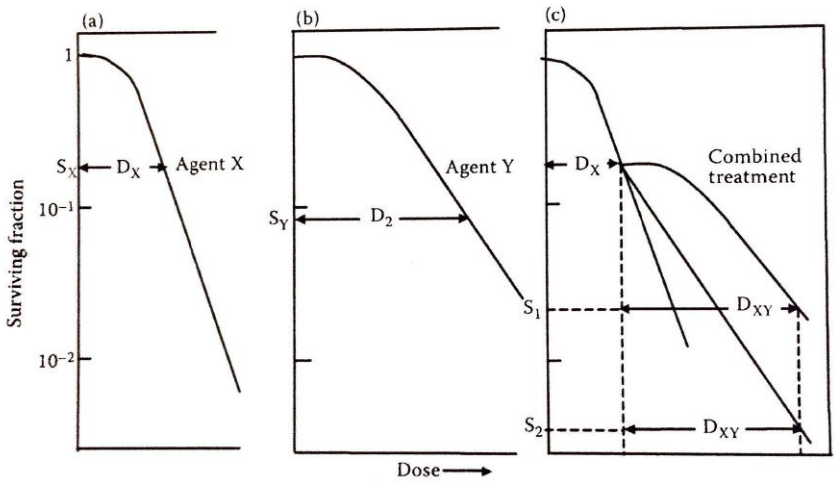

FIGURE 6.1: The effect of combining two cytotoxic agents together [65]. Cell survival is indicated following treatment with agent X or agent Y, each of which has a survival curve with a shoulder followed by an exponential slope with increasing dose (a and b). Survival (S_{XY}) after combined use of dose D_X of X and dose D_Y of Y will be equal to $S_1 = (S_X \times S_Y)$ if there is no overlap of damage and the shoulder is retained for the second agent (c). Survival after combined treatment S_{XY} will be equal to S_2 if cells have accumulated maximum sublethal damage from the first agent X and the shoulder of the curve is lost for the second agent Y.

6.2 Drugs and radiation

Mechanisms of interaction between drugs and radiation can be evaluated at the cellular level on the basis of radiation survival curves prepared with or without the drug.

Drugs can influence the survival curve in three ways (see Figure 6.2)

1. the curve may be displaced downward by the amount of cell kill produced by the drug alone;
2. the shoulder on the survival curve may be lost, suggesting that the drug is in some way preventing the repair of sublethal damage;
3. the slope on the survival curve may be altered, indicating sensitization or protection by the drug.

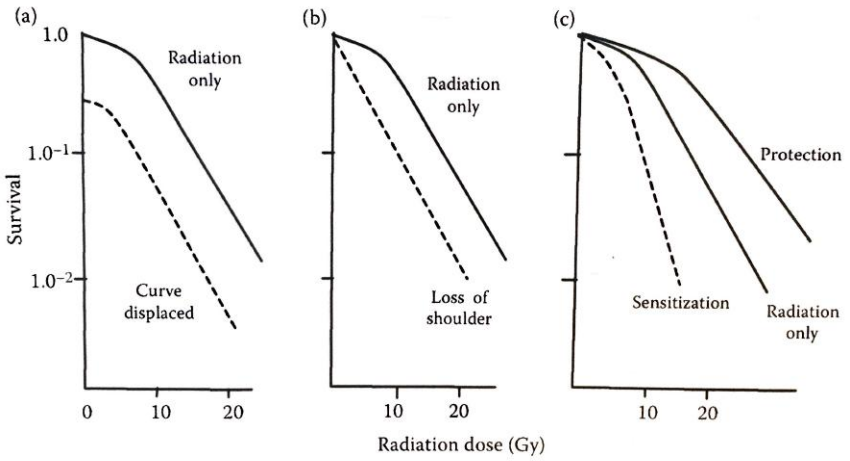

FIGURE 6.2: Possibile outcomes of drug treatment on the relationship between the radiation dose and cell survival [65]. (a) Displacement of curve; (b) loss of shoulder, indicating the effects of drug on the repair of sublethal damage; and (c) change in the slope of the curve indicating sensitization or protection.

Most drug influence radiation response according to the first two modes, a type of response corresponding to the limits of additivity described in par. 6.1. The third type of response defines drugs that are radiosensitizers or protectors.

Table 6.1 lists the important interactions between radiation and chemotherapy, which occur at the cellular and tumor cell population level .

TABLE 6.1: Mechanisms of Chemotherapy and Radiotherapy interaction

Process Affected (Mode of radiosensitization)	**Mechanism**	**Example**
Increase DNA damage (cytotoxic enhancement)	Drug incorporated into DNA/RNA	Cisplatin, 5-FU, cetuximab, incorporation increases damage susceptibility
Inhibit DNA repair (cytotoxic enhancement)	Prevent repair of radiation damage	Halogenated pyrimidines (5-FU) nucleoside analogues (gemcitabine, fludarabine), cisplatin
Cell cycle slowing/arrest (cytotoxic enhancement)	Radiation and most chemotherapy target cycling (proliferating) cells. Accumulation of cells in radiosensitive G_2/M. Elimination of radioresistant S-phase cells	Texanes (microtubule stabilization) nucleoside analogues, hydroxyurea

Increase of DNA damage. The majority of chemotherapeutic drugs target DNA and directly produce damage, which manifests as DNA breaks. For example, the integration of cisplatin into DNA or RNA close to a radiation-induced SSB can act synergistically to make the defect significantly more difficult to repair.

Inhibition of DNA repair. Chemotherapy agents have been shown to inhibit the repair of radiation. For example, Fludarabine is a nucleoside analogue which is incorporated into DNA and blocks DNA primase, DNA polymerase and DNA ligase.

Cell cycle effects. When administered concurrently, radiotherapy and chemotherapy often target different phases of the cycle and may cooperate to produce an additive effect. The radiosensitivity of a cell is dependent on the phase of the cell cycle; cells in the S phase being the most radioresistant, whereas those in the G_2-M phase are the most radiosensitive.
Because tumors are often defective in one of the cell cycle checkpoints (e.g., the G_1/S checkpoint), inhibiting the remaining checkpoints can shorten the cell cycle, leaving tumors with less repair time and resulting in greater cell kill than in normal tissues. The majority of chemotherapeutic agents are inhibitors of cell division and are thus mainly active on proliferating cells, in addition, many drugs have cell cycle phase specificity. For example, Gemcitabine, fludarabine, texanes and 5-FU inhibit various enzymes involved in DNA synthesis and repair in S-phase cells.

As a consequence of cell cycle phase-selective cytotoxicity of chemotherapeutic agents, the remaining surviving cells will be synchronized. If radiation could be delivered when these synchronized cells have reached a more radiosensitive phase of the cell cycle (e.g., G_2/mitosis), a potentiation of the radiation effect might be observed.

In Figure 6.3 is possible to appreciate the effect of radiosensitizers in radiotherapy.

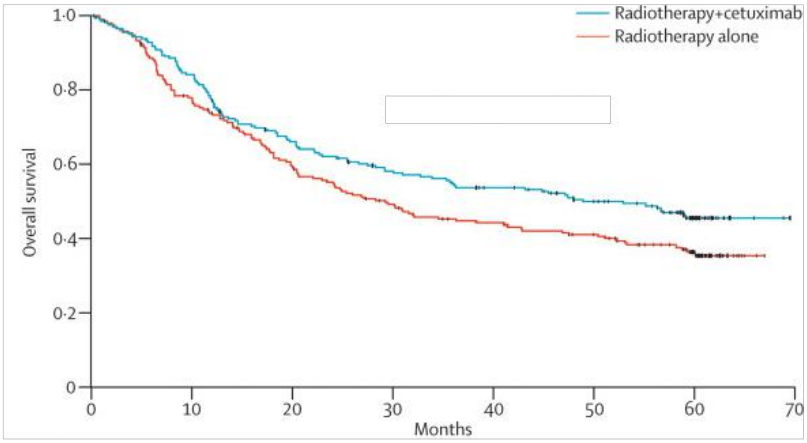

FIGURE 6.3: Radiotherapy plus Cetuximab for locoregionally advanced head and neck cancer. Overall survival by treatment: 5-year update [66]. Seven patient was treated. The red curve represents radiotherapy alone, while the blu one radiotherapy coupled with the Cetuximab radiosensitizer. The overall survival at 5-year is greater in the combined treatment case.

6.2.1 BNCT as radiosensitizer in radiotherapy

Efforts to improve radiotherapy efficacy have focused on the identification of compounds that can sensitize targeted areas to radiotherapy while limiting bystander and systematic toxicity, thereby enhancing radiotherapy within tumor cells relative to normal cell.
For this reason, considering the selective characteristics of BNCT described in the previous chapter 5, the research work aims at exploiting the boron-10 compound usually employed in BNCT applications as a localized radiosensitizing drug in radiotherapy. This radiosensitization effect could increase the treatment effectiveness.

Chapter 7

Materials: The experimental detection system

In this chapter, the experimental detection system is described, reporting both the instrumentation used to measure the photon absorbed dose and the neutron dose equivalent, and the employed anthropomorphic phantoms to detect the dose in depth in tissue.

7.1 Gafchromic EBT3 films

Radiochromic films have become an important instrument in medical applications both to verify and to measure two-dimensional dose distributions in external beam radiotherapy, radiosurgery and brachytherapy [67], [68].
The most popular radiochromic films are the Gafchromic EBT films by Ashland Advance Materials Inc. (Wayne, NJ, USA) and, at the moment, the third generation of the film - EBT3 (shown in Figure 7.1), released in late 2011, is available for the radiotherapy community [69] .

FIGURE 7.1: Gafchromic EBT3 films
by Ashland Advance Materials Inc. (Wayne, NJ, USA), 2011.

Films used in this work are the GAFCHROMIC EBT3 (batch number A10171102), with sheet dimensions of (20.3×25.4) cm^2, and they were handled according to the procedures described in the AAPM TG-55 report [70] and in the user guideline provided by the manufacturer together with the films [71].

7.1.1 Description

The EBT3 is a self-developing film, it doesn't require post-exposure processing, and it can be read with commercial flatbed RGB (Red Green Blue) color scanners.
The film is tissue equivalent and water resistant, its dose response ranges from 1 cGy to tens of Gy, and it has got a high spatial resolution (about 25 μm).

The Gafchromic EBT3 dosimetry film is made up of a single active layer, nominally of 27 μm thick, placed between two transparent polyester substrates of 120 μm thick each, as represented in Figure 7.2. This symmetric structure allows to no longer keep track which side is which, eliminating the film face-dependence during scanning.

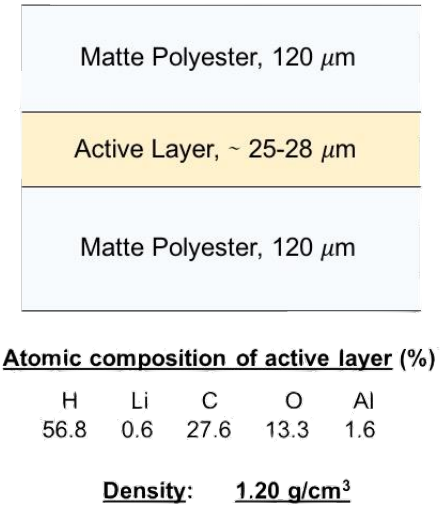

FIGURE 7.2: Gafchromic EBT3 film structure.
The film is made up of a single active layer, nominally of 27 μm thick, placed between two polyester substrates, 120 μm thick each.
The atomic mass fraction of the elements constituting the active layer and the film density are also reported.

The active layer contains the active component, stabilizer, a yellow marker dye and other additives giving to the film its low energy dependence. The yellow marker dye, used in conjunction with a RGB film scanner, decreases UV/light sensitivity and enables multi-channel dosimetry, improving thus the dosimetry results [72].
The polyester substrate, instead, is coated with silica particles. These particles maintain a gap between the film surface and the glass window in a flatbed scanner. Since the gap is nearly ten times the wavelength of visible light, formation of Newton's Ring patterns[1] is prevented in the scanned image.

[1] *Newton's rings*: it is a phenomenon in which an interference pattern is created by the reflection of light between two surface: a spherical surface and an adjacent touching flat surface. It is named for Isaac Newton, who first studied the effect in 1717.

7.1.2 Principle of operation and use

Like all other Gafchromic films, EBT3 dosimetry films can be handled in interior room light for short periods without noticeable effects. However, it is suggested that the film should not be left exposed to room light for hours, but rather should be kept in the dark when not in use [70].
When the active component in EBT3 film is exposed to radiation, it reacts to form a blue colored polymer with an absorption maxima at approximately 633 nm.
The Gafchromic EBT3 dosimetry film is recommended to be used with a 48-bit flatbed color scanner: the EPSON Expression 11000XL or 10000XL Photo scanners are the recommended models due to their large scanning area, measuring the red, green and blue color components of light transmitted by the film at a color depth of 16-bit per channel.

In this work, the exposed films were read two days after the irradiation to allow the stabilization of changes in all the color channel [73], and each film was read three times with the EPSON Expression 10000XL flatbed scanner on the same day, to ensure the identical condition of temperature and humidity, minimizing thus the scanner variability.
The readout process was made according to the manufacturer's scan guideline [71], placing the films into the center of the scan area in landscape orientation (a frame was used to fix the film in a reproducible way), keeping consistent position and orientation in each scan to avoid the lateral scan effect.
RGB-positive images were collected in 48-bit, with a spatial resolution of 72 dpi, in transmission mode with no colour correction, keeping fixed all the scanner parameters during all the film acquisitions.
The digitized images were then saved in tagged image file format (TIFF) and analyzed by means of the software *ImageJ 1.50i* [74], by splitting the film image data into red, green and blue color channels.
For each scanned image and color channel, a small region of interest (ROI) at the field centre was selected to obtain the mean pixel value V and its standard deviation σ. Knowing these values and the absorbed dose D by each film, the dose response curves per each color channel were plotted and analyzed with the software ROOT [75].

7.1.3 Calibration and sensitivity

Before to use a set of radiochromic films with an identical batch number, one film needs to be calibrated exposing it to known photon doses.
For this reason, in order to investigate the film performance and to obtain a calibration curve, several film pieces, each of (4×4) cm^2, were irradiated at different dose values, from 0.5 to 90 Gy, with the 15 MV photon beam provided by the Elekta Synergy Agility LINAC at Maggiore Hospital, Trieste (Italy).
Films were placed in a water equivalent slab phantom (RW3 PTW [76]) of $(30\times30\times12)$ cm^3 at 1.6 cm depth, in correspondence with the build-up, and irradiated perpendicularly to the radiation beam. The distance from the source to the phantom surface (SSD) was 100 cm and the field size was (30×30) cm^2 at isocenter. The RW3 phantom was centered under the LINAC gantry thanks to its laser alignment system.

The typical dose response for EBT3 film on a RGB scanner is shown in Figure 7.3, [71]. Note that the response curves slopes are different for each color channel. Each

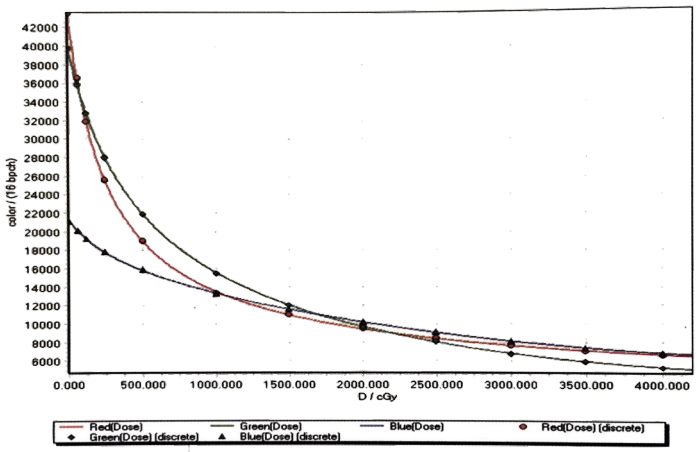

FIGURE 7.3: Typical response of Gafchromic EBT3 film in all color channels [71].

of the signals is comprised of a dose-dependent and a dose-independent portion, but the proportions are different in each color channel. For instance, the response in the blue channel has a relatively low slope because the signal has weak dose-dependent while having strong dependence on the thickness of the active layer; instead the response in the red channel has a relatively high slope because the signal is highly dose-dependent.

The recommended equation to fit the calibration curve is:

$$d_x(D) = \frac{a+b}{D-c} \tag{7.1}$$

where $d_x(D)$ is the optical density[2] of the film in the scanner channel x at dose D, and a, b, c are the equation parameters to be fitted.

However, in this work, the suggested function to fit the dose response curve has been empirically modified both to avoid the problem of an impossible ratio when D is equal to c in equation 7.1 and to provide more precise dose measurements.
The modified calibration function is represented by:

$$V(D) = \frac{W_0 + W_1(D/c)}{1 + (D/c)} \tag{7.2}$$

where $V(D)$ is the pixel value as a function of the absorbed dose D, and W_0, W_1, c are the equation parameters to be fitted that depend on the considered color channel. Moreover, W_0 is the pixel value corresponding to D tending to zero (linked, thus, to the unirradiated film); W_1 is the pixel value corresponding to D tending to infinite (linked to the maximum film dimming); while the parameter c represents the dose at which the pixel value is half way between W_0 and W_1, $[(W_0 + W_1)/2]$.

The rational formula 7.2 can be inverted for each of the three RGB colors to provide three absorbed dose values D_x starting from the film dimming V, with their associated propagated uncertainty. Then, by weighting the three RGB D_x values, a

[2] *Optical density*: it describes the propagation of a wave through a material, and it is calculated as the logarithmic ratio of the radiation incident on the material to the radiation transmitted by the medium.

final more precise dose value of an unknown film can be obtained.
Detailed information about the calibration function and the employed procedure can be found in the recently submitted paper attached in Appendix B.
The described procedures provide dose measurement uncertainty well below 2% with a precision of about 2.5%, respecting the precision level of 2-4% to be achieved in film dosimetry [77], [78]).

Notice that other works, such as the recent one by Ref.[79], propose alternative calibration functions, but often using more complicated expressions not simply to be handled, inverted and/or suitable for a large dose range like the one here described.

7.2 Superheated Drop (Bubble) detectors

First described by Apfel in 1979 [80], the bubble or superheated drop detectors are becoming more and more attractive for practical applications in neutron dosimetry.
The most popular bubble detectors are those commercially available from Bubble Technology Industries (BTI), Chalk River, Canada [81], showed in Figure 7.4.

FIGURE 7.4: Bubble dosimeters representation.
Neutron integral passive bubble detectors from
Bubble Technology Industries (BTI).

In this work two types of their detectors were used, the BD- PND and the BDT. The BD-PND type has an energy threshold at approx. 100 keV (fast neutrons) and it is supposed to give a good estimate of dose equivalent above this threshold. While the BDT was introduced to monitor thermal neutrons, neutrons with energy up to 0.4 eV.
Bubble dosimeters are unique in their high sensitivity to neutrons (up to a few bubbles per μSv), in their direct reading capability and in their insensitivity to γ-radiation, with an isotropic angular distribution: they are thus suitable to be employed in mixed radiation fields as in radiotherapy.
Research in this field [82], [42] suggest that the bubble detector is the only type of personal neutron dosimeter with adeguate sensitivity (i.e., low detection threshold) to meet the implications of ICRP Publication 103 [22] (the revised ICRP Publication 60 [27]) recommendations for neutron dosimetry.

7.2.1 Description

A bubble dosimeter consists of a transparent plastic vial of 8 cm^3 containing a clear, elastic hydropolymer medium throughout which 10^4-10^5 tiny droplets approximately 20 μm in diameter of a superheated liquid (CCl_2F_2) have been dispersed.
The polymer in the vial is kept under pressure to prevent the droplets from growing under normal conditions (i.e., before the detectors are prepared for exposure to neutrons). The pressure on the elastic polymer is controlled by a cap assembly on top of the vial.
The bubble dosimeter from BTI has built-in temperature compensation, which keeps response sensitivity within $\pm$20% between 20°C and 37°C (see Figure 1 in Appendix A, provided by BTI).
The number of the bubbles obtained from the dosimeter is proportional to the neutron dose over a wide neutron range (see Figure 3 in Appendix A, provided by BTI). The proportionality constant (i.e., sensitivity) is indicated on the label of every bubble dosimeter.
Each dosimeter is shipped in an airtight aluminum storage tube and with the polymer medium containing the superheated droplets pressurized (i.e., with the cap screwed onto the top of the dosimeter).

7.2.2 Principle of operation and use

By unscrewing the cap assembly of the bubble dosimeter, the pressure on the polymer is released, and the liquid droplets become superheated. When the dosimeter is exposed to a neutron flux, neutrons strike the polymer, and the superheated droplets vaporize due to the high linear energy transfer (LET) recoils from neutron interactions. Small visible bubbles are thus produced instantly in the sensitive medium. A representation of the process is shown in Figure 7.5.

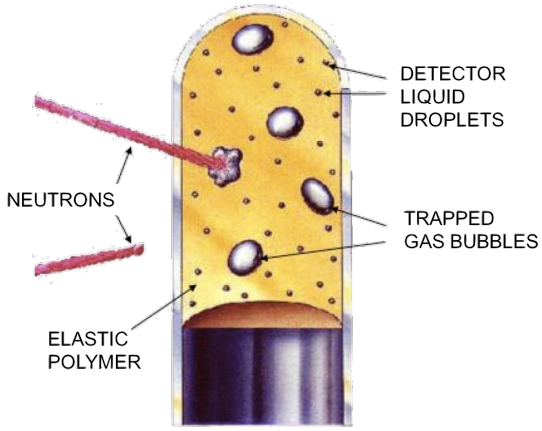

FIGURE 7.5: How a bubble detector works.
Neutrons interaction with the clear elastic polymer constituting the dosimeter, in which tiny droplets of a superheated liquid (CCl_2F_2) have been dispersed. Neutrons strike the polymer and the superheated droplets vaporize due to the recoils from neutron interactions, making the bubbles visible.

The number of the produced bubbles is proportional to the neutron dose equivalent as shown in Figures A.2 and A.3 in Appendix A (provided by the manufacturer).

The bubbles are fixed in the elastic medium and can be subsequently counted visually or by an automatic image reader. The dose is determined by multiplying the number of bubbles by the dosimeter's sensitivity (i.e., the proportionality constant between the number of the bubbles and delivered dose).
Studies demonstrate that the number of observed bubbles increases with time after the end of exposure [83]. The increase is approximately (2-4)% in the first 24 hours, then climbs to (4-6)% in the next 24 hours (48 hours after the end of exposure), reaches 10% in the next 24 hours (72 hours after the end of exposure), and ranges between (10-20)% in the next 72 hours (144 hours after the end of exposure). This small increase in the number of the bubbles after the end of exposure may be explained by assuming that some bubbles are too small to be counted immediately after the end of the exposure but then may gradually increase in size as evaporation continues due to the fact that the pressure of the gel is insufficient to fully immobilize them. Thus, the bubbles eventually reach sufficient size to be counted some time after exposure. This effect is relatively small and may be considered to be within the uncertainties associated with neutron dose determination.
However, the manufacturer recommends keeping the dosimeters under pressure when not in use (i.e., reading the exposed dosimeters as soon as feasible and repressurizing them as soon as possible): for this reason, in this works the produced bubbles were read within 1-2 hours after the measurement.

To reuse the dosimeter, the bubbles must first be recompressed into droplets by screwing the cap assembly back on the dosimeter. The detector is activated again by unscrewing the cap assembly on the top of the dosimeter. The bubble dosimeter can be reused several hundred times.

7.2.3 Calibration and sensitivity

The bubble dosimeters are calibrated by the manufacturer with an Am-Be source having a fluence-weighted average energy equal to 4.15 MeV and a source strength of 1.13×10^7 n/s. Dosimeters are calibrated by BTI without the use of a phantom and with a combination of time and distance from the source that produces approximately 100-150 bubbles. The source and the dosimeters are held upright and parallel to each other in a styrofoam jig. The conversion factor used for the Am-Be source is $3.70 \times$ mrem/(n·cm^{-2}), as calculated from dose equivalent defined in ICRP Report 107 [84] (the revised ICRP Report 38 [85]).

The dosimeters are exposed to the neutron source to determine their detection sensitivities. The detection sensitivity is then indicated on the label of every bubble dosimeter and a calibration certificate is given together with each detector.
As stated by the BTI manufactures and shown in several studies, the type of the neutron source used in calibration has only a small effect on the sensitivity value [86], [87]; in particular, in this work differences between detectors calibration and the neutron spectrum provided by the e-LINAC are within the 8%.

After sensitivity determination, the necessary temperature compensation components are incorporated into the dosimeters, which are then calibrated five times using the Am-Be source: one calibration each at 20°C, 24°C, 28°C, 35°C, and 37°C. A bubble dosimeter's indicated sensitivity is the average response over the temperature range 20-37°C. The Figure A.1 in Appendix A (provided by BTI) shows the temperature response of the dosimeters; while Figures A.2 and A.3 (provided by BTI)

indicate that the dosimeter's linearity with dose is excellent with and without repressurization of the dosimeters between exposures. The BD-PND bubble dosimeters provide a good estimate of the dose equivalent for neutrons with energies greater than 100 keV, as shown in Figure A.4 in Appendix A (courtesy of BTI); while the BDTs for energies up to 0.4 eV.
However, performing some calibrations in the fast secondary neutron flux provided by the medical LINAC, it was found that about one-tenth of the fast neutron dose equivalent contribute to the measured value in thermal dosimeters [47] (see Chapter 9, par. 9.2). This value has been so taken into account and excluded in thermal neutron measurements.

7.2.4 Longevity of bubble dosimeters

The end of a bubble dosimeter's useful life occurs when the bubbles can no longer be compressed back into droplets, when the elastic polymer starts leaking, or when, for any other reason, the bubble dosimeter does not properly record the neutron dose.
BTI guarantees optimum dosimeter performance for 3 months after receipt, having a shelf life of at least 6 months (assuming no exposure to neutrons and no depressurization). However, several studies indicate that the useful life span of the bubble dosimeters is longer than the manufacturer's 3-month warranty. For example, in the Vanhavere study [88], dosimeters were irradiated over a 2-year period before reaching the end of their useful life. Despite this, the dosimeters employed in this work were not expired and a calibration check was periodically performed exposing them to a known neutron field.

7.3 The anthropomorphic phantoms

Anthropomorphic phantoms are employed in radiotherapy in order to evaluate the dose absorbed by the body: their task is to reproduce, in the better possible way, the geometry, the sizes and the composition of the human body.

7.3.1 The Trieste anthropomorphic phantom

The Trieste anthropomorphic phantom was specifically developed to be suitable both for neutron and photon dosimetry. It was designed and built by INFN (National Institute of Nuclear Physics) in Trieste following the International Commission on Radiological Protection indications for neutron dosimetric phantoms (ICRP 103) [22], both about organ positions and tissue substitutes (ICRU 44) [89].

A new phantom was developed because standard phantoms usually employed in radiotherapy (like RANDO [90]) do not meet all the work needs: to provide suitably large holes to locate bubble dosimeters and to be more tissue equivalent also for neutrons.
To build a phantom for neutron dosimetry, it's necessary to consider both the elemental mass fraction of H, C, N and O (which are the main elements involved in the absorption and scattering reactions) and the neutron energy range involved: the fine details like surface curvature or squared edges of the phantom geometry are not so relevant for neutrons. The neutron RBE becomes important at energies higher than 10 keV and, in this range, the contribution to the absorbed dose comes from the main elastic scattering on Hydrogen nuclei (up to 97% [89]), while both the scattering with C, N, O and inelastic scattering and nuclear reactions give a contribution

of a few percent: for these reasons the phantom was simply made up of polyethylene. In fact looking at the mean human upper part body composition, Hydrogen is present for 0.10 mass fraction and polyethylene $[(C_2H_4)_n]$, 0.14 Hydrogen mass fraction, is suitable as material for neutron dosimetry.

The anthropomorphic phantom, represented in Figure 7.6, is thus made entirely in polyethylene and it approximates dimensions, weight, density and hydrogen content of an average man [91], as shown in Table 7.1. Moreover, in Figure 7.7 it's possible to see how the body proportions known in literature have been exploited to build the phantom. In fact, it is composed by several modular polyethylene blocks, listed in Table 7.2 and shown in Figure 7.8, reporting also the external dimensions. The modular characteristic lets both to place the phantom in the sitting position, making it suitable for other different dosimetric purposes, and to be easily transported.

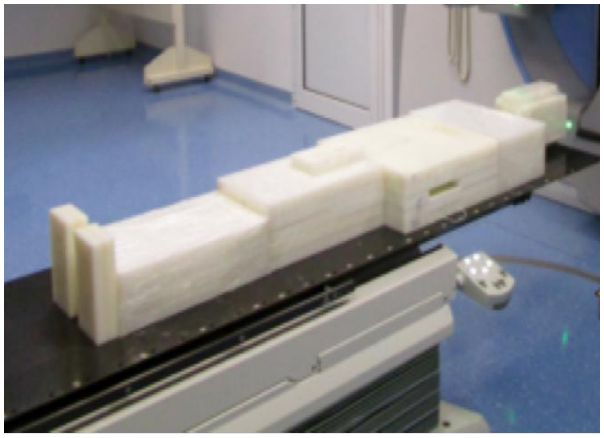

FIGURE 7.6: A representation of the Trieste anthropomorphic phantom.

TABLE 7.1: Comparison between the human body and the Trieste anthropomorphic phantom.

	Height [cm]	**Weight** [kg]	**Density** [g/cm^3]	**Hydrogen content** [mass fraction %]
Human body	1.70	73.6	1	0.10
Phantom	1.73	71	0.96	0.14

Inside the phantom several holes, suitable to allocate bubble dosimeters, have been made in correspondence with critical organs in order to detect the neutron dose equivalent in depth in tissue. In details, the chest and abdomen area consist of five polyethylene slabs, in which three slabs present a drawer with arrays (shown in Figure 7.9) in which bubble dosimeters can be placed. In this way it's possible to arrange each dosimeter in the correct organ position and depth, following the ICRP 103 [22] (new ICRP 60 release) recommendations. Moreover, two holes have been made in the phantom head in order to locate detectors also in correspondence of the brain position.

Two dosimeters (one for fast neutrons and one for thermal neutrons) were placed

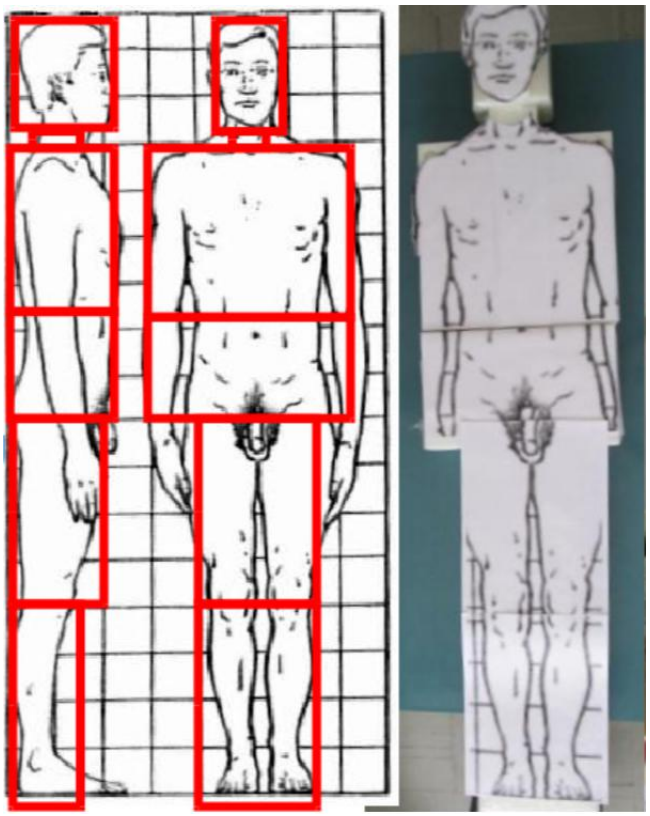

FIGURE 7.7: Study of the body proportions useful to build the Trieste phantom.

in the considered organ positions, and holes with no dosimeters inside are filled with polyethylene cylinders having the same shape of the dosimeter, so no vacuum areas are present.
The critical organs taken into account for the Trieste phantom are those represented in Figure 7.10 and reported in Table 7.3.

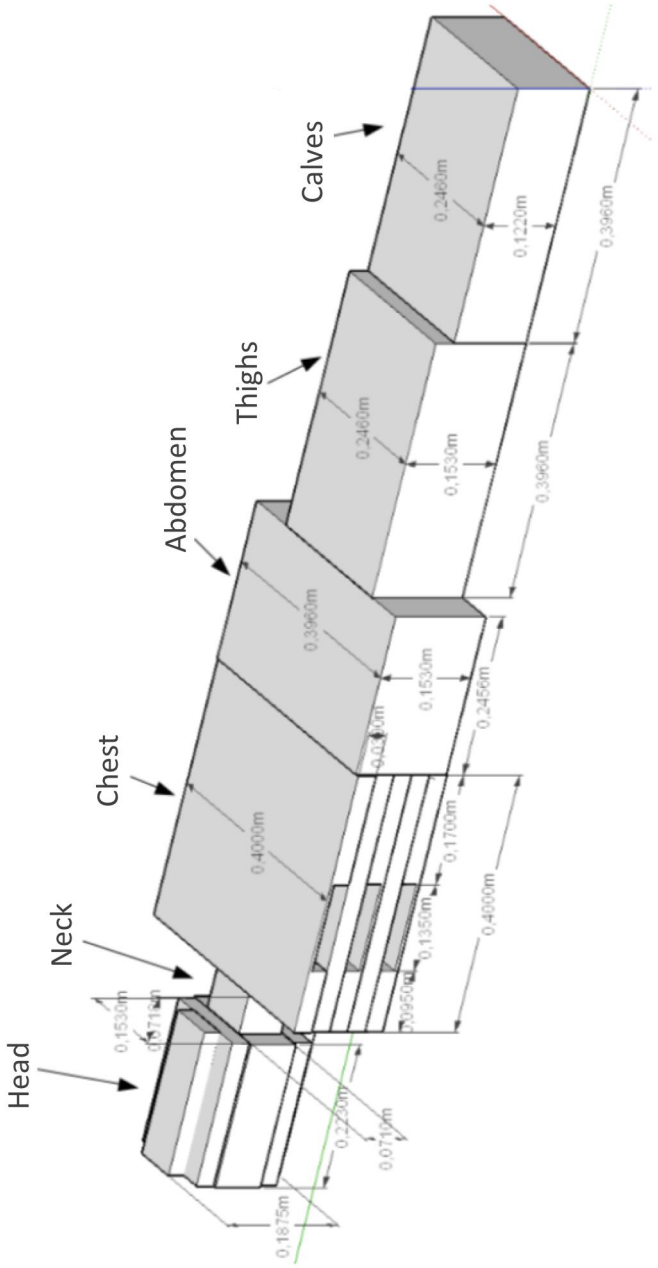

FIGURE 7.8: 3-D representation of the Trieste anthropomorphic phantom with its external dimensions. The design was made by means of the open source software *SketchUp* [92], a computer graphics application for 3D modeling.

TABLE 7.2: The Trieste anthropomorphic phantom, external dimensions.

	Height [cm ± 0.1 cm]	**Width** [cm ± 0.1 cm]	**Depth** [cm ± 0.1 cm]
Head	22.0	15.0	19.0
Neck	7.0	9.0	7.0
Chest	40.0	40.0	15.0
Abdomen	25.0	40.0	15.0
Thighs	40.0	25.0	15,0
Calves	40.0	25.0	12.0
Feet (2×)	20.0	10.0	5.0

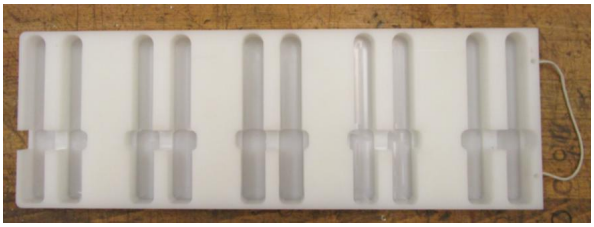

FIGURE 7.9: Representation of the drawer with five couples of arrays suitable to host bubble detectors for the chest area of the Trieste phantom.

TABLE 7.3: Considered critical organ positions in the Trieste anthropomorphic phantom.

Position	**Organs**	**x** [cm ± 0.1 cm]	**y** [cm ± 0.1 cm]	**z** [cm ± 0.1 cm]	**Drawer**
	Brain	0.0	84.0	10.0	
a-b	Thyroid	0.0	60.0	5.0	1
d	Lung (right)	-10.0	45.0	10.0	2
g	Stomach	2.0	45.0	10.0	2
f	Liver	2.0	35.0	5.0	1
n	Bladder	0.0	5.0	5.0	1
i	Kidney (left)	-10.0	30.0	15.0	3
	Gonads	0.0	-5.0	2.0	

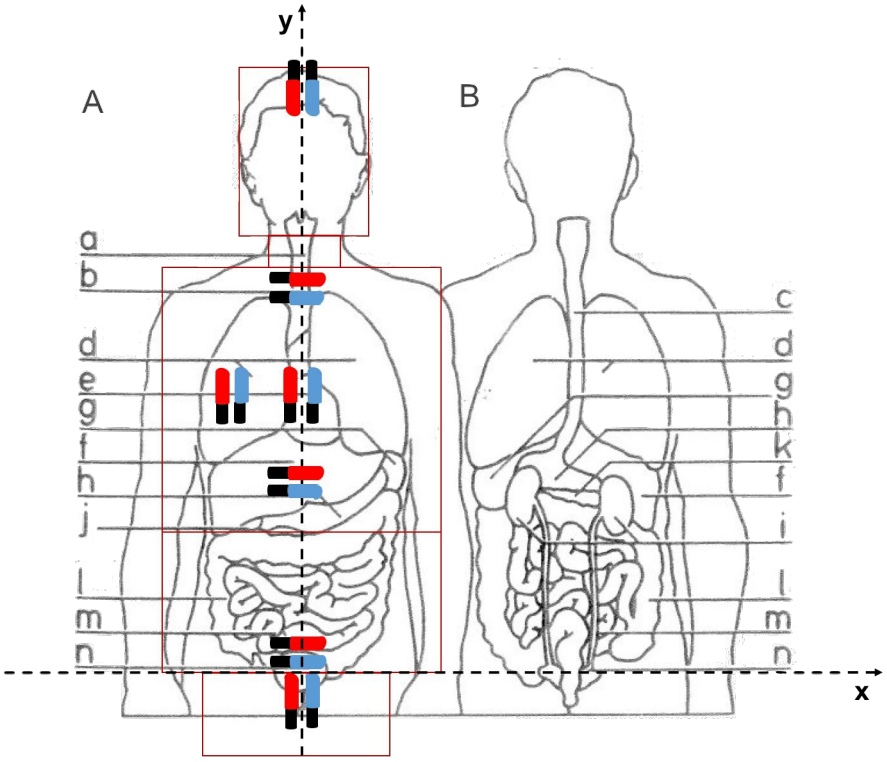

(A) Front projection.

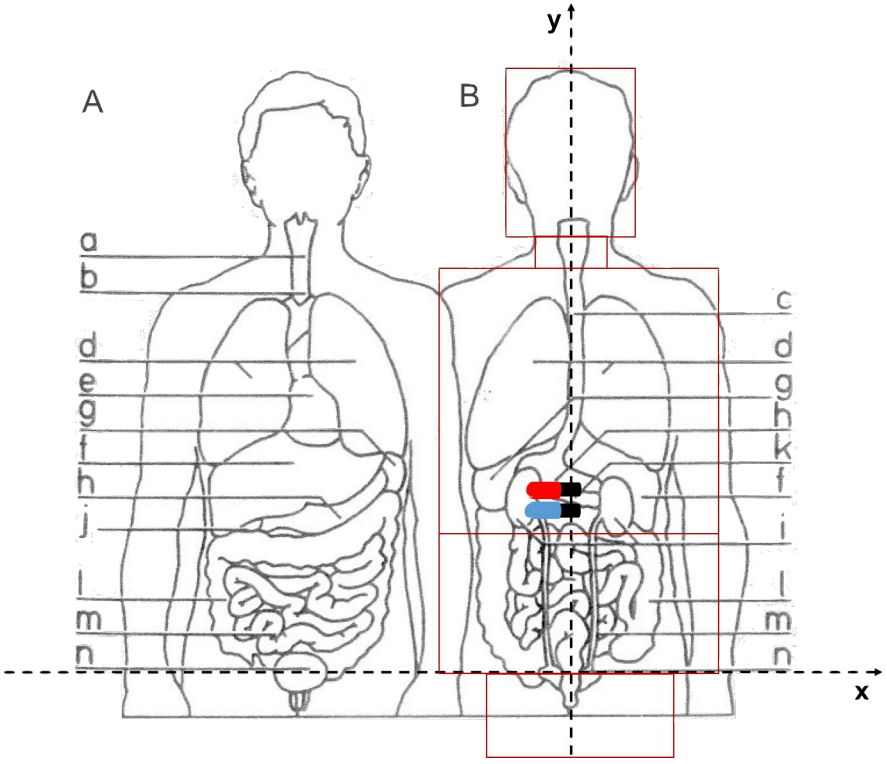

(B) Back projection.

FIGURE 7.10: The Trieste anthropomorphic phantom overlapping the front and back projection of the human body, with bubble dosimeters located in correspondence with the considered critical organs. Blue dosimeters correspond to the BD-PNDs, the red ones to the BDTs.

7.3.2 The Torino anthropomorphic phantom

Measurements carried out in Torino were performed by using an existing anthropomorphic phantom.

The Torino anthropomorphic phantom (Figure 7.11) was designed and made by INFN sec. Turin in collaboration with the Ispra JRC (Join Research Centre), Varese, Italy, several years ago [93]. It was specifically developed for neutron dosimetry in order to evaluate the neutron spectrum and the neutron dose equivalent in tissue (NCRP 38) [41].
The Torino phantom is made up by different slabs of plexiglass and polyethylene (seven plexiglass slabs of 1 cm and 2 cm thickness, and one polyethylene slab of 6 cm thickness). There are also 16 cavities in correspondence of critical organs suitable to locate the integral passive bubble dosimeters (BTI) in order to detect the neutron dose in depth. Moreover, the phantom has human bone dust inserted in correspondence of the vertebral column, taking so into account the interactions between neutrons and calcium nuclei.
The phantom was designed following the International Commission on Radiological Protection indications for neutron dosimetric phantom both about organ positions (ICRP 60) [27] and tissue substitutes (ICRU 44) [89].

The mass fraction composition of materials of the Torino phantom are reported in Table 7.4, while its external dimensions and organ positions in Table 7.5 and 7.6, respectively.

Moreover, Table 7.7 shows the comparison between the composition of the anthroporphic phantom and the reference ICRU sphere[3](ICRU 44)[89]. The hydrogen content inside both phantoms is comparable.

TABLE 7.4: Chemical composition and density of materials constituting the Torino phantom.

Materials	**Percentage mass**	**Density** [g/cm^3]
Plexiglas	8% H, 32% O, 60% C	1.190
Polietilene	14.4% H, 85.6% C	0.920
Polvero di osso	0.2% H, 41.4% O, 18.5% P, 39.9% Ca	1.930

[3] *ICRU sphere*: standard phantom for the definition of operational quantities for dose equivalent. It is a 30 cm diameter sphere, with a density of 1 g/cm^3. The chemical composition, in percentage mass, is: H (10.1%), C (11.1%), O (76.2%), N (2.6%).

FIGURE 7.11: The Torino anthropomorphic phantom representation. Front projection. It is possible to see the holes in correspondence of critical organs with inside the BTI detectors.

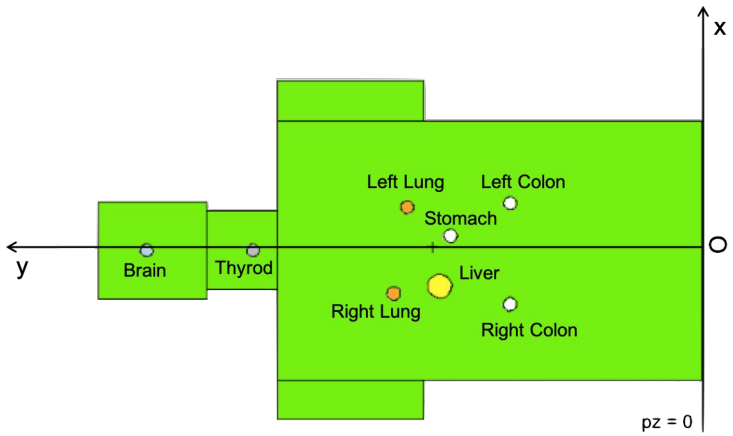

FIGURE 7.12: The reference system for determining the organ positions in the Torino anthropomorphic phantom. Organs belonging to slab No.5 are reported.

TABLE 7.5: The Torino phantom, external dimensions.

	Hight [cm ± 0.1 cm]	**Width** [cm ± 0.1 cm]	**Thickness** [cm ± 0.1 cm]
Head	15.0	13.5	19.0
Neck	10.0	11.0	13.5
Body	59.0	30.0 (chest)	20.0
		36.0 (chest + pelvis)	
		47.0 (chest + pelvis + shoulders)	

TABLE 7.6: The Torino phantom, organ positions. The coordinates were calculated by choosing the origin of the reference system along the vertical axis of the phantom, on the surface of the first slab (as shown in Figure 7.12), and the z-axis pointing downwards. The mid-point of each cavity was chosen to identify the position of the organ. The slab No.5 is made up of polyethylene, while the remaining ones of plexiglass.

Organs	**x** [cm ± 0.1 cm]	**y** [cm ± 0.1 cm]	**z** [cm ± 0.1 cm]	**slabs**
Gonads	0.0	10.0	2.0	2
Bladder	0.0	17.2	6.0	4
Liver	-5.0	36.5	6.0	4
Esophagus	0.0	39.7	6.0	4
Right Colon	-7.5	26.7	10.1	5
Left Colon	6.5	26.7	10.1	5
Stomach	2.0	35.0	10.1	5
Right Lung	-6.0	42.9	10.1	5
Left Lung	6.0	41.0	10.1	5
Thyroid	0.0	62.5	10.1	5
Brain	0.0	77.3	10.1	5
Spleen	9.5	26.0	14.3	6
Left Kidney	4.0	27.8	16.0	7
Right Kidney	-5.5	29.0	16.0	7
Bottom Column	0.0	28.8	16.0	7
Half-high Column	0.0	44.0	16.0	7

TABLE 7.7: Tissue substitutes in percentage mass. Comparison between tissues substitutes of the Torino phantom and the tissue of the reference ICRU sphere.

	Torino Phantom [w%]	**ICRU Sphere** [w%]
H	10.2	10.1
C	67.9	11.1
O	18.7	72.2
C + O	86.6	87.7
N		2.6
Bone dust (H, O, P, Ca)	3.2	
Density [g/cm^3]	1.056	1

Chapter 8

Simulation methods: the Monte Carlo codes

The way to analyse in detail complex probabilistic processes, such as the production and transport of photon, neutrons and other particles, is the Monte Carlo approach. The name is a reference to the Monte Carlo Casino in Monaco: the use of randomness and the repetitive nature of the process are analogous to the activities conducted at a casino.
Numerous software packages for Monte Carlo simulation of nuclear processes have been developed: the main ones dealing also with no-charged particles interactions and transport are Fluka, MCNP and GEANT4 [94], [64], [95].
Fluka is a fully integrated particle physics Monte Carlo simulation package born in CERN, based on Fortran77 programming. It covers an extended range of applications, from high energy nuclear physics to medical physics and radioprotection. MCNP, which the acronymous stands for Monte Carlo N- Particles, was instead developed by Los Alamos National Laboratories. It finds application in several fields, such as radiation protection and dosimetry, radiation shielding, medical physics, nuclear criticality safety, detector design, fission and fusion reactor design, etc. The last mentioned code is GEANT4, developed by CERN starting from 1998 as the successor of the GEANT series of software toolkits, and it is based on C++ object-oriented programming. It is mainly employed for high energy physics but has recently spread out in dealing with neutron problems at low energies as well as in medical physics.

The code chosen for the simulation in this work is MCNP release 4B, a quite old code but available at University. Its main features useful for the application are: the possibility to follow radiation transport of neutrons, photons and electrons using cross sections tables from evaluated data libraries for almost all the isotopes on a wide energy range; the presence of specific libraries for the handling of thermal neutrons interactions; the availability of variance reduction techniques, the treatment of photo-nuclear (γ,n) reactions with specific cross section libraries as well as the possibility to calculate the dose in BNCT, an important feature for the thesis work purpose.
Moreover, in the last part of the research work simulations by using the GEANT4 software were performed, with the intent to test the toolkit performance in simulating the neutron photoproduction in medical LINACs.

8.1 Monte Carlo simulations: the MCNP4B code

The MCNP4B release allows treating the neutron, photon and electron transport through 3-dimensional geometries. The particle is followed from the source until it stops for collisions or until it goes out from the geometry of interest. The interaction of the particle with matter is based on stochastic processes. Each probabilistic event is simulated in sequence and, only later, the individual probability distributions which regulate these events are sampled: this gives a precise description of the phenomenon.

The data necessary for the process description, such as cross sections and threshold energies, are located in suitable folders, called libraries.

The probability of neutron emitted by the source to make a collision in a range l and $l + dl$ is

$$p(l)dl = e^{-\sum_t l} \cdot \sum_t dl \tag{8.1}$$

where $\sum_t$ is the macroscopic cross section of the absorber, and it is considered as the probability for unit of path length to collision occurs.

Fixed a random number between 0 and 1 such that:

$$\xi = \int_0^1 e^{-\sum_t} \cdot \sum_t ds = 1 - e^{-\sum_t l} \tag{8.2}$$

the range l is:

$$l = -\frac{1}{\sum_t} ln(1 - \xi) \tag{8.3}$$

Since $1 - \xi$ has the same distribution of ξ, it can be replaced, obtaining the expression of the crossed distance by the neutron before a collision:

$$l = -\frac{1}{\sum_t} ln(\xi) \tag{8.4}$$

Once the collision has occurred and the target nucleus has been identified, the neutron may undergo an elastic scattering, an inelastic scattering, or a capture process.

Regarding photons, the procedure is based on two different models: the first one, used with highly energetic photons, considers the photoelectric effect, Compton scattering and pair production. Thus, the total cross section will be:

$$\sigma_t = \sigma_{ph} + \sigma_c + \sigma_{pp} \tag{8.5}$$

While, the procedure used dealing with low energy photons, or with high-Z material, considers the coherent scattering, fluorescence and capture processes. This model allows to describe interactions of photons with energies lower than the photoelectric threshold one.

The high number of small interactions which characterized the transport of electron and charged particles do not allow the Monte Carlo code to a full knowledge of the entire path of a particle, because this requires too many resources in terms of calculation speed. For this reason, suitable procedures have been included in the code in

order to treat charged particles transport, exploiting the main cross sections and the statistical dependence of the transport. It is so possible to provide an estimation of the quantity probability distributions, such as the energy loss and angular deflection.

To compile an input file is required the definition of:

1. the three-dimensional geometries, dividing the space into cells bounded by surfaces of the first and second order as a plane, sphere or cylinder;
2. the density and chemical composition of materials that make up the cells;
3. the source, by specifying the size, shape and energy spectrum;
4. the physical quantities that are to be estimated (such as particle flux, mean energy deposed, absorbed dose);
5. the variance reduction techniques in order to speed up the calculation time, such as energy cuts or by increasing the importance of some cells (detailed in Appendix C).

8.1.1 The MCNP4B-GN code

A routine implemented in the MCNP4B code, the MCNP4B-GN code (NEA 1733/01), especially developed by INFN (National Institute of Nuclear Physics) of Turin, for (γ, n) reaction was used [96].
MCNP4B-GN is used both to simulate the production of giant dipole resonance photoneutrons in thick layers of high-Z elements, treating so the (γ,n) production and transport in medical accelerator heads, and to study the undesired neutron dose to patients, employing a single code for both the electromagnetic and the neutron transport.
In the simulation code, (γ, n) and (γ, 2n) channels are treated and both evaporation and direct models of neutron emission from the nucleus are considered.

Since photonuclear cross-sections are more than 2 orders of magnitude lower than the main atomic processes (Photoelectric, Compton and Pair production), as Figure 4.2 shows, suitable and effective variance reduction techniques were applied.

Evaporation model

According to the evaporation model, a photon going deep into the nucleus, gives rise to a highly excited nucleus. This energy can be considered as the "heat" produced by the collision of the photon with the nucleus: such "heat" causes the neutron evaporation. Called E the energy corresponding to the excited level of the nucleus, the maximum kinetic energy of the emitted neutron is equal to $E - S_n$, where S_n is the neutron separation energy from the nucleus.
If the neutron leaves the residual nucleus (Z, A-1) in an excited level E_r, the corresponding energy to the emitted particle will be:

$$E_n = E - S_n - E_r \tag{8.6}$$

The energy linked to each level E_r of the residual nucleus will correspond to the neutron energy E_n until the following relation is valid: $E_r < E_M$, where E_M is the maximum energy value of the emitted particle, that is when the nucleus stays in its fundamental state.

The energy distribution of the particles emitted by the nucleus consists of a set of peaks. These peaks correspond to the spectrum of the levels of the nucleus (Z, A-1); the higher energies correspond to the lower excitation states. If the incident particle energy reaches an enough high value, a greater number of levels of the nucleus can be excited. Therefore, there will be a continuous energetic distribution of emitted particles because the E_r energies are very close to each other.
Statistical mechanics provides an explanation of the physical behavior of strongly excited nuclei. The emission of a neutron from the excited nucleus can be compared to the evaporation of a molecule from a heated liquid: the thermodynamic concepts of heat, temperature and entropy are thus applied to the nucleus.

The energy spectrum of the emitted particles follows a Maxwellian distribution, and it depends on the nuclear temperature after the emission.
It is expressed as:

$$T = \left(\frac{E_r}{a}\right)^{1/2} \tag{8.7}$$

where E_r is the excited energy of the nucleus (Z, A-1), and a is the level density parameter.
In calculating the temperature T, the value of E_r corresponding to the maximum excitation energy of the residual nucleus is used; while, the parameter a is empirically calculated. The level density parameter is expressed in MeV, and it depends on the number of neutrons and protons of the considered nuclide.

The photoneutrons from evaporation process are emitted with an isotropic angular distribution.

Direct model

In the direct model, the incident particle transfers its energy to a single nucleon. This one is emitted with a energy that depends on:

- its difference with the incident particle energy;
- the nucleon binding energy with the nucleus;
- the possible excitation energy of the remaining nucleus.

The direct process is characterized by an anisotropic angular distribution of the photoneutrons. It can be expressed according to the following function:

$$f(\theta) = 1 + C \cdot sin^2(\theta) \tag{8.8}$$

where θ is the angle between the incident photon and the emitted neutron, while C is an empirical constant depending on materials as a function of the neutron energy.

The direct effect increases as the incident photon energy increases, and the ratio between neutrons emitted by direct effect and evaporative effect is of the order of 13-14%.
In literature there is a spare information about the direct photonuclear effect, but an

algorithm to calculate the percentage of neutrons produced by direct processes is done by [97].

$$F_d = \begin{cases} 0, & (E_\gamma - S_n) < 2.5 \text{ MeV} \\ 0.031, & 2.5 \text{ MeV} < (E_\gamma - S_n) < 9.0 \text{ MeV} \\ 0.2, & (E_\gamma - S_n) > 9.0 \text{ MeV} \end{cases} \tag{8.9}$$

where F_d is the fraction of neutrons directly produced with respect to the total ones: this quantity will thus increase as the excitation energy of the nucleus increases. E_γ is the incident photon energy, and S_n the binding energy of the neutron.
The F_d value as a function of (E_γ - S_n) for different high-Z elements is done by Figure 8.1.

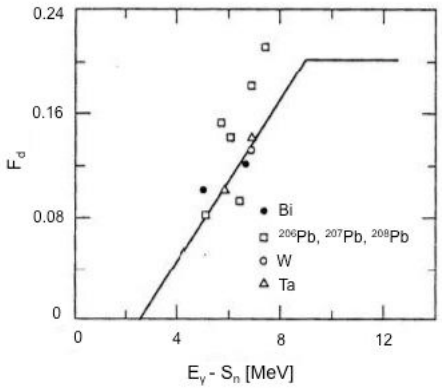

FIGURE 8.1: Fraction of neutrons emitted by the direct process as a function of the energy available for the emission itself [97].

Photonuclear reactions on light elements

By using this simulation code it is possible to calculate the photoneutron spectrum and doses due to photon interactions with heavy elements constituting the LINAC head. However, interactions with light elements constituting the human body must be also take into account in order to evaluate the neutron spectrum and neutron doses in tissue: in this way a correct estimation of the neutron contamination in radiotherapy can be achieved.

Photons with energies range between few MeV and tens of MeV interact with light elements constituting the tissue producing high-LET particles such as neutrons, protons, ^{2}H, ^{3}H, ^{4}He and other heavier particles, depending on the incident beam energy.
In the giant dipole resonance energy range (6 - 20 MeV), of interest for this work, the photonuclear process is dominated by the (γ, n) and (γ, p) reactions, and the maximum of the cross sections is included between 10 mb - 20 mb depending on the considered nucleus (see par. 4.2). For energies higher than 20 MeV the dominated process is the quasi-deuton effect, consisting in the emission of a couple neutron-proton.

The light elements considered by the code (listed in Table 8.1), the corresponding cross sections and the chosen theoretical model refer to the data published by [98].

The used photonuclear model is greatly simplified, considering only direct channel, in which the incident photon transfers all its energy to a single particle, which it is emitted from the nucleus with an energy E_N equal to:

$$E_N = (E - E_{th} - E_e) \cdot \frac{(A - A_N)}{A} \tag{8.10}$$

where E is the incident photon energy, E_{th} is the photonuclear reaction threshold energy, and E_e is the transition energy between the excited state and the ground state of the residual nucleus. The factor [(A - A_N) / A] takes into account the recoil of the residual nucleus, in which A is the atomic mass of the residual nucleus and A_N is the atomic mass of the emitted particle.

TABLE 8.1: Light elements considered in the MCNP4B-GN code, photonuclear reactions and corresponding threshold energies [98]. (γ, n_0) e (γ, n^*) indicate the fundamental state and the excited state, respectively, in which the nucleus remains after the neutron emission.

Element	**Photonuclear reaction**	**Threshold energy** [MeV]
^{16}O	(γ, n_0)	15.7
	(γ, n^*)	21.0
	(γ, np)	23.0
	(γ, 2n)	28.5
^{12}C	(γ, n_0)	18.7
	(γ, n^*)	20.7
	(γ, np)	27.4
	(γ, nα)	26.0
	(γ, npα)	38.0
^{14}N	(γ, n_0)	10.5
	(γ, np^*)	14.08
^{18}O	(γ, n)	8.05
	(γ, 2n)	12.2
^{13}C	(γ, n)	4.95
	(γ, 2n)	23.7
^{23}Na	(γ, n)	12.4
	(γ, np)	19.2
	(γ, 2n)	23.5
^{35}Cl (75.5%)	(γ, n)	12.6
	(γ, np)	17.8
	(γ, 2n)	24.2
^{37}Cl (24.5%)	(γ, n)	10.3
	(γ, np)	18.3
	(γ, 2n)	19.0
^{31}P	(γ, n)	12.3
	(γ, np)	17.9
^{32}S	(γ, n)	15.0
	(γ, np)	21.2
^{39}K	(γ, n)	13.1
	(γ, np)	18.2
^{40}Ca	(γ, n)	15.6

8.2 Monte Carlo simulations: the GEANT4 code

The acronymous GEANT stands for "GEometry ANd Tracking". The code has been created exploiting software engineering and object-oriented technology and implemented in the C++ programming language, for modeling and simulating particles interactions with matter.
It has been designed and constructed to include facilities for handling geometry, tracking, detector response, run management, visualization and user interface.

- *Geometry* is an analysis of the physical layout of the experiment, including detectors, absorbers, etc., and considering how this layout will affect the path of particles in the experiment.
- *Tracking* is simulating the passage of a particle through matter, considering also possible interactions and decay processes.
- *Detector response* is recording when a particle passes through the volume of a detector, and approximating how a real detector would respond.
- *Run management* is recording the details of each run (a set of events), as well as setting up the experiment in different configurations between runs.

Because of its general purpose nature, Geant4 is well suited for development of computational tools for analysing interactions of particle with matter in many fields, including space, medical and nuclear physics applications [99]

8.2.1 How to built a GEANT4 input file

Working with GEANT4 is like making a building set. If "you get the idea, you can build what you want, tailor it to your requirements, but you have to build it yourself" [100].
The general receipt for user includes the so-called **Mandatory classes** (in any user application) and **Action classes** (invoked during the execution of the loop).

The mandatory classes, analysed in the next three subsections, are:

1. *G4VUserDetectorConstruction*, that describes the experimental set-up
2. *G4VUserPhysicsList*, that selects the physics you want to activate
3. *G4VUserPrimaryGeneratorAction*, that generates primary events

while the action classes include:

- *G4VUserPrimaryGeneratorAction*
- *G4UserRunAction*
- *G4UserEventAction*
- *G4UserTrackingAction*
- *G4UserSteppingAction*

Relationships between action classes are represented in Figure 8.2.

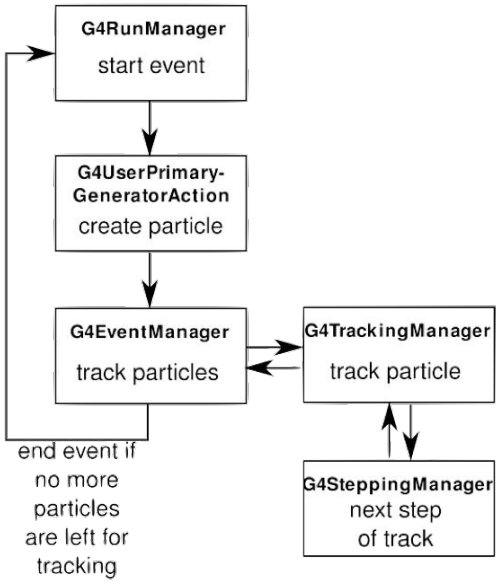

FIGURE 8.2: Block diagram representing the relationships between action classes in GEANT4 (from [101]).

1. Detector construction

The simulated detector geometry and materials are defined by a mandatory class extending *G4VUserDetectorConstruction*.
Geant4 provides many pre-programmed shapes that can be assembled in a hierarchy of volumes. The hierarchy is used as a natural way of embedding volumes within volumes and as an efficient way of navigating through the geometry. However, efficiency comes primarily from an automated process of "voxelisation": the space is divided into slices in three dimensions such that each slice contains only a few volumes, reducing so the computation time for determining the location of tracks within the geometrical model.

To understand how to manage the geometry, see Figure 8.3.
Three conceptual layer are present:

- *G4VSolid*, which gives information about the detector shape and dimensions;
- *G4LogicalVolume*, for adding information about material (G4Material), sensitivity (G4VSensitiveDetector) and visualization (G4VisAttribute);
- *G4VPhysicalVolume*, for adding information about its position, rotation, etc.

The *G4VSensitiveDetector* class should be extended to build a detector; one or more *G4LogicalVolumes* classes can be linked to it, and it is invoked when a particle passes through the associated volume.
The scheme in Figure 8.4 shows how the sensitive detector class works, where the *G4VHit* class stores information (e.g.: position and time of the step, energy deposition of the step, momentum of the track...), while by the *G4UserEventAction* class it's possible to access to the stored hits at the end of events.

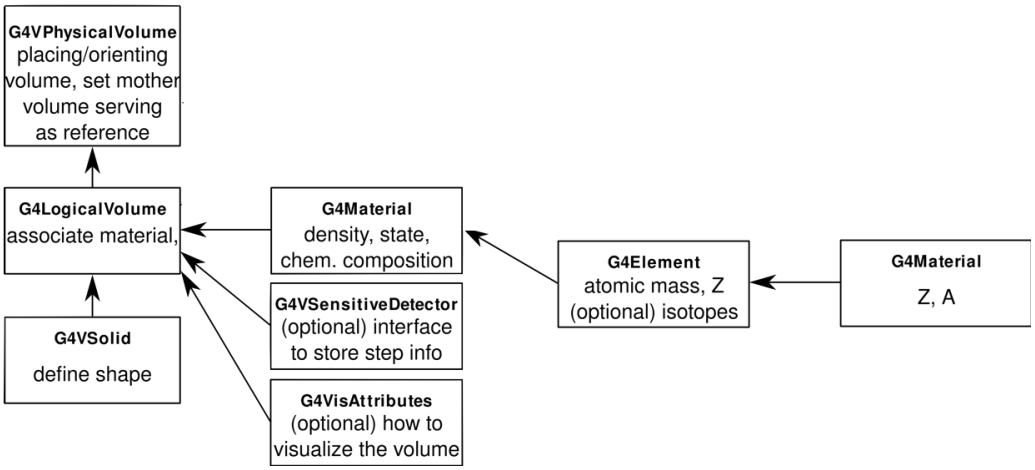

FIGURE 8.3: The geometry management in GEANT4 (from [101]).

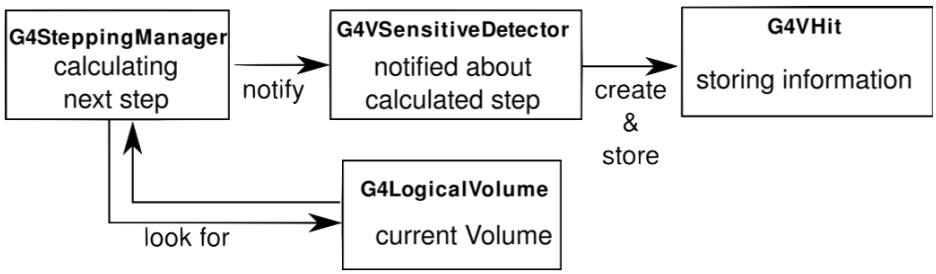

FIGURE 8.4: Bock diagram representing the sensitive detector classes in GEANT4 (from [101]).

2. Physics implementation

The application builder has to code a second mandatory class, called the physics list, that assigns appropriate processes to each particle or ion of interest. Each process can invoke one or more models, depending on the type of particle, energy, etc. Each process randomly competes to be the one that happens. After something happens, the probabilities for happening in the future are updated so that proper distributions are observed.
The user has to choose the correct physics list, and he has to:

- implement all the necessary particles;
- define all the necessary processes and assign the proper particles to them;
- set the energy threshold of the production of the particle.

3. Primary generator action

The last mandatory class is the *G4VUserPrimaryGeneratorAction* abstract class for the generation of primaries. Inside it the user has to set the beam parameters: the shape, the initial energy, the position, the direction, etc.

Chapter 9

PART 1: Measurements of the secondary neutron radiation in radiotherapy

As described in the previous chapters, medical linear accelerators (LINACs) for radiotherapy produce fast secondary neutrons due to photonuclear (γ, n) reactions. Neutron production is governed by the properties of the giant dipole resonance (GDR) reaction and neutrons are generated when the incident photon energy exceeds the GDR reaction threshold (6 - 20 MeV), with a mean energy of about 1 MeV and an isotropic angular distribution. Most of the neutrons are produced by the interaction of the photon beam on high-Z elements constituting the LINAC head (target, scattering foils, collimators, jaws, etc.), in addition to being produced in the bunker walls, floor and ceiling or directly inside the human body. Therefore, a patient undergoing a radiotherapy treatment is affected by an extra unaccounted neutron dose that could represent a risk contribution for the patient, causing for example radio-induced tumours.

For this reason, the first part of the research work was dedicated to performing measurements of the secondary neutron radiation during radiotherapy sessions, in order to estimate the total amount of photoneutrons inside and outside the human body.

The chapter describes measurements performed in Trieste, at Maggiore Hospital, by using the Elekta Synergy Agility LINAC at different megavoltages.

Measurements of the parasitic neutron dose at organs at different LINAC energies

Experimental measurements of the full body parasitic neutron dose equivalent at critical organs, during single-field conformal radiotherapy sessions, were performed in order to investigate the neutron photoproduction provided by a LINAC operating at 15 MV, 10 MV and 6 MV. The aim was to compare the results in terms of, in-field and out-of-field, neutron photoproduction between different energies with the same irradiation conditions.
Each measurement was repeated three times, in the same location, in the same set-up conditions and by using the same LINAC.

9.1 Materials and methods

The LINAC photoneutron production has been investigated during single-field radiotherapy sessions, measuring the neutron dose equivalent in depth in tissue by using a tissue equivalent phantom together with bubble dosimeters.
The LINAC employed was the Elekta Synergy Agility operating in photon mode at 15 MV and at energies near the GDR reaction threshold, 10 MV and 6 MV.
The medical LINAC calibration output was carried out by following the International Code of Practice for Dosimetry IAEA TRS-398 [102]. The relationship of the dose to the number of monitoring units (MU) is 1 cGy = 1 MU at build-up in a water tank, measured with cylindrical chamber (PTW Farmer), with the SSD (source-to-surface distance) equal to 100 cm and the field size of (10×10) cm^2 at isocenter.

The experimental method

Two different kinds of measurements were performed:

1. The neutron dose equivalent at the patient surface plane, to estimate the total amount of photoneutrons in the treatment area
2. The neutron dose equivalent at organs, to measure the full body photoneutron contribution to the patient.

Measurements were carried out with the LINAC gantry at 0°, with an open direct photon beam of (10×10) cm^2 at isocenter.
The patient plane measurements were carried out placing two dosimeters (one for fast and one for thermal neutrons) on the surface of a cubic polyethylene phantom $(30 \times 30 \times 30$ cm$^3)$ at isocenter, with the SSD equal to 100 cm. While, the neutron dose equivalent measurements at organs were performed by using the Trieste anthropomorphic phantom, with the photon beam centered on the pelvis region, having the SSD equal to 92.5 cm and the isocenter at 7.5 cm depth, in correspondence with the prostate position. Eight critical organs were taken into account and two dosimeters (one for fast neutrons and one for thermal neutrons) were placed in each organ position, for a total of 16 detectors employed.
In Figure 9.1 the experimental setup for the second kind of measurements is represented.

9.2 Results and discussion

All results are reported in mSv normalized to 100 MU provided by the LINAC, that is 1 Gy of photon dose absorbed by the patient at build-up in reference conditions. The typical statistical errors are $\sim$5 - 10% due to bubble counting in the range of 300 - 100 bubbles per dosimeter, respectively.

The patient surface plane neutron dose equivalent

Results regarding the patient plane measurements are shown in Figure 9.2 reporting, in logarithmic scale, both the fast and the thermal neutron dose equivalent at the patient surface plane for nominal X-ray energies of 15, 10 and 6 MV. The measured values are summarized in Table 9.1.
From the obtained results, two important considerations have been drawn:

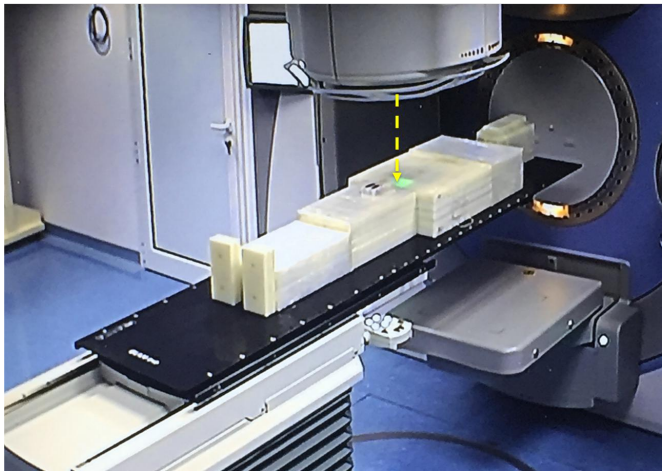

FIGURE 9.1: The Trieste anthropomorphic phantom undergoing the single-field radiotherapy session. The photon beam is centered on the pelvis region and the isocenter is at 7.5 cm depth, in correspondence with the prostate. The irradiation is done with the LINAC gantry at 0°, with a direct open field of (10 × 10) cm^2 at isocenter and with the SSD equal to 92.5 cm.

TABLE 9.1: Patient surface plane neutron dose equivalent per 100 MU for the LINAC operating at 15, 10 and 6 MV. Irradiation setup conditions: field size of (10 × 10) cm^2 at isocenter and SSD of 100 cm. Measurements performed by using BTI detectors.

	Fast neutron dose [mSv / 100 MU]	**Thermal neutron dose** [mSv / 100 MU]
15 MV	1.98 ± 0.20	0.24 ± 0.02
10 MV	0.91 ± 0.09	0.09 ± 0.01
6 MV	0.07± 0.01	0.006 ± 0.001

- The neutron dose equivalent is reduced by a factor ∼2 and by a factor ∼30 of the measured values at 15 MV for data acquired at 10 and 6 MV, respectively.
- It was found that about one-tenth of the fast neutron dose equivalent contribute to the measured value in thermal dosimeters. This value has been so taken into account and excluded in thermal neutron measurements.

The measured neutron dose equivalent per unit of 100 MU values at the patient plane compare reasonably well with those measured by other workers using similar detector technology, for LINACs operating at 15 and 10 MV [46], [103]. While the photoneutron production in lower energy LINACs, at 6 MV, is usually ignored.

The parasitic neutron dose equivalent at organs

Results of the BTI measurements at organs during the single-field 15 MV and 10 MV test irradiations are summarized in Figure 9.3. For each critical organ, the first column represents the total neutron dose equivalent (fast plus thermal), the second one is the fast neutron component, while the third column corresponds to the thermal

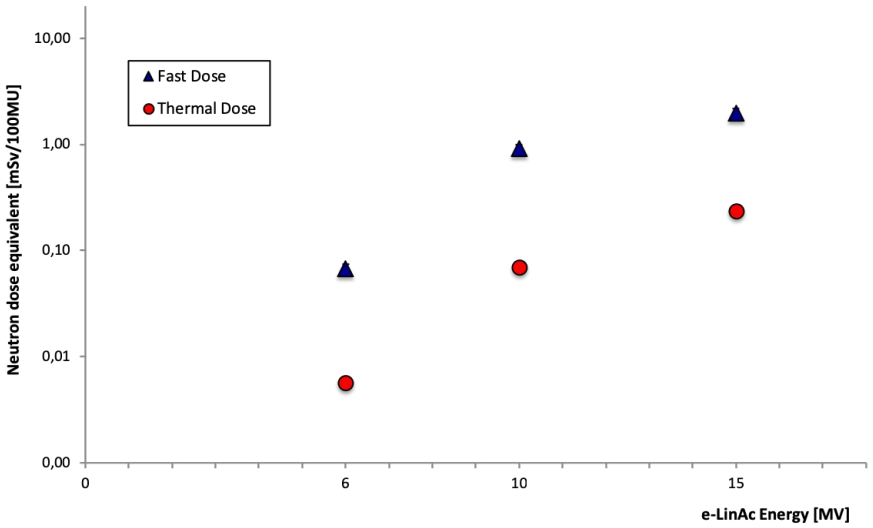

FIGURE 9.2: Fast and thermal neutron dose equivalent at the patient surface plane for a 6, 10 and 15 MV LINAC operating in photon mode. Logarithmic scale. Irradiation setup conditions: photon field size of (10×10) cm^2 and SSD equal to 100 cm. BTI measurements.

component. Results for the 6 MV irradiation are instead reported in Figure 9.4.
At nominal X-ray energies of 15, 10 and 6 MV, the in-field recorded values are 2.05 $\pm$ 0.2, 0.56 $\pm$ 0.06 and 0.031 $\pm$ 0.003 mSv/100 MU, respectively. In the remaining critical organs, the neutron dose equivalent decreases out-of-field and going deep in phantom, due to neutron moderation and absorption in tissue. Notice that in experimental cases like this one described, the last statement could be slightly not accurate: neutrons could be also produced in the bunker walls, floor and ceiling, in a complex and mostly unknown way, giving a contribution to an organ rather than to another one. Only at 6 MV the out-of-field neutron dose equivalent contribution is less than 0.1% of the photon dose and it may be considered negligible, while photoneutrons are still present in the treatment area.
In Figure 9.5, all the obtained results are plotted together in logarithm scale. It is so possible to notice that the total neutron dose equivalent trend at organs is the same for each simplified direct beam irradiation. Moreover, in the treatment area, in the prostate position, the neutron dose equivalent to the patient is is maximum at 15 MV, 4 times lower at 10 MV and 72 times lower at 6 MV. This factor increases going far away from the radiation field, but the neutron dose equivalent is not negligible except for the 6 MV irradiation.

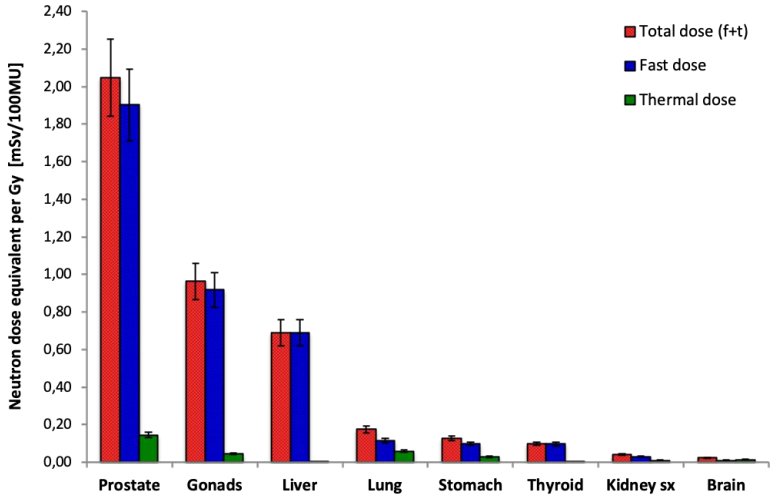

(A) Neutron dose equivalent at organs for the 15 MV LINAC.

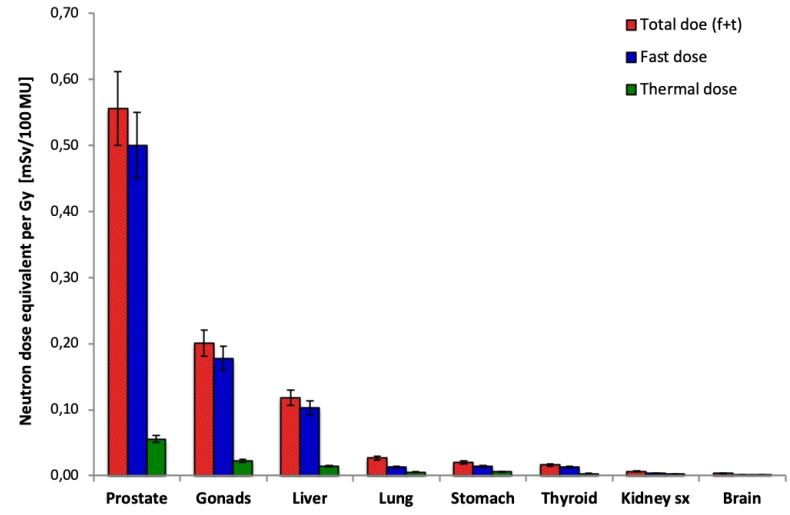

(B) Neutron dose equivalent at organs for the 10 MV LINAC.

FIGURE 9.3: Neutron dose equivalent per 100 MU at organs for the LINAC operating at 15 MV and 10 MV. Photon field centered on the pelvis region. SSD: 92.5 cm; isocenter: 7.5 cm depth in phantom in correspondence with the prostate; field size: (10×10) cm^2 at isocenter. BTI measurements.

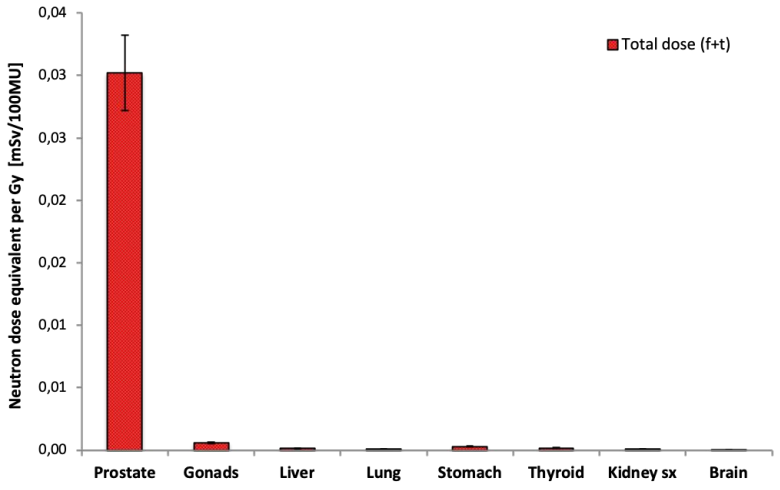

FIGURE 9.4: Neutron dose equivalent per 100 MU at organs for the LINAC operating at 6 MV. Photon field centered on the pelvis region. SSD: 92.5 cm; isocenter: 7.5 cm depth in phantom in correspondence with the prostate; field size: (10×10) cm^2 at isocenter. BTI measurements.

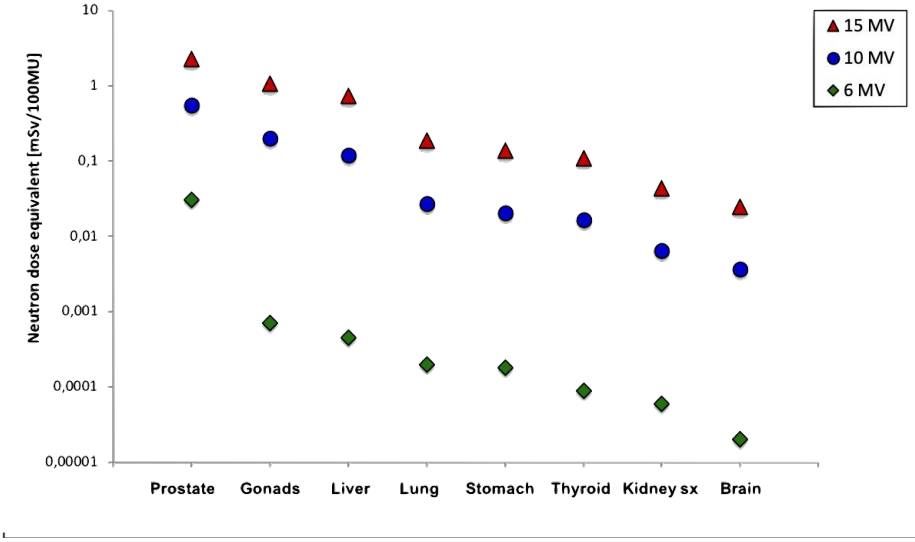

FIGURE 9.5: Total neutron dose equivalent per 100 MU at organs provided by a 15, 10 and 6 MV LINAC. Logarithmic scale. Photon field centered on the pelvis region. SSD: 92.5 cm; isocenter: 7.5 cm depth in phantom in correspondence with prostate; field size: (10×10) cm^2 at isocenter. BTI measurements.

9.3 Conclusions

The photoneutron production in the Elekta Synergy Agility LINAC operating at 15, 10 and 6 MV was investigated for an anthropomorphic phantom undergoing single-field radiotherapy sessions. The parasitic neutron dose equivalent was measured by using bubble detectors both at the patient surface plane and inside critical organs, maintaining the same experimental setup conditions within the two kinds of measurements in order to compare results among the three studied operating LINAC megavoltages.
Several studies about the photoneutron dose measurements, with different dosimetric system such as bubble detectors, polycarbonate film, activation detectors and thermoluminescance dosemeters, are present in literature [46], [45], [104]. However, there is sparse information about photoneutrons provided in lower megavoltages LINACs, near the GDR reaction threshold, at 10 MV and 6 MV.
The measured neutron dose equivalent per unit of 100 MU values at the patient plane compare reasonsobly well with those measured by other workers using similar detector technology, for LINACs operating at 15 and 10 MV [46], [103]. While the photoneutron production in lower energy LINACs, at 6 MV, is usually ignored.

From this first part of the research work it emerges that a patient undergoing a conventional radiotherapy treatment, with energies $E \geq 10$ MV, is always affected by an extra usually unaccounted neutron dose, which could cause radio-induced tumours representing a risk factor for the patient.
The residual neutron photoproduction is also present at energies near the GDR reaction threshold. It is $\sim$20% and $\sim$3% of the measured values at 15 MV for data acquired at 10 and 6 MV, respectively. These values increase during a treatment due to neutron thermalization and absorption in the human body, but the neutron contribution is not negligible at 15 and 10 MV. Although a slight amount of photoneutrons are provided by a 6 MV LINAC, it should not be completely neglected in clinical applications, especially considering other kind of treatments in which the use of multileaf collimators or lead blocks could increase the neutron photoproduction.

Chapter 10

PART 2: The BNCT contribution in radiotherapy

During X-ray radiotherapy treatments by using electron medical linear accelerators with accelerating potentials above 10 MV, patients undergo an extra unaccounted neutron dose. Emitted photoneutrons cannot be ignored and represent a risk factor for patients, since neutrons could cause secondary radio-induced tumours. Moreover, neutrons are moderated by elastic collisions on light elements (H, C, O, N) constituting the human body: therefore, a consistent thermal neutron field is present in the treatment area. The research work aims at investigating the possibility to employ the thermal neutron field to combine a "BNCT contribution" to the traditional radiotherapy treatment, improving the radiotherapy effectiveness.

The second part of the work was thus focused on performing simulations and measurements quantifying the thermal neutron field in the treatment zone during a conventional radiotherapy treatment in order to calculate the additional BNCT equivalent dose.
This part of the work was performed in Turin, by using the 18 MV Varian 2300CD LINAC and the Torino anthropomorphic phantom with inside thermal neutron bubble detectors.

10.1 Materials and Methods

The BNCT contribution in radiotherapy was investigated during a simplified prostate cancer treatment, by using an open direct field centered on the gonads position at 4 cm depth in phantom.
The irradiation set-up conditions are: LINAC operating in photon mode at 18 MV accelerating potential; gantry at 0°; photon field size of (10 $\times$ 10) cm^2 at isocenter; SSD = 96 cm.
The LINAC calibration output is such that 1 cGy = 1 MU at build-up in a water tank, when the SSD = 100 cm and the photon field size is (10 $\times$ 10) cm^2 at isocenter.

The experimental set-up is shown in Figure 10.1, in which it's possible to see the Torino anthropomorphic phantom undergoing the radiotherapy session. The total structure, the LINAC plus the phantom, was considered in the MCNP4B-GN input file.

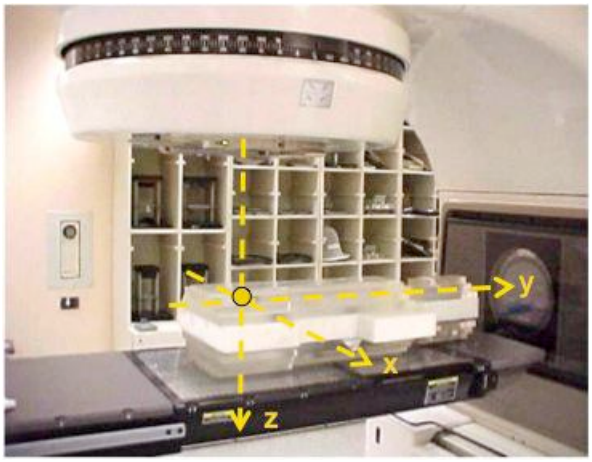

FIGURE 10.1: The Torino anthropomorphic phantom undergoing the single-field radiotherapy session. The photon beam is centered on the pelvis region and the isocenter is at 4 cm depth, in correspondence with the prostate position. The irradiation is done with the LINAC gantry at 0°, with a direct open field of (10 × 10) cm^2 at isocenter and with the SSD equal to 96 cm.

10.1.1 Simulation of the experimental set-up

This section describes the data entered into the simulation file for characterizing both the accelerator and the anthropomorphic phantom.

The 18 MV Varian 2300CD LINAC

The accelerator head components included in the simulation file are summarized in Table 10.1, for the 18 MV Varian 2300CD LINAC, reporting its materials and their approximate shapes.
The axes origin was placed in the target centre, with the z-axis pointing downwards, along the isocenter line.

The representation of the simulated LINAC head is shown in Figure 10.2. Notice that multileaf collimators were not considered in the input file: MLC is not used for a conventional radiotherapy treatment like the one here studied.
From an operational point of view the LINAC beam parameters can be summarized as follow (Table 10.2):
From this parameters it is possible to obtain the effective electron flux impinging on the target by the relation:

$$6.25 \cdot 10^{18} \cdot I \cdot \nu \cdot T = 1.05 \cdot 10^{14} \frac{e^-}{s} \tag{10.1}$$

where 6.25· 10^{18} is the inverse of the electron charge. It represents the number of electrons per second for a current of 1 Ampere.

The effective electron current on the LINAC target is thus of the order of $\sim 10^{14}$ e^-/s.

This value varies following the energy and technical characteristics of the accelerator, and it is used as a normalization factor for the simulation results (expressed per

TABLE 10.1: Summary table of the Varian LINAC head components.

Head components	**Distance from the target** [cm]	**Materials**	**Approximative shapes**
Target source	0.0	Tungsten and Copper	two coaxial cylinders
Primary collimator	upper surface: 1.6 lower surface: 7.8	Tungsten	truncated hollow cone
Flattening filter	12.5	Iron and Tantalum	inverted cone
Upper secondary collimator	upper surface: 28.0 lower surface: 35.8	Tungsten	pair of parallelepipeds
Lower secondary collimator	upper surface: 48.2 lower surface: 53.5	Tungsten	pair of parallelepipeds

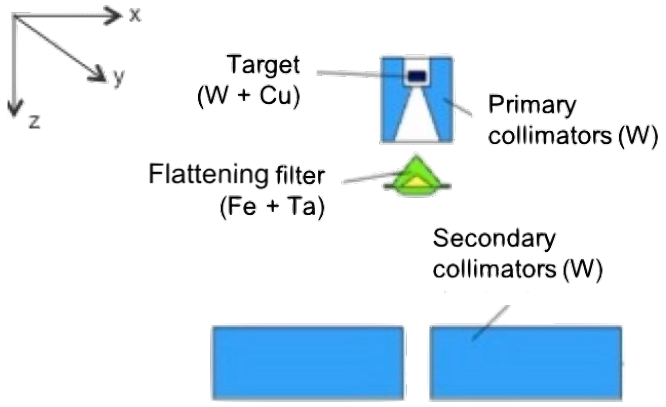

FIGURE 10.2: Representation of the Varian 2300 LINAC head simulated by MCNP4B-GN code. The target (made up by tungsten and copper), flattening filter (iron and tantalum), primary and secondary collimators (tungsten), are represented. Section on plane y = 0. The origin of the reference system is placed in the centre of target and the z-axis is directed downward, along the isocenter line.

TABLE 10.2: Beam parameters for the 18 MV Varian 2300CD LINAC. Characteristics of the electron beam impinging on the target.

Technical characteristics	Values
Maximum energy	18 MeV
Effective pulse duration, T	2.4 μs
Electron current, I	35 mA
Repetition rate, ν (frequency electron pulse)	200 Hz
Beam power	264 W

a single source electron): the higher is the number of electrons striking on the target, the higher is the number of X-rays produced by Bremsstrahlung and, consequently, the amount of neutrons produced by the GDR reaction.

The Torino anthropomorphic phantom

The anthropomorphic phantom was implemented in the simulation input file at 96 cm from the origin of reference system (the LINAC target); the secondary collimators were opened in order to make a 10 cm $\times$ 10 cm square at isocentre. The photon beam was centered on the gonads position at 4 cm depth in phantom.

The new organs coordinates referred to the simulation reference system (Figure 10.3) are reported in Table 10.3.

The cavities in correspondence of organs were simulated with spheres, having 1 cm radius and centre in the position reported in Table 10.3. The chemical composition of the corresponding tissue/organ, tabulated in the ICRU 44 and reported in Table 10.4, was also inserted.

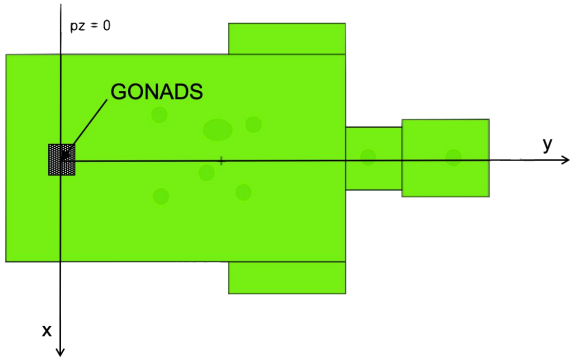

FIGURE 10.3: Reference system for determining organs position. The beam is centered on the gonads position.

TABLE 10.3: Organs positions inside the Torino anthropomorphic phantom, following the simulation reference system.

Organs	**x** [cm]	**y** [cm]	**z** [cm]
Gonads	0.0	0	98.0
Bladder	0.0	7.2	102.0
Liver	-5.0	26.5	102.0
Esophagus	0.0	29.7	102.0
Right Colon	-7.5	16.7	106.1
Left Colon	6.5	16.7	106.1
Stomach	2.0	25.0	106.1
Right Lung	-6.0	32.9	106.1
Left Lung	6.0	31.0	106.1
Thyroid	0.0	52.5	106.1
Brain	0.0	67.3	106.1
Spleen	9.5	16.0	110.3
Left Kidney	4.0	17.8	112.0
Right KIdney	-5.5	19.0	112.0
Low Column	0.0	18.8	112.0
Half-height Column	0.0	34.0	112.0

TABLE 10.4: Elemental composition (in percentage mass) of organs according to ICRU 44.

Organs	**H** [w%]	**C** [w%]	**N** [w%]	**O** [w%]	**Density** $[g/cm^3]$
Gonads	10.6	9.9	2.0	76.6	1.04
Bladder	10.2	14.3	3.4	71.0	1.05
Liver	10.2	13.9	3.0	71.6	1.06
Esophagus	10.2	14.3	3.4	71.0	1.05
Colon	10.6	11.5	2.2	71.5	1.03
Stomach	10.2	14.3	3.4	71.0	1.05
Lung	10.3	10.5	3.1	74.9	1.05
Thyroid	10.4	11.9	2.4	74.5	1.05
Brain	10.7	14.5	2.2	71.2	1.04
Spleen	10.3	11.3	3.2	74.1	1.06
Kidney	10.3	13.2	3.0	72.4	1.05
Bone	3.4	15.5	4.2	43.5	1.92

10.2 Results

All the results are normalized to 1 Gy of photon dose absorbed by the phantom at build-up.

Results can be summarized as follows:

- simulation of the neutron spectrum provided by the LINAC at the patient plane
- simulation of the neutron spectrum in depth in tissue
- simulation of the neutron fluence at organs when the photon beam is centered in the gonads position
- comparison between simulation and experimental results
- calculation of the additional BNCT equivalent dose at different depth in tissue

Neutron spectrum at patient plane

The typical photoneutron energy spectrum simulated by using the 18 MV VARIAN 2300CD LINAC at patient plane in standard condition during a single-field radiotherapy treatment is shown in Figure 10.4.

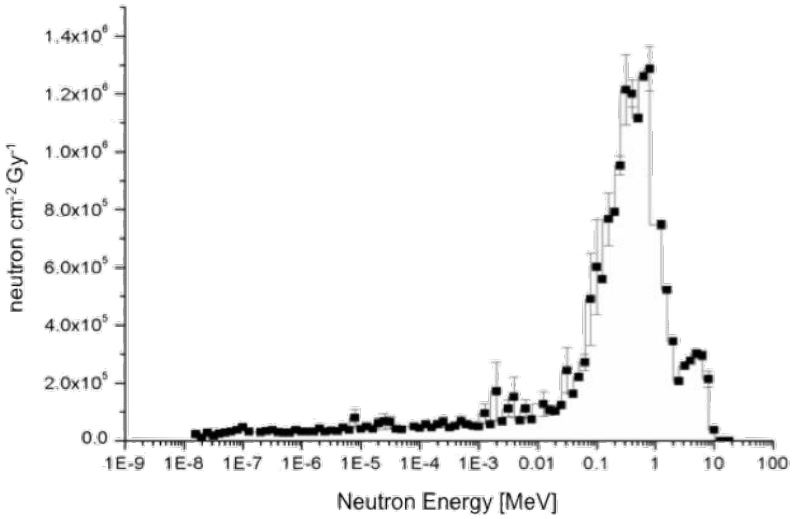

FIGURE 10.4: Neutron fluence per Gy at the patient plane during a direct single-field radiotherapy treatment. 18 MV VARIAN 2300CD LINAC. Irradiation conditions: SSD=96 cm; photon field= (10 × 10) cm^2 at isocenter. Simulation result carried out by the MCNP4B-GN code. The mean neutron energy is around 1 MeV, in the fast energy range.

As expected, the mean neutron energy ranges between 700 keV and 1 MeV [37], in the fast neutron energy range. The dominant energy peak centered around 1 MeV is due to the evaporative mechanism, in which the neutron angular emission is isotropic, and the energy distribution follows the Maxwellian curve. Moreover, a

peak can be observed for energies higher than 3 MeV due to direct-reaction neutron knockout component: in this case the angular distribution is anisotropic, f(θ) = a + b(sinθ)^2, and the energy distribution is given by the difference between the photon energy and the binding energy, E_n = Eγ- E_b (see paragraph 8.1.1).

Neutron spectrum in depth in tissue

The photoneutron energy spectrum inside the phantom at isocentre, at 4 cm depth in tissue, is shown in Figure 10.5: an intense thermal neutron peak of about 1.55 $\times$ 10^7 cm^{-2} Gy^{-1} arises in the lower energy range (between 0.001 eV and 0.4 eV), inside the treatment zone, due to fast neutrons moderation in tissue.

Moreover, it was simulated how the neutron fluence changes at different depth in tissue (Figure 10.6): the relative importance of thermal and fast neutron components change with depth in phantom. Going deeper in tissue, fast neutron component is thermalized, while thermal component is then absorbed. By considering the ratio between the thermal and fast neutron component at each depth in phantom, without losing the thermal component, the most favourable depth where more thermal neutrons are present is between 4-5 cm.

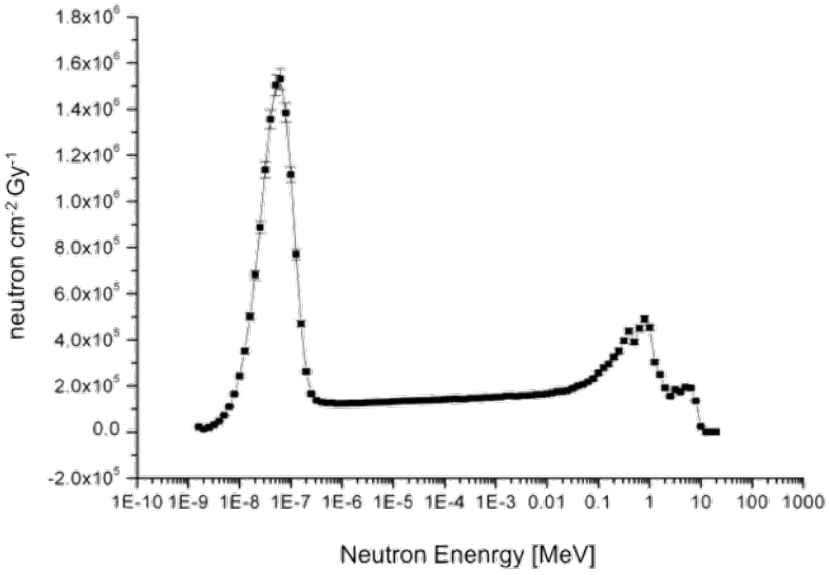

FIGURE 10.5: Neutron fluence per Gy at 4 cm depth in tissue during a direct single-field radiotherapy treatment. 18 MV VARIAN 2300CD LINAC. Irradiation conditions: SSD=96 cm; photon field= (10 $\times$ 10) cm^2 at isocenter; isocenter at 4 cm depth in tissue. Simulation result carried out by the MCNP4B-GN code. The fast neutron component is thermalized and an intense thermal peak of $\sim$ 10^7 cm^{-2} Gy^{-1} arises in the lower energy range.

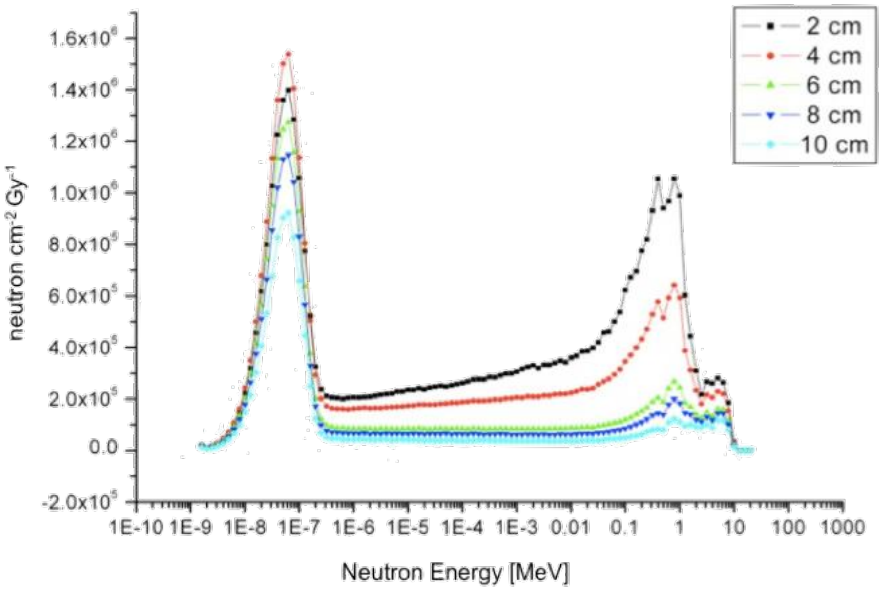

(A) Neutron spectrum at different depth in tissue.

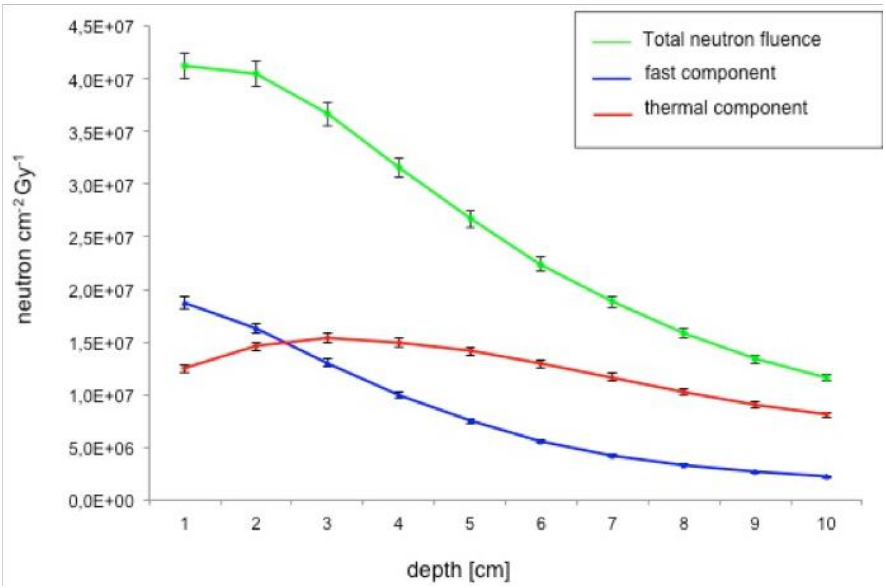

(B) Neutron fluence per Gy at different depth in tissue.

FIGURE 10.6: Neutron spectrum (A) and neutron fluence per Gy (B) at different depth in tissue, simulated by the MCNP4B-GN code. Irradiation conditions: 18 MV VARIAN 2300 CD LINAC; SSD=96 cm; photon field= (10 $\times$ 10) cm^2 at isocenter. The relative importance of thermal and fast neutron components change with the depth in tissue.

Neutron equivalent dose at organs

To study the neutron equivalent dose at organs, the following inputs were implemented in the simulation file:

- fluence-to-dose conversion coefficients, tabulated in the ICRP 116 [40]. (Their trend as a function of energy is shown in Figure 10.7).
- radiation and tissue/organ weighting factors, w_R and w_T respectively (see par. 2.3.2).

In Figure 10.8A is reported the neutron fluence per Gy in organs for the thermal (neutrons with energies up to 0.4 eV) and fast (neutrons with energies above 100 keV) components; while, in Figure 10.8B the corresponding calculated neutron equivalent dose for the thermal component. In this way it was also possible to make a comparison with experimental measurements carried out with thermal neutron bubble dosimeters BDT, keeping the same the irradiation set-up conditions.

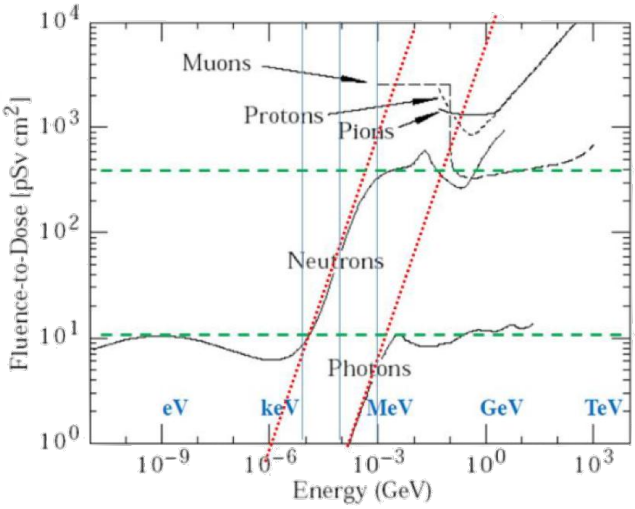

FIGURE 10.7: Fluence to dose conversion coefficients trend as a function of energy, for different types of radiation [40]. Looking at the curve corresponding to neutrons, for thermal energies the neutron curve is quite constant: the fluence to dose conversion coefficient is about 10 pSv·cm^2.

The additional BNCT equivalent dose

To evaluate the additional dose due to BNCT it is necessary to take into account the various physical dose components, arising from neutrons and gamma interactions with biological tissues and ^{10}B captured by cells.

As described in section 5.2.1, the total physical dose consists of the gamma dose ($D\gamma$), due to gamma of 2.2 MeV from thermal neutron capture reactions on hydrogen in tissue; the fast neutron dose or hydrogen dose (D_H), due to recoil protons from fast neutron reactions in tissue; the thermal neutron dose or nitrogen dose (D_N), from thermal neutron reactions by nitrogen nuclei, and the boron dose (D_B), due to the neutron capture reactions by ^{10}B that absorbs a thermal neutron.

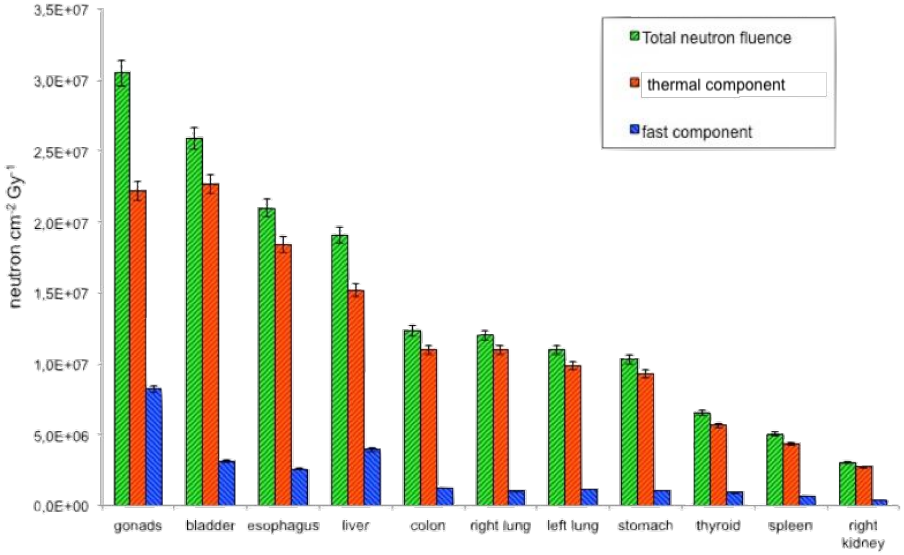

(A) Neutron fluence per Gy components at organs for thermal and fast components. MCNP4B-GN simulation results. Neutron fluence decreases moving away from gonads position and going deeper in phantom.

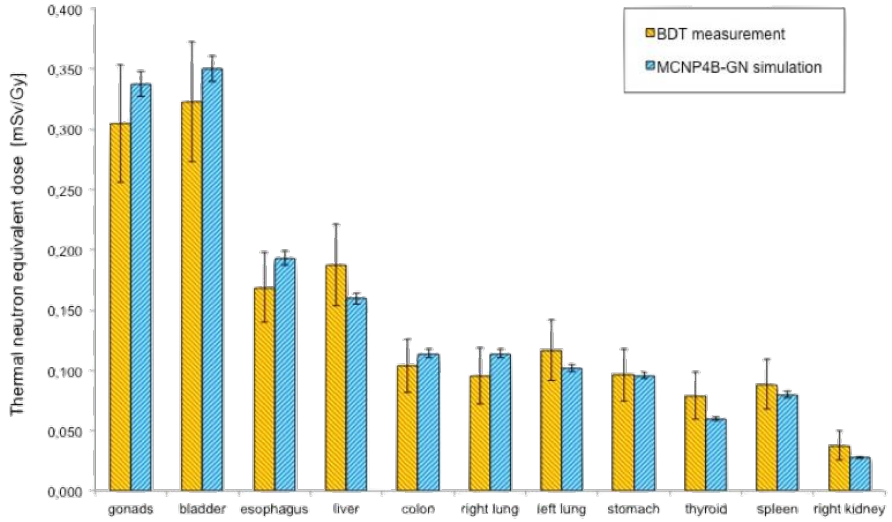

(B) Thermal neutron equivalent dose at organs. Comparison between BDT measurement and MCNP4B-GN simulation results. Accuracy BDT: 20%. Considering neutron absorption in depth in tissue, neutron dose distribution is uniform at organs. The peak in the irradiation zone is also due to neutrons directly produced in human body.

FIGURE 10.8: Neutron fluence per Gy in organs (A) and thermal neutron equivalent dose at organs (B). Irradiation conditions: 18 MV VARIAN 2300 CD LINAC; SSD=96 cm; photon field= (10×10) cm^2 at isocenter; isocenter at 4 cm depth in phantom; photon beam centered in gonads position.

Remember that, in order to compare the BNCT dose with the fractionated absorbed dose in photon radiotherapy, the physical dose needs to be converted to biological dose multiplied by their relative biological effectiveness: the BNCT dose is so measured in Gy-eq.

All the dose components were calculated by integrals such those described in section 5.2.2, considering a thermal neutron total fluence in treatment zone of 1.55×10^7 cm^{-2} per Gy and a typical healthy-to-tumour tissue ^{10}B concentration ratio of 1:3, with a blood boron concentration of 11 parts per million (ppm) and 30 ppm. By using these parameters and considering the phantom exposure as in Fig. 10.1, the BNCT equivalent dose profiles in depth in tissue and its physical dose components are shown in Figure 10.9, by using the CBE factors of 3.8 in tumour tissues and 1.3 in healthy ones in absence of more accurate values (see section 5.2.1, [52]).
The additional BNCT dose delivered for 1 Gy of photon absorbed dose at 4 cm depth in phantom, where the treatment target is, is about 1.5 mGy-eq/Gy.

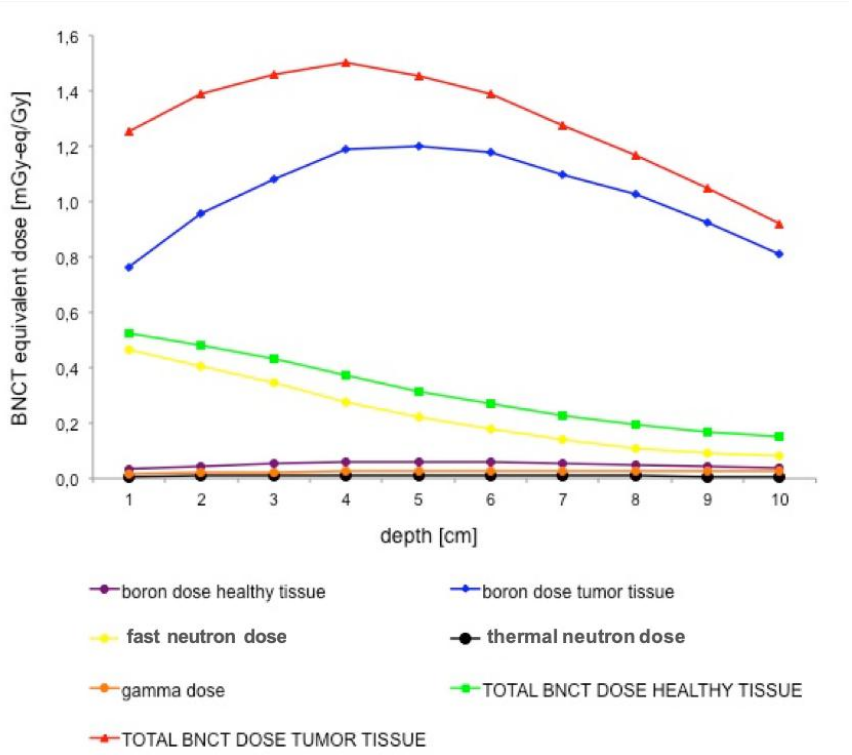

FIGURE 10.9: BNCT equivalent dose profiles in depth in tissue and its different physical dose components calculated for a thermal neutron fluence of 1.55×10^7 cm^{-2} Gy^{-1} and a healthy-to-tumour tissue ^{10}B concentration ratio of 1:3, with a blood boron concentration of 11 parts per million (ppm) and 30 ppm. MCNP4B-GN simulation results. It can be observed that the total BNCT dose to tumour tissue, red line, is mainly due to the boron dose to tumour tissue, blue line. The total dose to healthy tissue, green line, is mainly due to the fast neutron component, yellow line, always present during a radiotherapy treatment; the boron-10 carrier perfusion, violet curve, is negligible, it does not affect healthy tissue.

In a conventional 70 Gy radiotherapy treatment, the BNCT additional dose is thus about 0.11 Gy-eq. This value depends on the LINAC characteristics and energy, from

the collimation system, and from different radiotherapy treatment protocols. This contribution could considerably increase when the improvement in photon beam collimation requires a longer time to deliver a certain dose to target volume and also an accurate evaluation of the LINAC output factor (OF), (par. 4.5.2). As a matter of fact, a greater number of Monitor Unit (MU), linked to OF, corresponds to a major neutron flux. For example, during a 70 Gy IMRT radiotherapy treatment (1815 MU with respect to 100 MU for traditional radiotherapy treatment), patients could undergo an additional BNCT dose component, localized inside tumour cells, of about 3 Gy-eq (i.e. 4% of the therapeutic X-rays dose). This value, calculated by Monte Carlo simulations, takes into account the total BNCT dose to tumour tissue. This additional dose could thus improve radiotherapy, acting as a localized radio-sensitizer.

10.3 Conclusions

In this part of the research work, the possibility to perform a treatment by coupling conventional high-energy radiotherapy with an additional dose contribution from thermal neutrons is investigated.
A patient undergoing a conventional radiotherapy treatment is always affected by an extra unaccounted neutron dose, which presents an intense thermal neutron field ($>10^7$ cm^{-2} Gy^{-1}) localized in the tumour region. If a boron-10 enriched compound is previously administered to the patient, if the ratio ^{10}B in cancer cells compared to ^{10}B concentration in healthy tissues is sufficiently high and the carrier is uniformly distributed in cancer cells, this neutron component could produce a localized BNCT effect with a localized therapeutic dose enhancement, following tumour characteristics.
This application is a preliminary study of the possibility to use parasitic neutrons for the enhancement of radiotherapy treatments. In routine photon treatments the dose is usually delivered in many fractions, so the clinical application at present seems to be not possible in practice. However, it could be of interest in the future because of the new trend in radiotherapy, consisting of dose escalation and in dose hypo-fractioning, i.e. using a very high MU number per Gy (until 2000 MU/Gy) administering the total therapeutic dose, and consequently the ^{10}B-carrier, in only few sessions.

Chapter 11

PART 3: Development of a compact neutron photo-converter-moderator

The research work is part of the e-LiBANS project. The acronym e-LIBANS stands for "electron-LINAC Based Actively monitored Neutron Sources". The idea is to produce neutrons via photonuclear (γ,n) reaction and then to moderate them in a dedicated assembly: the photoconverter [105].
The e-LiBANS project profits of knowledge and experience from previous projects, first of all, the PhoNeS project [106], whose aim was the developing of a portable photoneutron source made by a photoconverter suitable to be applied to medical LINACs for studies on boron neutron capture therapy.
A selection of suitable materials was made on the basis of a cross section analysis and a radiation protection study, avoiding, for example, the production of radioactive materials [107].

Unlike the e-LiBANS and PhoNeS projects, in this work a compact assembly of the photoconverter was developed. The intent was to perform a combined treatment, by coupling the radiotherapy with an additional dose contribution from thermal neutrons, and not to produce a pure thermal or epithermal neutron field inside a cavity.

This third and last part of the research work was performed in Trieste, at Maggiore Hospital. The Elekta Synergy Agility LINAC was used in photon mode with 15 MV accelerating potential, coupled with the photoconverter and a simplified parallelepiped polyethylene phantom.

11.1 Performance of the neutron photo-converter-moderator assembly

A neutron photo-converter-moderator set-up, with an overall compact size [(20 $\times$ 20 $\times$ 24) cm^3], was designed and assembled in order to improve the thermal neutron field in the treatment region, without compromising the therapeutic photon beam.

This section shows measurements for assessing the photoconverter performance.

11.1.1 Materials and Methods

The photoconverter geometry is shown in Figure 11.1. It is made up by a 10 cm thick [(10 × 10) cm^2 wide] lead neutron target (2 lead blocks of 5 cm thick each), followed by 4 cm thick polyethylene and by 10 cm thick [(20 × 20) cm^2 wide] of carbon fiber box filled with heavy water moderator.
Photoneutron cross-section on lead shows a maximum of 600 mb for E_γ = 13.5 MeV. The convolution of this peak with the bremsstrahlung spectrum gives the theoretically expected amount of emitted neutrons, which have an energy spectrum characterized by a most probable energy around 1MeV. Neutrons can then be thermalized mainly through elastic scattering in moderator materials: heavy water was thus chosen for its high moderation power combined with its low neutron capture cross section.

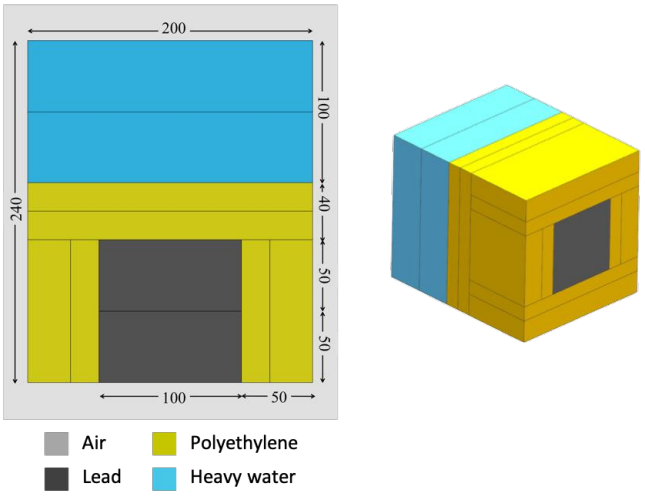

FIGURE 11.1: Plot of the photo-converter-moderator assembly. On the left, a longitudinal view, where the beam direction is bottom-top. On the right, a 3D view.

Measurements, by using lead blocks of 5 cm and 10 cm thick, were carried out in order to assess the neutron photo-converter-moderator performance.
Two kinds of measurements, for each configuration, were performed in depth in phantom:

1. the photon absorbed dose, by using radiochromic films EBT3;
2. the neutron dose equivalent, by using passive bubble dosimeters for thermal and fast neutrons (BDT and BD-PND respectively).

Measurements were performed by using the Elekta Synergy Agility LINAC in photon mode, operating at 15 MV accelerating potential, coupled with the photoconverter and a simplified parallelepiped polyethylene phantom of (30 × 30 × 22) cm^3 dimensions.
The phantom is made up by several slabs, and bubble dosimeters and EBT3 radiochromic films were located inside it at different depth.
The irradiation was performed by using an open direct field of (10 × 10) cm^2 at isocentre; the isocentre was at 10 cm depth in phantom; SSD = 90 cm; LINAC gantry

= 90°.
Each measurement was repeated three times, in the same location, in the same set-up conditions and by using the same LINAC.

The experimental set-up is shown in Figure 11.2.

11.1.2 Results

Results are reported in mSv normalized to 100 MU provided by the LINAC. The typical statistical errors are $\sim$ 5-10% due to bubble counting in the range of 300-100 bubbles per dosimeters, respectively.

The photon absorbed dose in depth in phantom

Regarding the in-phantom photon absorbed dose as a function of depth, the depth-dose curves (PDDs) are reported in Figure 11.3, both for the configuration without the photoconverter and for the photoconverter with 5 cm and 10 cm thick lead shield.
By calculating the tissue-phantom ratio (TPR), it was possible to know which megavoltage photon beam corresponds the found PDDs (see section 3.2.1, eq. 3.5 and Table 3.1). Both for 5 cm and 10 cm thick lead, the calculated $TPR_{20,10}$ is about 0.67, which corresponds to a 6 MV photon beam: this is due to the minimum photon cross section on lead (see Fig. 4.2).
The attenuation factor at build-up was also calculated. The photon beam is attenuated by a factor of $\sim$8 between the configuration without the photoconverter assembly and the photoconverter with 5 cm thick lead shield, and by a further factor of $\sim$9 between the photoconverter with 5 cm and 10 cm thick lead shield.

Moreover, the photon beam profiles were measured checking for the beam deterioration after using the photoconverter. Figure 11.4 shows the photon beam cross profiles at different depth in phantom for a photon field size of (10 $\times$ 10) cm^2 at isocentre by using the photoncervert with 10 cm thick lead shield. The photon profiles are very similar to the ones measured by Dawod et al. [108] for the same field size and the same megavoltage LINAC. The photon beam is not so spread out with the photoconverter, it is still well collimated: the photon field is not deteriorated.

By using the photo-converter-moderator assembly, the photon field is modified without degrading the quality of the therapeutical beam.

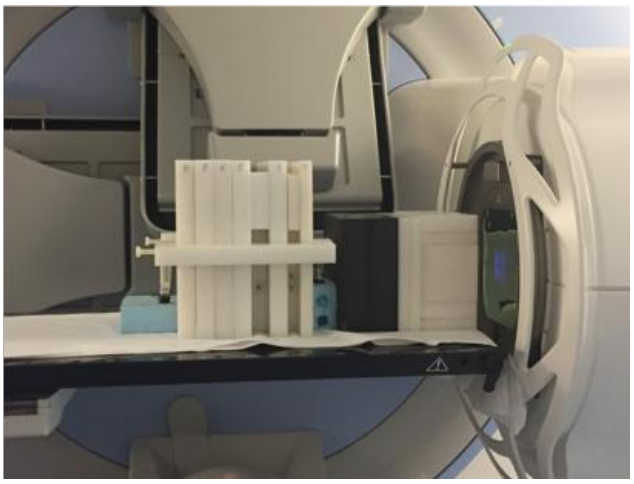

(A) Set-up for the neutron dose equivalent measurements. Bubble dosimeters were placed in suitable holes inside the phantom at 0 cm, 3 cm, 8 cm, 23 cm depth. Two dosimeters, one for fast and one for thermal neutrons, were located in each position.

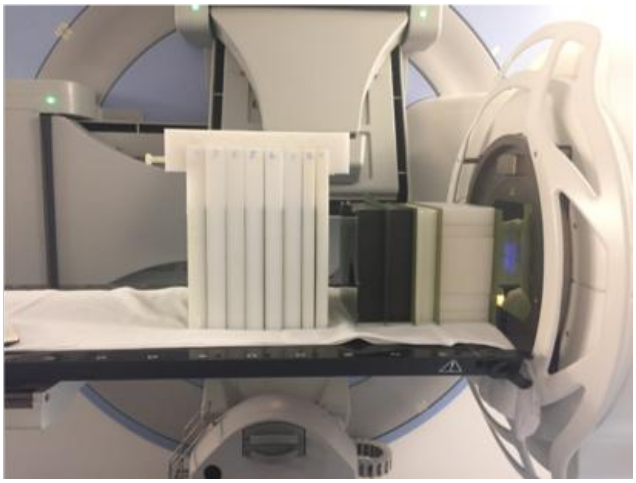

(B) Set-up for the photon absorbed dose measurements. Gafchromic EBT3 films were placed between the phantom slabs at 2 cm, 4 cm, and then every 3 cm up to 22 cm depth.

FIGURE 11.2: Experimental set-ups for assessing the photo-converter-moderator performance. 15 MV Elekta Synergy Agility LINAC; photon field = (10×10) cm^2 at isocentre; SSD = 90 cm; isocentre at 10 cm depth in phantom; LINAC gantry at 90°.

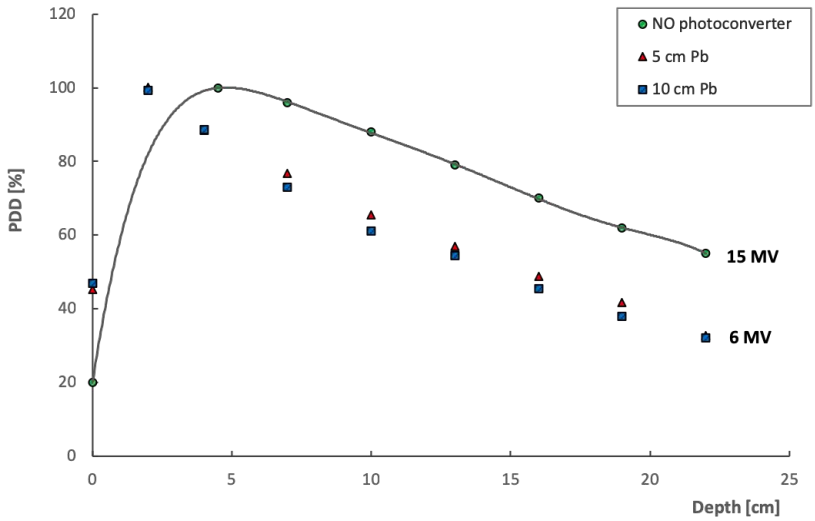

FIGURE 11.3: Percentage depth dose curves of the photon beam. Configuration without the photoconverter assembly, and with the photoconverter with 5 cm and 10 cm thick lead. Both for 5 cm and 10 cm thick lead shield, the calculated $TPR_{20,10}$ is about 0.67, which corresponds to a 6 MV photon beam [32].

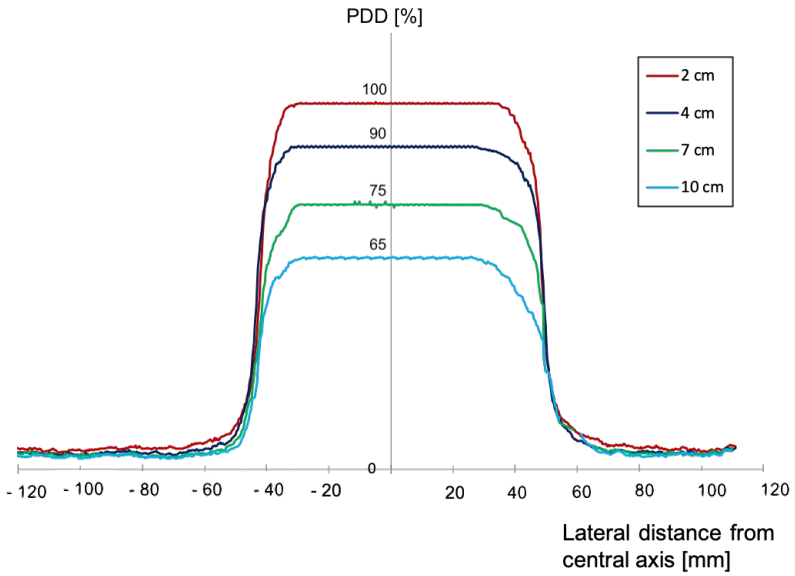

FIGURE 11.4: Photon beam cross profile at different depth in phantom, for a photon field size of (10×10) cm^2 at isocentre. Configuration with the photoconverter assembly by using 10 cm thick lead. The beam profile is not degraded after the photoconverter: it is still well collimated.

The neutron dose equivalent in depth in phantom

Regarding the neutron dose equivalent measurements, the fast and thermal neutron doses were investigated both in absence of the photoconverter and with the photoconverter with 5 cm and 10 cm thick lead, in front of the phantom and at different depth.
Figure 11.5 shows the ratio between the thermal and fast neutrons dose equivalent for each configuration. In general, more thermal neutrons are produced by using the photoconverter, especially with 10 cm lead thickness at 8 cm depth in phantom.

Moreover, the thermal neutron doses per unit photon dose in each configuration were calculated and represented in Figure 11.6. Neutrons are absorbed going deeper in phantom, and thermal neutrons per photon gain a factor of about 3 between 5 cm and 10 cm thick lead at 3 cm depth, and a factor of about 7 between the configuration without the photoconverter and the photoconverter with 10 cm thick lead. While, at 8 cm depth in phantom, these values increase due to neutron thermalization and absorption in tissue.

By the photon and neutron dose measurements, it emerges that the best photoconverter-moderator assembly is by using a 10 cm thick lead shield. This configuration was so used for the next investigations.

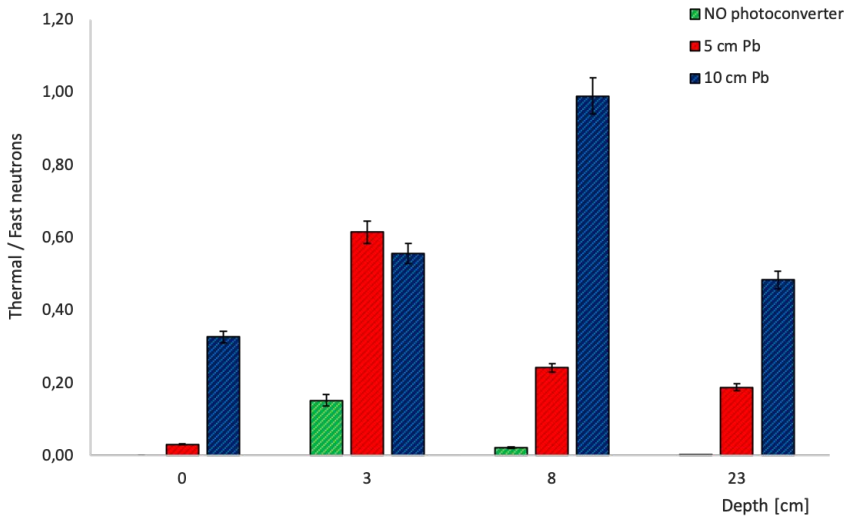

FIGURE 11.5: Ratio between thermal neutron dose equivalent and fast neutron dose equivalent at different depth in phantom. Configuration without and with the photoconverter assembly. In general, more thermal neutrons are present by using the photoconverter assembly, especially at 8 cm depth with 10 cm thick lead.

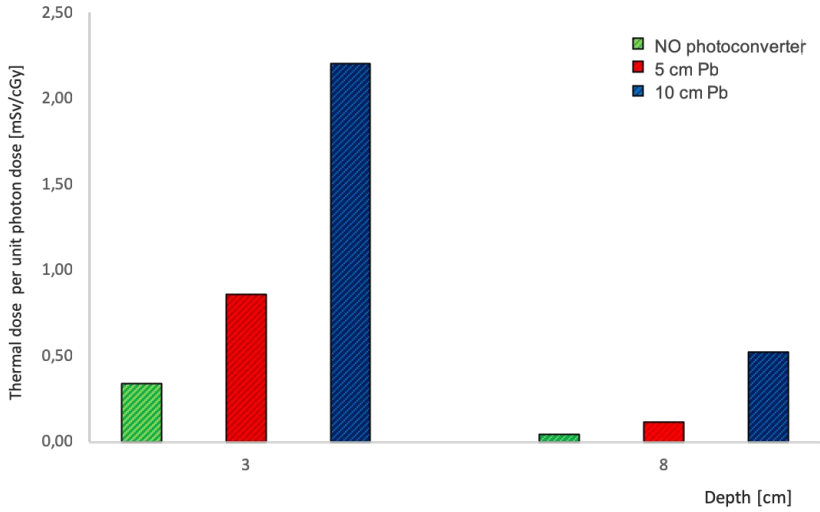

FIGURE 11.6: Thermal neutron dose equivalent per unit photon absorbed dose at 3 cm and 8 cm depth in phantom.

11.2 The angular neutron dose distribution

An angular neutron dose distribution measurements around the photo-converter-moderator was carried out. For this purpose, a suitable structure to allocate upon the photoconverter was designed and assembled.

11.2.1 Materials and Methods

The structure, in alveolar polycarbonate, is made up by several holes at different θ angles suitable to host neutron bubble detectors. The structure can also rotate around the photoconverter along the ϕ direction, making thus possible the angular distribution. Its dimensions perfectly suit the photoconverter geometry.
A 3D sketch of the support is represented in Figure 11.7.
Measurements were carried out by using bubble detectors for fast and thermal neutrons in the same experimental conditions of the previous ones: 15 MV Elekta Synergy Agility LINAC, single-open direct field of (10×10) cm^2 at isocentre, SSD = 90 cm, LINAC gantry = 90°, and by using the photoconverter in the configuration of 10 cm thick lead shield.
The angle (0°, 0°) of the alveolar polycarbonate structure is set in correspondence of the isocentre, at 100 cm from the source, centred with the beam direction axis.

Measurements were performed with and without the photoconverter assembly, comparing the two configurations. Figure 11.8 shows the experimental set-up.

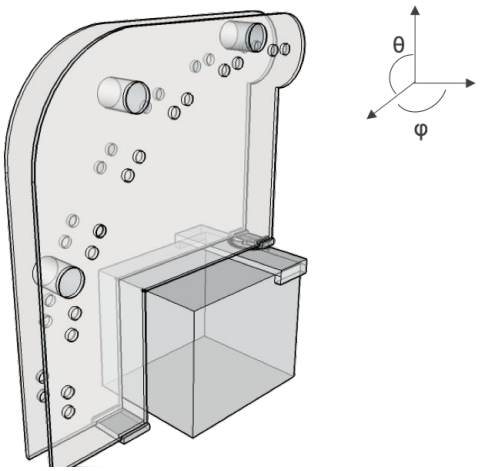

FIGURE 11.7: 3-D representation of the alveolar polycarbonate structure upon the photoconverter. Plot made by means of the open source software *SketchUp* [92], a computer graphics application for 3D modeling. The structure has got a pair of holes every 15°, from 0° to 90° suitable to host two bubble detectors (one for fast and one for thermal neutrons) per each angle.

11.2.2 Results

As usual, results are reported in mSv normalized to 100 MU provided by the LINAC. The typical statistical errors are $\sim$ 5-10% due to bubble counting in the range of 300-100 bubbles per dosimeters, respectively.

Figure 11.9 shows the angular neutron dose equivalent distribution around the photoconverter, at different θ and ϕ angles: 0°, 30°, 60°, 90°, both for thermal and fast neutrons. In general, neutrons are spread out around the photoconverter, without any preferential direction. For this reason, a specific direction was better investigated also without the photoconverter: the fast neutron component was investigated at different θ angles maintaining fixed the ϕ angle at 0° (see Figure 11.10). In the forward direction (0°, 0°), the most relevant one for the therapy, fast neutrons are reduced by over a factor 16; while, in the remaining angles no noticeable differences with respect to the configuration without the photoconverter are observed.

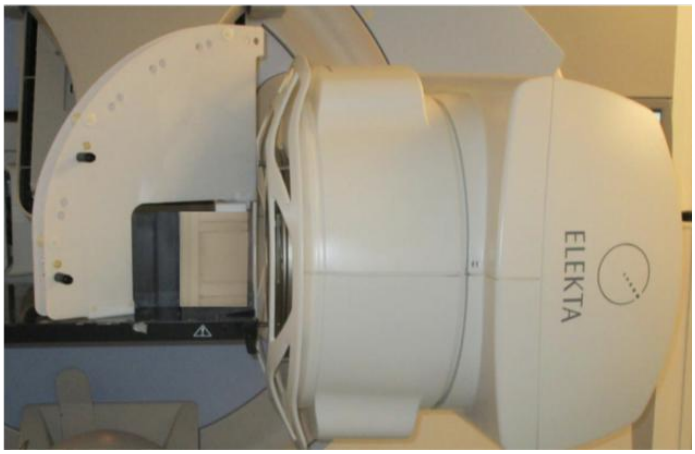

FIGURE 11.8: Experimental set-up for the angular neutron dose distribution. Configuration with the photoconverter assembly with 10 cm thick lead shield. The alveolar polycarbonate structure can rotate around the photoconverter along the ϕ direction, and bubble dosimeters are located in suitable holes at different θ angles. In the picture, the detectors are placed at (0°, 30°) and (30°, 30°).

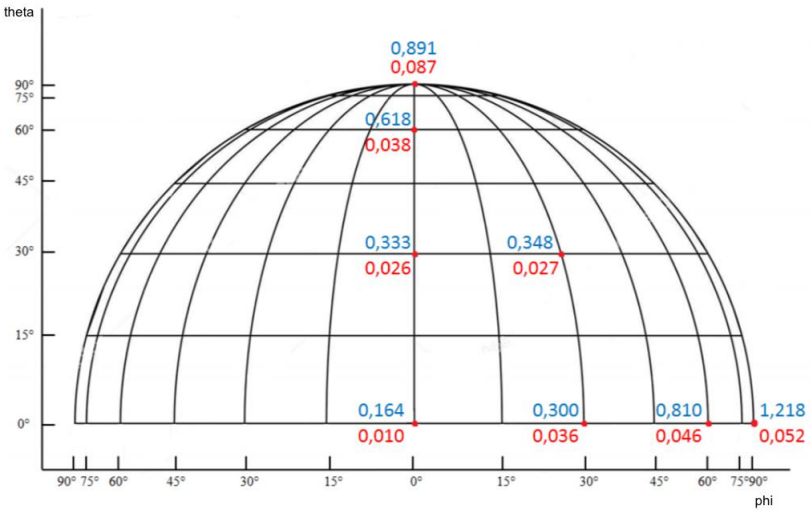

FIGURE 11.9: Graphical representation of the angular neutron doses distribution around the photoconverter. Values are reported in mSv/100 MU. The blue data correspond to the fast neutron dose equivalent measures, while the red ones to the thermal neutrons. In general, neutrons are spread out around the photoconverter, without any preferential direction.

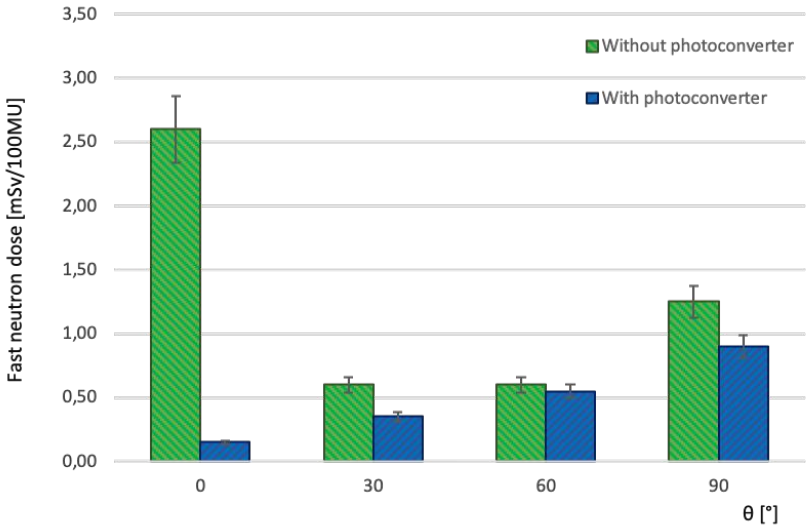

FIGURE 11.10: Fast neutrons dose equivalent angular distribution. Comparison between the configuration with and without the photoconverter assembly at $\phi = 0°$. In the forward direction (0°, 0°) fast neutrons are reduced by over a factor 16; while, in the remaining angles no noticeable differences with respect to the configuration without the photoconverter are observed.

11.3 GEANT4 simulations

Monte Carlo simulations, by using the GEANT4 code (release 10.4), were performed in order to test the toolkit performance in simulating the photoneutron production in medical LINACs.
The 15 MV Elekta Synergy Agility LINAC, the photoconverter with 10 cm thick lead, and the simplified polyethylene phantom were simulated in the set-up conditions previously described (see section 11.1.1).

The physics list used was QGSP-BERT-HP, the recommended one in simulating radiotherapy treatments [109].
A cut in energy was also done to speed up the simulation runs: all photons with energies lower than 7 MeV were cut. This choice was done considering the photonuclear reaction threshold energy on lead and tungsten nuclei.

11.3.1 Simulation of the experimental set-up

This paragraph describes the data entered into the simulation file for characterizing the linear accelerator, the photoconverter and the simplified phantom.

The 15 MV Elekta Synergy Agility LINAC

The included accelerator head components in the simulation file are summarized in Table 11.1, reporting their materials and shapes in an approximative way due to a *non-disclosure agreement* for the Synergy Agility LINAC technical manual. For this reason, components dimensions, their distance from the target, and beam parameters, such as the electron current, the pulse duration, the frequency, etc., could be neither reported.
The origin of the reference system was placed in correspondence of the LINAC target, with the z-axis pointing along the isocenter line.

TABLE 11.1: Summary table of the Elekta Synergy Agility LINAC head components.

Head components	**Approximative materials**	**Approximative shapes**
Target source	Tungsten and Copper	pair of parallelepipeds
Primary collimator	Tungsten	truncated hollow cone
Flattering filter	Copper alloy	inverted cone
Upper secondary collimator	Iron alloy	pair of parallelepipeds
Lower secondary collimator	Iron alloy	pair of parallelepipeds
MLC	Tungsten	set of parallelepipeds
Monitor chamber	Kapton	six cylinders

The photo-converter-moderator

The photoconverter was placed at 61 cm from the LINAC target, following exactly the dimensions, shapes, and materials of the real one (see Figure 11.1).

The simplified phantom

The polyethylene simplified phantom was implemented in the simulation input file at 90 cm from the origin of the reference system (the LINAC target), and the secondary collimators were opened in order to make a 10 cm $\times$ 10 cm square at isocentre, at 10 cm depth in phantom.
The simplified phantom was simulated as a parallelepiped of (30 $\times$ 30 $\times$ 22) cm^3 dimensions, divided in 220 slabs of 1 mm thick each in order to obtain a continuous neutron dose distribution as a function of the depth in phantom.

The total simulated structure (LINAC + photoconverter + phantom) is shown in Figure 11.11

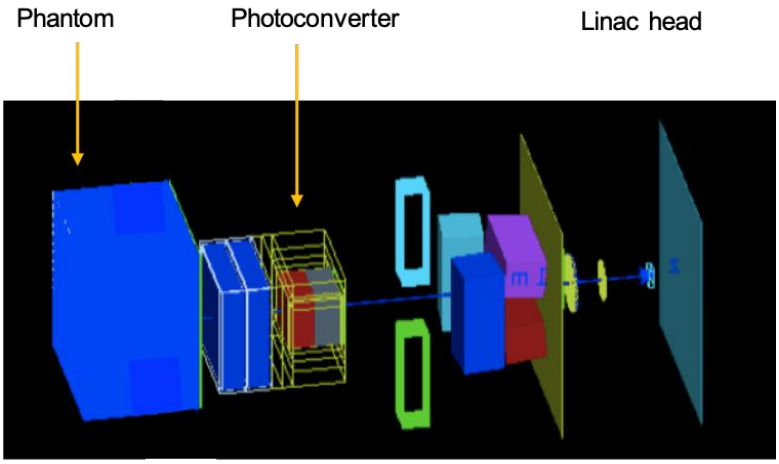

FIGURE 11.11: Simulation plot of the experimental set-up. It's possible to see the linac head, the photoconverter assembly and the simplified parallelepiped phantom.

11.3.2 Results

Results can be summarized as follows:

1. Simulation of the X-ray energy spectrum provided by the LINAC.
2. Simulation of the neutron equivalent dose in depth in tissue (to be compared with experimental results).

1. Simulation of the X-ray energy spectrum

Aiming to validate the simulation code, the first step was studying the photon beam spectrum provided by the LINAC in order to:

- make a qualitative comparison between the simulated 15 MV X-ray spectrum with the ones present in literature;
- calculate the ratio between photons with energies higher, γ_{high}, and lower, γ_{low}, than the cut in energy (to be used to reconstruct the MU provided by the LINAC);
- verify the incident photon beam symmetry.

Several runs were launched. The obtained spectra follow the typical trend of a bremsstrahlung spectrum, providing the first test on the simulation reliability. In Figure 11.12 one of the obtained X-ray spectra is shown.

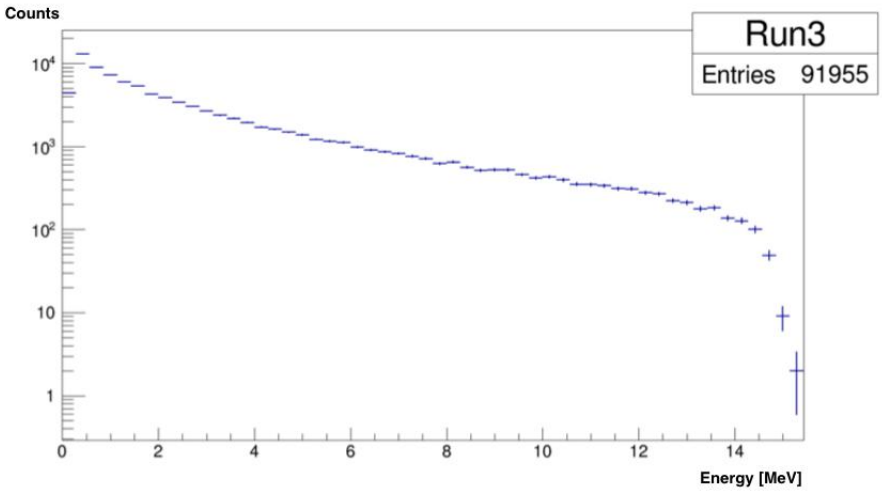

FIGURE 11.12: X-ray energy spectrum provided by the 15 MV Elekta Synergy Agility LINAC. The spectrum shows a maximum energy of 15 MeV and a peak at 0.6 MeV as espected [110].

Starting from the energy spectra, it was possible to calculate the ratio between photons with energies higher than the cut and the total produced photons as:

$$R = \frac{\gamma_{high}}{\gamma_{tot}} \tag{11.1}$$

A weighted mean was done over all the runs, by assuming that the counts follow a Poisson distribution[1]. The resulting R value was 0.113037.

[1] If the number of counts is N, the statistical error on the counts will be $\sqrt{N}$

The incident photon beam symmetry was then evaluated. Figure 11.13 shows the spatial distribution of the photon beam. The symmetry was confirmed: the beam uniformity is within 0.6 σ.

2. Simulation of the neutron dose equivalent in depth in phantom and comparison with experimental results

The neutron fluence in depth in phantom was evaluated both for thermal and fast neutrons. Thanks to fluence-to-dose conversion coefficients trend reported in Figure 10.7 (ICRP 116), it was possible to calculate the neutron dose equivalent.

Aiming to compare simulation results with the experimental ones, the number of generated photons by the simulation have to be converted in MU given experimentally by the accelerator.
Remembering the relationship between monitor units and absorbed dose, 1 MU = 1 cGy[2], and the fluence-to-dose conversion coefficients trend for photons, it was found that

$$1MU = 2 \cdot 10^9 \gamma / cm^2 \tag{11.2}$$

for photon energies of the order of MeV.

The run output gives the number of photons γ_{high}, therefore:

$$\gamma_{tot} / cm^2 = \frac{\gamma_{high} / cm^2}{R} \tag{11.3}$$

Consequently, the total number of monitor units given during a run simulation is:

$$MU_{tot} = \frac{1MU \cdot \gamma_{tot} / cm^2}{2 \cdot 10^9 \gamma / cm^2} \tag{11.4}$$

where γ_{tot} is the total number of simulated photons, R is the ratio between γ_{high} and γ_{tot}, and MU_{tot} are the total simulated monitor units.

Figure 11.14 shows the simulated neutron dose equivalent as a function of depth in tissue for the thermal and fast components, while Figure 11.15 the comparison with experimental data.
A better correspondence between experimental and simulation data is present for the thermal dose with respect to the fast one (σ_{max} = 0.8 and σ_{max} = 2.3, respectively). This is due to the higher statistic available for the thermal component in the simulation: the ratio of the number of neutrons entering in the phantom between thermal neutrons and fast neutrons is 3.01 $\pm$ 0.04 n_{th}/n_{fast}. As wanted, the photoconverter moderates fast neutrons.

[2] at build-up for a field of 10 cm x 10 cm square and SSD= 100 cm

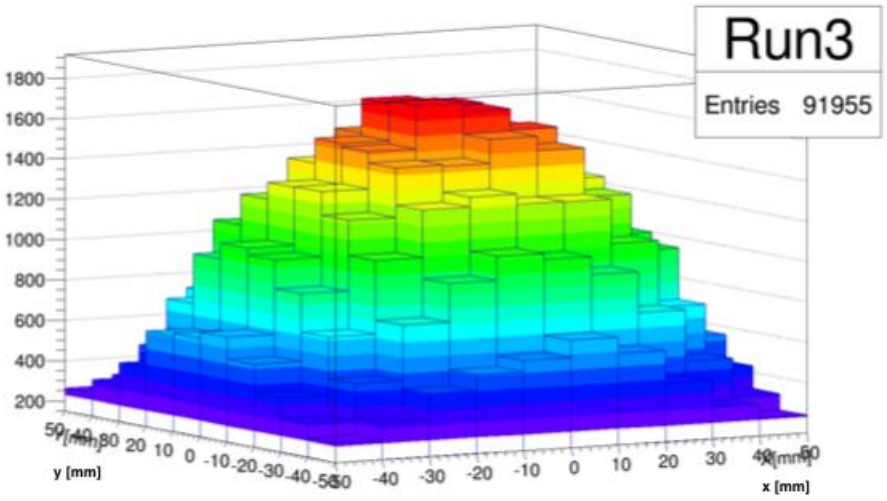

(A) Photon beam spatial distribution. 3D view.

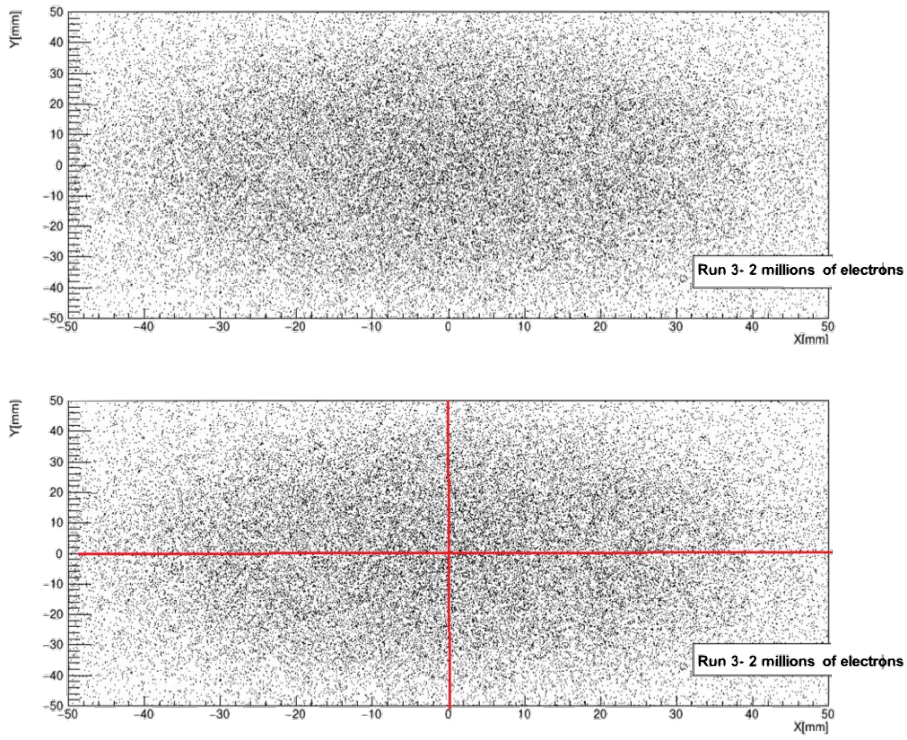

(B) Photon beam spatial distribution. 2D view. To evaluate the beam symmetry, the image was divided in 4 equal regions.

FIGURE 11.13: Spatial distribution of the X-ray beam on the photo-converter lead block. Geant4 calculations. The beam uniformity is within 0.6 σ.

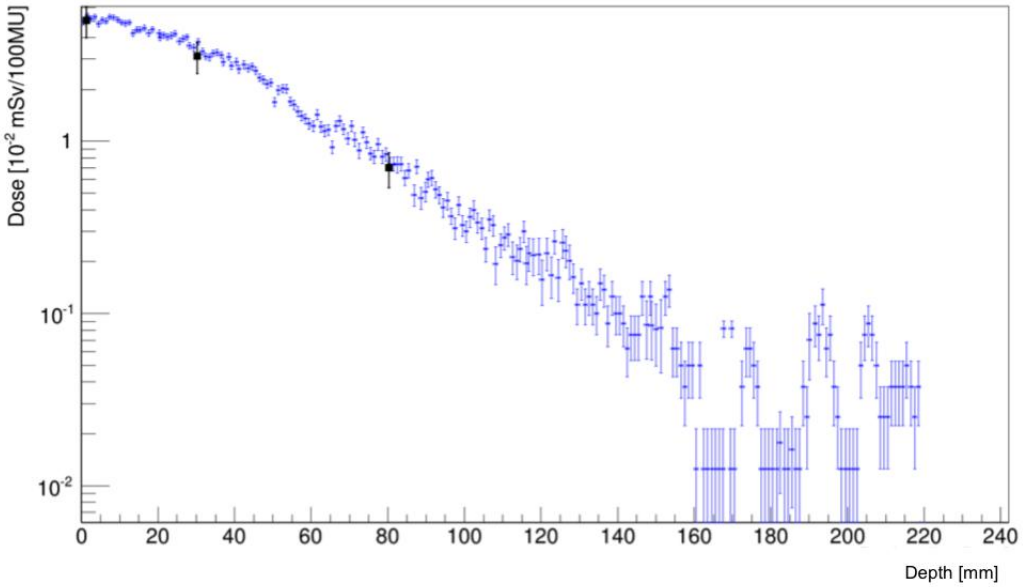

(A) Thermal neutron dose equivalent.

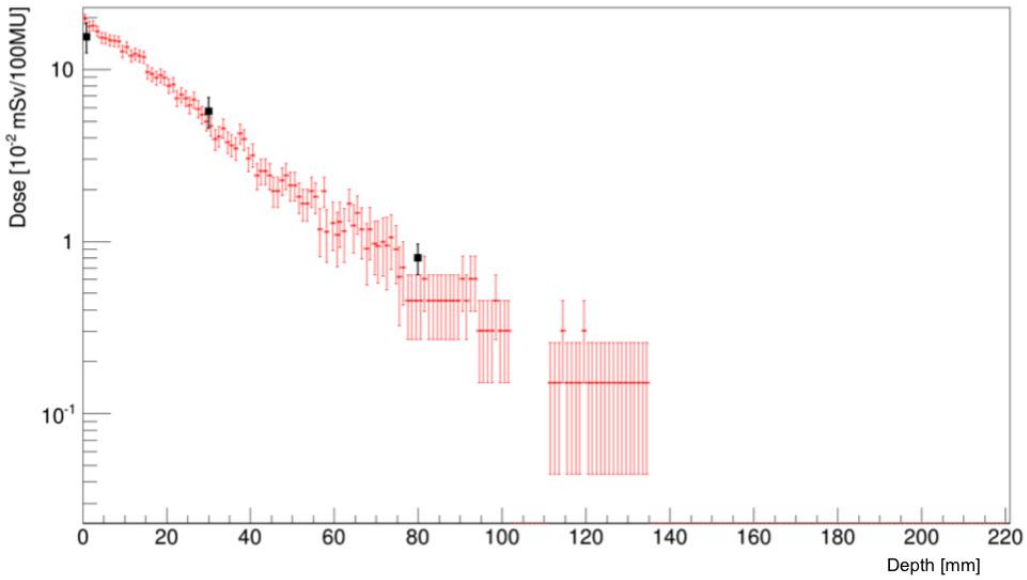

(B) Fast neutron dose equivalent.

FIGURE 11.14: Thermal and Fast neutron dose equivalent in depth in phantom by using the photonconverter assembly. Simulation results. The black dots represents the experimental values.

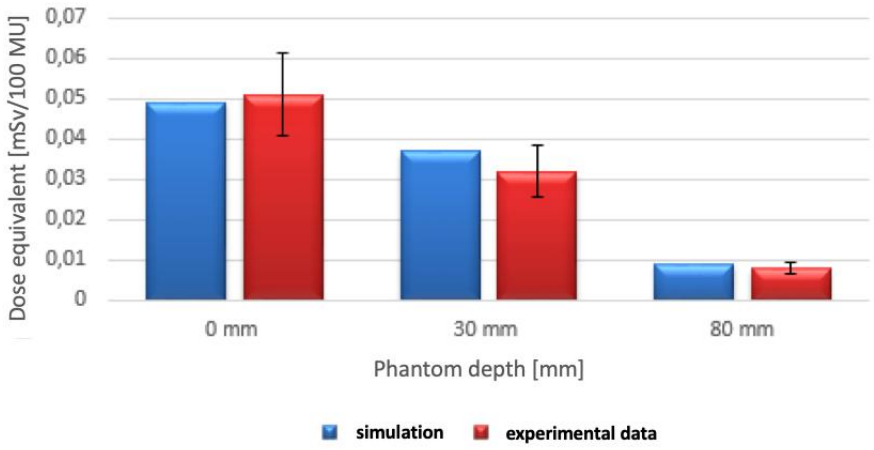

(A) Thermal neutron dose equivalent.

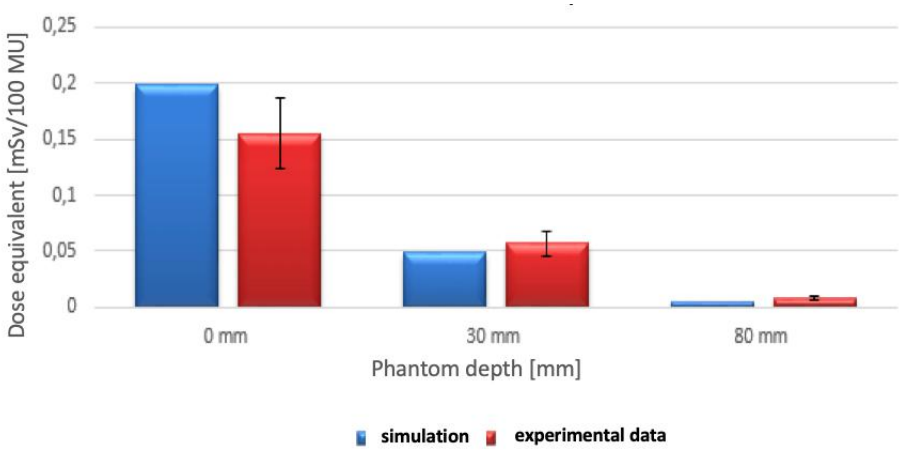

(B) Fast neutron dose equivalent.

FIGURE 11.15: Thermal and fast neutron dose equivalent in depth in tissue, by using the photoconverter assembly. Comparison between experimental and simulation results.

11.4 Summary

A compact photo-converter-moderator assembly [(20 $\times$ 20 $\times$ 24)] cm^3 was developed: it modifies the photon field and increases the neutron photoproduction, absorbing and thermalizing fast neutrons.

Measurements were performed by using the 15 MV Elekta LINAC in photon mode, coupled with the photoconverter and a simplified polyethylene phantom of (30 $\times$ 30 $\times$ 22) cm^3 dimensions. The photon dose and the neutron dose equivalent at different depths in phantom were measured by using radiochromic films and neutron bubble detectors, respectively. Results show that the photon field is modified: a 15 MV photon field produces a dose profile very similar to that would be produced by a 6 MV field in absence of the photoconverter assembly. Moreover, the photon beam profile is not so compromised by the scattering of the photons on lead, the beam is still collimated.
As far as the neutron field is concerned, neutrons are still spread around the photoconverter, without any preferential direction. No appreciable differences with respect to the configuration without the photoconverter are present, except in the direction of the incident photon beam, where fast neutrons are reduced of a factor of 16. Moreover, in phantom measurements show that more thermal neutrons are present by using the photoconverter assembly; thermal neutrons per photon increase of a factor 3 to 12 according to the depth in phantom and to different photoconverter geometries.

GEANT4 simulations were performed to verify the toolkit performance in simulating photoneutron production in medical LINACs, by comparing also the obtained results with the experimental ones. Simulation and experimental data are in agreement: the GEANT4 simulation is completely validated.
Moreover, from the simulation it emerges that a greater amount of thermal neutrons are present after the photoconverter with respect to the fast component ($n_{th}/n_{fast} \simeq 3$).

Chapter 12

Conclusions

This work investigated the possibility of using the parasitic neutron field, produced by high-energy radiotherapy LINACs, to deliver an additional BNCT therapeutic dose to the patient under treatment. The following steps illustrate the idea:

- Patients udergoing radiotherapy with high-energy electron LINACs are exposed to an intense photoneutron field;
- The patient is a very efficient moderator, thus the neutron field in the internal organs and tissues has in important thermal fraction;
- If a tumour seeker boron-10 drug is subministered to the patient, an additional BNCT treatment can be superposed to the conventional radiotherapy;
- This radiosensitization effect could be increased by modifying the treatment field by using a specifically designed neutron photo-converter-moderator assembly.

The idea was investigated experimentally, by using radiochromic films and superheated bubble dosimeters, and with Monte Carlo simulations.

The study consists in three part:

1. Measurements of the parasitic neutron field in organs during single-field radiotherapy with different energies.

   The patient was mimicked by a simplified phantom, suited for dosimetric measurements. For a 10 cm $\times$ 10 cm square photon field at isocentre (at 7 cm depth in phantom) with accelerating potentials 6 MV, 10 MV and 15 MV, the measured neutron dose equivalent in phantom was 0.07 mGy/Gy (neutron dose equivalent / photon absorbed dose at isocentre), 0.99 mGy/Gy and 2.22 mGy/Gy, respectively.

2. Simulation of the potential BNCT dose contribution during single-field radiotherapy.

   For a 10 cm $\times$ 10 cm square photon field at isocentre (at 4 cm depth in phantom) with 18 MV accelerating potential, Monte Carlo simulations quantified the thermal neutron field in the treatment zone in 1.55×10^7 cm^{-2} Gy^{-1}. Assuming a BNCT-standard ^{10}B concentration in tumour tissue, the calculated additional BNCT dose at 4 cm depth in phantom would be 1.5 mGy-eq/Gy. This value depends on the LINAC characteristics and energy, from the collimation system, and from different radiotherapy treatment protocols, reaching 43 mGy-eq/Gy for an IMRT treatment (corresponding to 4% of the 70 Gy photon

dose). The thermal neutron component could thus produce a localized BNCT effect, with a localized dose enhancement, following tumour characteristics.

3. Development of a compact neutron photo-converter-moderator assembly to improve the thermal neutron field in the treatment region without compromising the therapeutic photon field.

   When a specifically designed compact neutron photo-converter-moderator assembly is applied to the LINAC to enhance the thermal neutron field, the photon field is modified. Particularly, a 15 MV photon field produces a dose profile very similar to that would be produced by a 6 MV field in absence of the photo-converter-moderator assembly, without compromising the therapeutic photon beam. As far as the thermal neutron field is concerned, in general more thermal neutrons are present with the photoconverter, and thermal neutrons per photon increase of a factor 3 to12 according to its different geometries and to the depth in phantom. By contrast, the photo-converter-moderator assembly was found to reduce fast neutrons of a factor 16 in the direction of the incident beam.

Although this work is only preliminary, the quantitative estimations suggest that:

- A patient undergoing a radiotherapy treatment is always affected by a parasitic thermal neutron field in the treatment region, of variable intensity depending both on the used collimation techniques and on the performed type of treatment.

- The thermal neutron component could be exploited to produce localized additional therapeutic doses if the ^{10}B-carrier was administered to the patient.

- This radiosensitization effect could be increased by modifying the treatment field by using the specifically designed neutron photo-converter-moderator assembly.

This work is a feasibility study of the possibility to employ the neutron contamination in radiotherapy for the enhancement of the treatment effectiveness, it is not a clinical application. However, the methodology here proposed could be of interest for clinical applications in the future, considering both the ongoing research on newer boron delivery agents, able to be more selective in tumour cell targeting with minimal normal tissue toxicity, and the new trend in radiotherapy consisting of dose escalation and dose hypofractionation.
The next work steps will be:

- to evaluate how the photoconverter assembly changes the total BNCT dose in healthy and tumour tissues, having a higher fraction of thermal neutrons;

- the development of a holder for the photoconverter, to be fixed to the LINAC head, to perform real treatments with multiple fields.

Appendix A

Superheated Drop (Bubble) detectors: Features provided by BTI

In this appendix, graphs provided by the manufacturer BTI about the performance of BD-PND bubble detectors are reported.

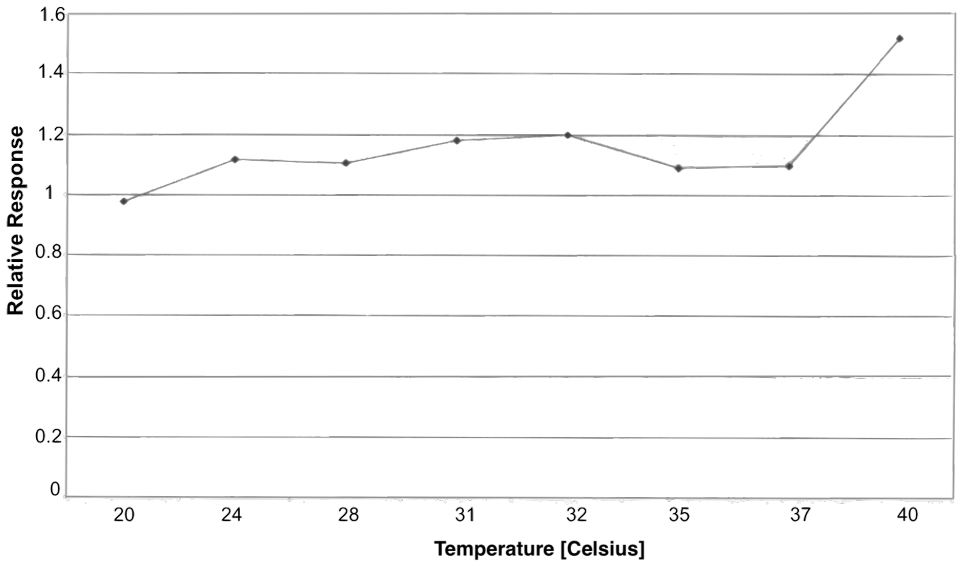

FIGURE A.1: Temperature response of BD-PND dosimeters.

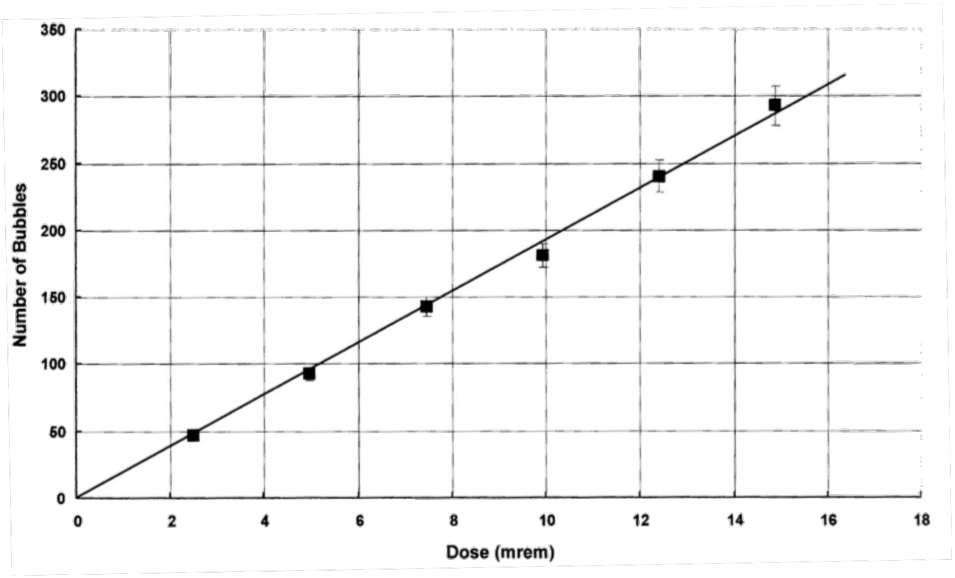

FIGURE A.2: Dynamic range for BD-PND dosimeter - with recompression.

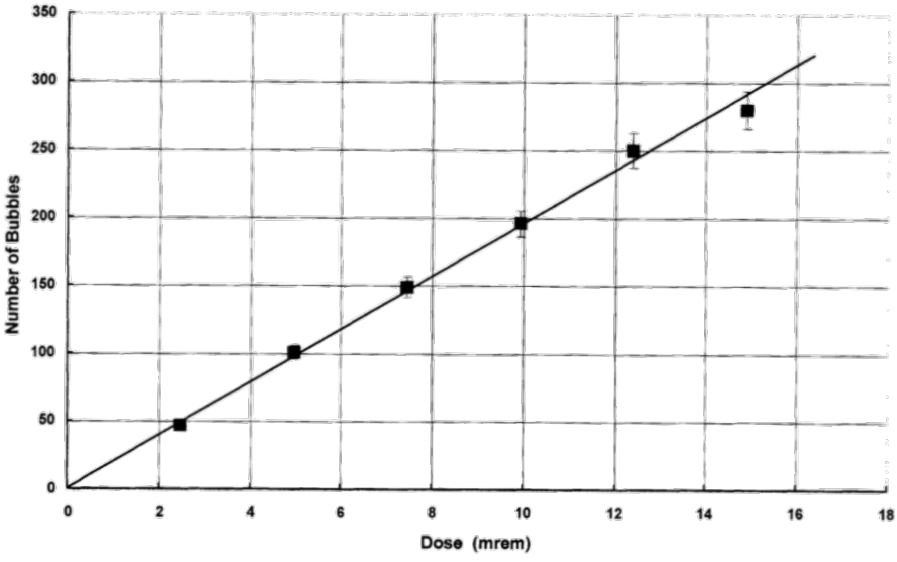

FIGURE A.3: Dynamic range for BD-PND dosimeter - without recompression between measurements.

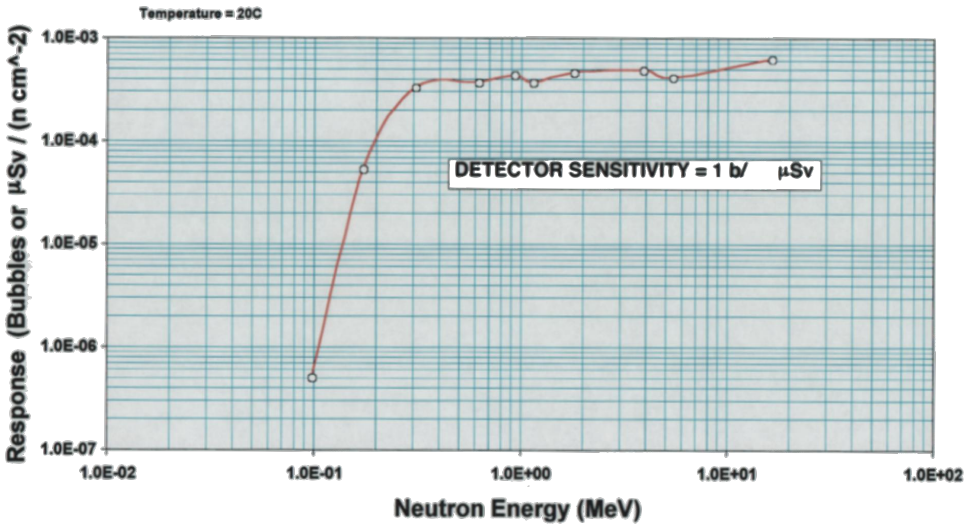

FIGURE A.4: Energy response of BD-PND dosimeters.

Appendix B

New RGB algorithm for dose measurements with EBT3 films tested in 15 MV X-ray beams

Recently submitted in: *Physics and Imaging in Radiation Oncology*
number ID: PHIRO_2018_28

The work investigates the dose-response of EBT3 films in 15 MV X-ray beams up to high-dose levels, 90Gy, with a fit function able to provide more precise dose measurements in the whole range by weighing the three RGB (Red-Green-Blue) color channels together, comparing also results with two different scanners. A consistent dose response was observed, no deviation from the known response curves is shown, only some difference in the recorded pixel values was detected using different scanners. The absorbed dose of unknown films was found to be within 1-1.5% of the true absorbed dose, with a precision of about 2.5%.

Key-words:
Gafchromic EBT3 film; Radiochromic film; Dosimetry; Dose response curve; Calibration function; Scanner dependence

Introduction

Radiochromic films have become an important instrument in medical applications both to verify and to measure two-dimensional dose distributions in external beam radiotherapy, radiosurgery and brachytherapy [1], [2]. The most popular radiochromic films are the Gafchromic EBT films and, at the moment, the third generation of the film (EBT3), released in late 2011, is available for the radiotherapy community. Several studies have been published about the film properties, such as the scanning orientation dependence [3], [4], the energy dependence [5], the film homogeneity [6], and its use in different applications (IMRT [7], stereotactic radiotherapy [8], electron beam therapy [9], *in vivo* dosimetry [10], IORT [11]). However, there is a little information about both the film response to high dose levels and calibration functions usable in an extended dose range. Only few recent works deal with these aspects ([12], [13, [14]), but using greyscale images or not all the three RGB (Red, Green, Blue) color channels together to give the absorbed dose, and/or using a small experimental data set to test the calibration functions. For this reason, this work aims to studying the dose response of Gafchromic EBT3 films in a 6 MV x-ray beam up to very high dose levels, 90 Gy, above the recommended 40 Gy value, with a modified calibration function able to provide more precise dose measurements by weighting

the three RGB scanned image colors together. Moreover, a comparison between two different flatbed scanners was performed.

Materials and Methods

Measurements were carried out exposing the Gafchromic EBT3 dosimetry films to a 15 MV Elekta Synergy Agility LINAC x-ray beam.
The medical LINAC calibration output was carried out by following the International Code of Practice for Dosimetry IAEA TRS398.

Gafchromic EBT3 film

Films used are Gafchromic EBT3, lot #03171501, by Ashland Advance Materials Inc. (Wayne, NJ, USA) [15], and they were handled according to the procedures described in the AAPM TG-55 report [16] and in the user guideline provided by the manufacturer together with the films [17].
The EBT3 is a self-developing film, it doesn't require post-exposure processing, and it can be read with commercial flatbed color scanners. The film is tissue equivalent and water resistant, its dose response ranges from 1 cGy to tens of Gy, and it has got a high spatial resolution (about 25 μm).
The Gafchromic EBT3 dosimetry film is made up of a single active layer, nominally of 27 μm thick, placed between two polyester substrates, 120 μm thick each. This symmetric structure allows to no longer keep track which side is which, eliminating the film face-dependence during scanning.
The active layer contains the active component, stabilizer, marker dye and other additives giving to the film its low energy dependence; while the yellow dye decreases UV/light sensitivity and enables multi-channel dosimetry. The polyester substrate, instead, is coated with silica particles to prevent Newton's ring patterns in the scanned image.

Irradiation Process

In order to investigate the film performance at high dose levels and to obtain a calibration curve, 22 film pieces, each of 4×4 cm^2, were irradiated at different dose values, from 0.5 to 90 Gy. Each film piece was marked on the upper edge in order to know its orientation relative to the original 20×25 cm^2 sheet.
Films were placed in a water equivalent slab phantom (RW3 PTW) of $30\times30\times12$ cm^3 at 1.6 cm depth, in correspondence with the build-up, and irradiated perpendicularly to the radiation beam. The distance from the source to the phantom surface (SSD) was 100 cm and the field size was 30×30 cm^2 at isocenter. The RW3 phantom was centered under the LINAC gantry thanks to its laser alignment system.
The film homogeneity was also investigated as a part of the calibration process, exposing 4 film pieces, each of 4×4 cm^2, in different positions in the radiation field prior to irradiation in the same conditions above described.

Readout Process

The exposed films were read two days after the irradiation, to allow the stabilization of changes in all the color channels [18], by means of two different commercial flatbed color scanners: the Epson 1680Pro (Scanner A), with a scan window of 22×31 cm^2 (A4 paper size), and the Epson Expression 10000XL (Scanner B), with a scan window of 31×44 cm^2 (A3 paper size).

Each film piece was read three times with both scanners on the same day, to ensure the identical condition of temperature and humidity, minimizing the scanner variability.
The readout process was made according to the manufacturer's scan guideline [17], placing the films into the center of the scan area in landscape orientation (a frame was used to fix the film in a reproducible way), keeping consistent position and orientation in each scan to avoid the lateral scan effect.
RGB-positive images were collected in 48-bit, measuring the red, green and blue color components of the light transmitted by the film at a color depth of 16-bit per channel with a spatial resolution of 72 dpi, in transmission mode with no color correction. All the scanner parameters have been kept fixed during all the film acquisitions.

Analysis Process

The digitized images were saved in tagged image file format (TIFF) and analyzed by means of the software *ImageJ 1.50i* [19], by splitting the film image data into red, green and blue color channels. For each scanned image and color channel, a small region of interest (ROI) at the field centre was selected to obtain the mean pixel value V and its standard deviation σ. Knowing these values and the absorbed dose D by each film, the dose response curves per each color channel were plotted and analyzed with the software *ROOT* [20].
Four different conditions have been taken into account:

- Films read with the Scanner A, in the recommended dose range 0-40 Gy
- Films read with the Scanner A, in the extended dose range 0-90 Gy
- Films read with the Scanner B, in the recommended dose range 0-40 Gy
- Films read with the Scanner B, in the extended dose range 0-90 Gy

The suggested function to fit the dose response curve of the EBT3 film [21] has been empirically modified, providing more precise dose measurements. The modified calibration function is represented by:

$$V(D) = \frac{W_0 + W_1(D/c)}{1 + (D/c)} \tag{B.1}$$

where $V(D)$ is the pixel value as a function of the absorbed dose D, and $W0, W1, c$ are the equation parameters to be fitted that depend on the considered color channel. Moreover, W_0 is the pixel value corresponding to D tending to zero (linked, thus, to the unirradiated film); W_1 is the pixel value corresponding to D tending to infinite (linked to the maximum film dimming); while the parameter c represents the dose at which the pixel value is half way between W_0 and W_1, $[(W0 + W1)/2]$.

The rational formula B.1 be inverted for each of the three RGB colors to provide three absorbed dose values Dx of an unknown film starting from the film dimming V, with their associated propagated uncertainty:

$$D_x = c \cdot \frac{W_0 - V}{V - W_1} \tag{B.2}$$

This last expression can be used to give a final more precise dose value in the whole range, by weighting the three RGB scanned image colors together:

$$D_f = \sum_x \frac{D_x/\sigma_{x^2}}{1/\sigma_{x^2}} \tag{B.3}$$

with its standard deviation:

$$D_f = \sqrt{\sum_x \frac{1}{1/x^2}} \tag{B.4}$$

Results

For each of the four conditions taken into account, the dose response curves per each color channel were plotted and fitted with the equation B.1, by means of *ROOT*.
Results are shown in Figure B.1. The flattest curve is linked to the blue channel, the curve with a steep slope at low doses corresponds to the red channel, while the curve with a reasonable good response at low, medium, and high doses corresponds to the green channel.
Once the calibration has been carried out and the fitting parameters W0, W1 and c, have been evaluated in each condition, the equation B.2 was used to give the three RGB absorbed dose values D_x. Then, by taking the weighted mean of the three RGB colors together, the final absorbed dose value D_f was calculated with the equation B.3, giving the absorbed dose of an unknown film. Finally, residuals have been evaluated by calculating the ratio between the calculated absorbed doses and the original absorbed doses D.
Both the D_f values and residuals as a function of the original absorbed dose D are reported in Figure B.2 , for the extended dose range 0-90 Gy and for the Scanner B. Comparable results have been obtained for the Scanner A: for this reason, results were reported in the text but not shown in graphical representations.

Discussion

As far as the film homogeneity check is concerned, the deviation in all color channels was less than 1%: no evidence was so found for films inhomogeneity.
Looking at Figure B.1, the estimated fit parameters for the two dose ranges (0-40 Gy and 0-90 Gy) are in agreement within 2σ, except for the parameter W_1 in the green and blue channels in the Scanner A and Scanner B, respectively, within 3σ. Since W_1 is linked to the maximum film dimming, the value obtained for the extended dose range is considered nearer to the true one, and thus the correct value to be taken into account.
The simple parametric dependence has allowed to estimate the dose response error: relative errors range 0.4-0.8% for the green and red channels, and 1.0-2.8% for the blue one. This is due to the blue curve general flatness, giving a higher error value; while the slope of the other two curves is still pronounced around c, providing smaller errors.
The modified calibration function fits well in the whole dose range: it's so usable both in the recommended dose range values and at higher ones. A consistent dose response was thus observed in EBT3 films, no deviation from the typical response curves is shown [17].
However, some difference in the recorded pixel values was detected by using two different flatbed scanners, mostly in the blue channel, despite films were positioned

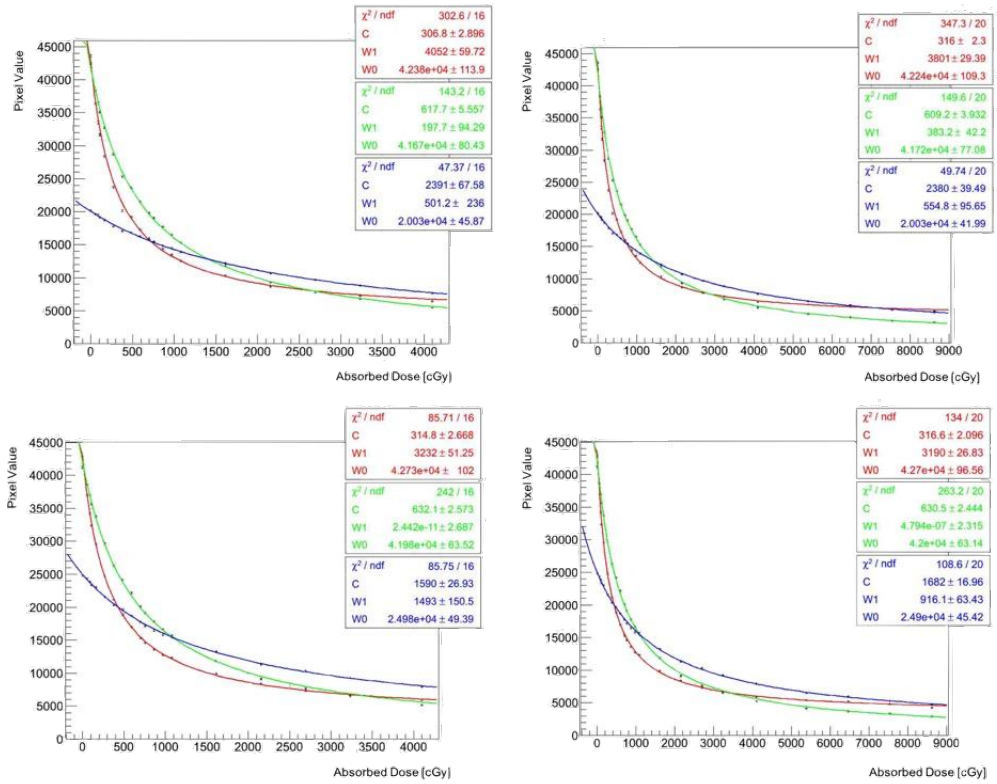

FIGURE B.1: EBT3 DOSE RESPONSE CURVE
for the Epson 1680Pro - Scanner A (upper graphs) and the Epson Expression 10000XL - Scanner B (bottom graphs).
Images on the left show the film response per each RGB color channel in the recommended dose range 0-4000 cGy, while the right ones for the extended dose range, up to 9000 cGy. In the upper right side of both images, the estimated fit parameters W0, W1, c and the reduced chi-square 2 values are reported for each of the three color channels. The upper box shows results for the red channel, the middle one for the green channel, and the last box for the blue channel.

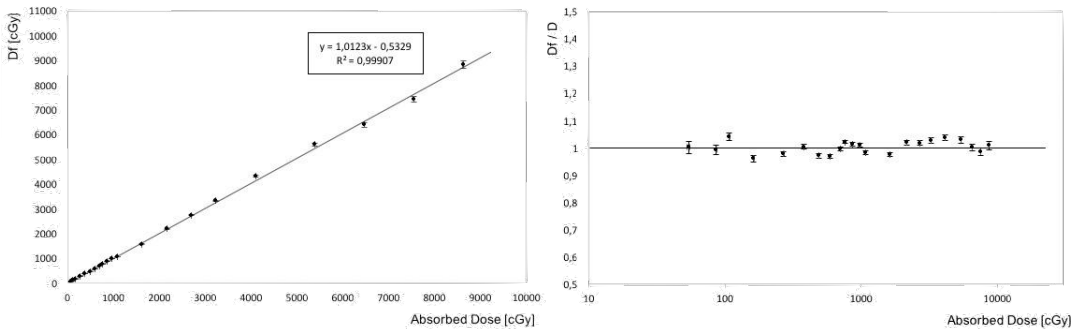

FIGURE B.2: Calculated weighted absorbed dose D_f (on the left) and residuals for the weighted RGB absorbed dose D_f (on the right in logarithm scale in the x axes) as a function of the true absorbed dose D. Films irradiated in the extended dose range 0-9000 cGy, and read with the Epson Expression 10000XL flatbed scanner (Scanner B).

in exactly the same way. The different responses have to be related to the dissimilar light source and sensor system of the scanners. It is known that Gafchromic film is a polarizer, like the mirror system in the scanner, and both influence the same light ray before it reaches the CCD sensor: the Scanner A and the Scanner B have different dimensions (width and height), thus differences in the angle of incidence on the mirrors can be expected between the scanners, introducing an off-set in the calibration curve. This problem has been largely discussed in a recent work [22], and here confirmed.

Regarding results obtained for the inverse of the calibration function, the graph on the left in Figure B.2 shows the linearity of the calculated absorbed doses D_f versus the real ones for the Scanner B. The reduced chi-square value is 1.40: with 20 degrees-of-freedom and a p-value equal to 0.05, the null hypothesis can be accepted. Comparable results have been obtained for the Scanner A, where the chi-square value is 1.42.
Moreover, looking at residuals in the graph on the right in Figure B.2, data are well arranged around the reference value 1 by weighting the three RGB colors together, and both relative errors and the chi-square value are lower than those found considering channels separately. Also in this case, analogous results have been obtained analyzing data for the Scanner A.
Starting from the dispersion of residuals it was possible to calculate the film precision: it was noted that precision level of 2-4% has to be achieved in film dosimetry [14, 23]. In this work the reached precision level is 2.5%, slightly better than the reported 2.6% for a 6MV photon beam [24] and much better than the 3.7% reached in other works for the same beam energy [14].

From this work it emerges that the calibration function fits well in the whole dose range, and its inverse function can be used to give the absorbed dose D_f of an unknown film, within the 1.5% and the 1% accuracy with respect to the true absorbed dose D for the Scanner A and Scanner B, respectively, by weighting all the three color channels together.
Notice that other works, such as the recent one by Ref. [12], propose alternative calibration functions, but often using more complicated expressions not easily to be handled, inverted and/or suitable for a large dose range like the one here discussed.

Acknowledgements

Authors thank the radiotherapy ward staff of the Maggiore Hospital in Trieste for making available all the necessary equipment to carry out the work.

References

[1] Butson MJ, Yu PKN, Cheung T, Metcalfe P. Radiochromic film for medical radiation dosimetry. Master Sci Eng 2003; 41:61-120. [2] Karellas A, Thomadsen BR. Radiochromic film: Role and applications in radiation dosimetry. 1st ed. CRC press: Indra J Das; 2017. [3] Saurs S, Frengen J. Gafchromic EBT film dosimetry with flatbed CCD scanner: a novel background correction method and full dose uncertainty analysis. Med Phys 2008; 35(7):3094-101. [4] Andres C, Del Castillo A, Tortosa R, Alonso D, Barquero R. Potential errors in optional density measurements due to scanning side in EBT and EBT2 Gafchromic film dosimetry. Med Phys 2010; 37(4):6271-78. [5] Massillon G-JL, Chiu-Tsao ST, Domingo-Munoz I, Chan MF. Energy dependence of the new Gafchromic EBT3 film: Dose response curves for 50 KV, 6 and 15 MV x-ray beams. [6] Mizuno H, Sumida I, Tanaka A, Ogawa K. Comparing homogeneity between Gafchromic film EBT2 and EBT3. 2014; J Med Phys 41(6):239. [7] Casanova Borca V, Pasquino M, Russo G, Grosso P, Cante D, Sciacero P, et al. Dosimetric characterization and use of Gafchronic EBT3 film for IMRT dose verification. J Appl Clin Med Phys 2013; 14(2):158-71. [8] Cusumano D, Fumagalli ML, Marchetti M, Farisellu L, De Martin E. Dosimetric verification of stereotactic radiosurgery/stereotactic radiotherapy dose distributions using gafchromic EBT3. Med Dosim 2015; 40(3):226-31. [9] Ulya S, Wibowo WE, Nuruddin N, Pawiro Sa. Dosimetric characteristics of gafchromic EBT3 film on small field electron beam. J Phys Conf Ser (2017); 851:012023. [10] Moylan R, Aland T, Kaim T. Dosimetric accuracy of Gafchromic Ebt2 and Ebt3 film dor in vivo dosimetry. Australas Phys eng Sci Med (2013); 36(3):331-7. [11] Severgnini M, De Denaro M, Bortul M, Vidali C, Beorchia A. In vivo dosimetry and shielding disk alignment verification by EBT3 GAFCHROMIC film in breast IOERTtreatment. J Appl Clin Med Phys 2015; 16(1):112-20. [12] Campajola L. Casolaro P, Di Capua F. Absolute dose calibration of EBT3 Gafchromic films. J Inst, 2017; 12(08):1-10 [13] Yao T, Huthjens LH, Gasparini A,Warman JM. A study of four radiochromic films currently used for (2D) radiation dosimetry. Rad Phys Chem 2017; 133:37-44. [14] Sipila P, Ojala J, Kaijaluoto S, Jokelainen I, Kosunen A. Gafchromic EBT3 film dosimetry in electron beams: Energy dependence and improved film read-out. J Appl Clin Med Phys 2016; 17(1):360-373. [15] Ashland. Gafchromic radiotherapy film, 2017. [16] Recommendations of AAPM Radiation Therapy Committee Task Group No.55. Radiochromic Film Dosimetry. AAPM report No. 63. Med Phys, 1998; 25(11):2093-115. [17] Ashland. Gafchromic EBT3: Scan handling guide. P/N AM0191, 3/12, Rev 0. [18] Devic S, Tomic N, Lewis D. Reference radiochromic film dosimetry: Review of techical aspects. Phys Med 2016; 32:541-56. [19] National istitutes of Health, Image J. Image processing and analysis in Java, 2004. [20] CERN. ROOT: Data analysis framework. [21] Ashland. Gafchromic: Dosimetry media, type EBT-3. [22] Van Battum LJ, Huizenga H, Verdaasdonk RMV, Heukelom S. How flatbed scanners upset accurate film dosimetry. Phys Med Biol 2016, 61(2):625-49. [23]Dreindl R, Georg D, Stock m. Radiochromic film dosimetry: Considerations on precision and accuracy for EBT2 and EBT3 type films. Z Med Phys 2014; 24(2):153-63. [24]Farah N, Francis Z, Abboud M. Analysis of the EBT3 Gafchromich film irradiated with 6MV photos and 6 MeV electrons usign reflective mode scanners. Phys Med Biol 2014; 30(6).708-12.

Appendix C

MCNP: Variance reduction techniques

A lot of variance reduction techniques are available in the MCNP code. They reduce the needed machine time to get statistically significant results, improving thus the accuracy and efficiency.

The efficiency of a Monte Carlo calculus depends both on the kind of the wanted result and on the random walk histories of particles. When a result is requested, for example a flux in a tally, the code provides a number coming from the reproduction of a series of particles that statistically give rise to the correct density of N particles at that point, $N(\vec{r}, v, t)$.
Several methods are present to statistically reproduce a correct particle density: the *analog* and *no-analog* techniques. The analog techniques reproduce simply the events according to their natural probability to occur, by estimating the number of physical particles that walk a certain path. The no-analog techniques, instead, do not directly simulate the nature of a particle: the statistical properties of a process can be modified, and the particle can walk any histories, as long as the correct particle density $N(\vec{r}, v, t)$ is, at the end, calculated. This can be obtained by modifying the statistical weight of each particle and histories simulated. The statistical weight can be thought as the number of physical particles corresponding to the simulated particle; therefore, the correspondence with the nature of a particle can be recovered by acting on the particle weight, lost altering the sampling process.
Summarizing, the estimated relative error accompanying any tally result is proportional to $1/\sqrt{N}$, where N is the number of particle histories, which is proportional to the computer time T. Since it is often impossible to improve the simulation precision by increasing the number of histories, other strategies like the tally choices and/or the sampling choices are employed.

The main techniques to reduce the computer time can be divided into four classes, meshing more non-analog techniques together:

1. **Truncation methods**. They speed up calculation by truncating parts of phase space do not contribute significantly to the solution, e.g., the energy cut-off and time cut-off.

2. **Population control methods**. They use particle splitting and Russian roulette to control the number of samples taken in various regions of phase space. In important regions, many samples of low weight are tracked; while, in unimportant regions, few samples of high weight are tracked. A weight adjustment is thus made to ensure that the problem solution remains unbiased.

3. **Modified sampling methods**. They alter the statistical sampling of a problem by increasing the number of tallies per particle. For any Monte Carlo event, it is possible to sample by any arbitrary distribution rather than by the physical probability, as long as the particle weights are adjusted to compensate. For example, sampling can be done by distributions that send particles in desired directions or into other desired regions of phase space, such as time or energy, or force a desired type of collisions.

4. **Partially deterministic methods**. They do not use the normal random walk process but apply deterministic-like techniques, such as the next event estimators used for point detectors.

Bibliography

[1] Stupp R. and et al. "Effects of radiotherapy with concomitant and adjuvant temozolomide versus radiotherapy alone on survival in glioblastoma in a randomised phase iii study: 5-year analysis of the eortc-ncic trial." In: *The Lancet Oncology* 10 (2009), pp. 459–466.

[2] Wardman P. "Chemical radiosensitizers for use in radiotherapy". In: *Clinical Oncology* 19.6 (2007), pp. 397–417.

[3] Barth R.F. "A critical assessment of Boron Neutron Capture Therapy: An overview". In: *Journal of Neuro-Oncology* 62.1 (2003), pp. 1–5.

[4] Chadwick M.B. et al. "ENDF/B-VII.0: Next Generation Evaluated Nuclear Data Library for Nuclear Science and Technology". In: *Nuclear Data Sheet Data Sheets* 107 (2006), pp. 2931–3060.

[5] Coderre J.A. and Morris G.M. "The Radiation Biology of Boron Neutron Capture Therapy". In: *Radiation Research* 151.1 (1999), pp. 1–18.

[6] Eaton B.R. and et al. "Secondary malignancy risk following proton radiation therapy". In: *Frontiers in Oncology* 5.261 (2015).

[7] Zanini A. and et al. "Monte Carlo simulation of the photoneutron field in linac radiotherapy treatments with different collimation systems." In: *Physics in Medicine and Biology* 49.4 (2004), pp. 571–582.

[8] Zanini A. and et al. "Patient plane and in tissue neutron spectra in photon radiotherapy treatments by Linacs." In: *Proceedings of the Workshop on Neutron Spectrometry and Dosimetry: Experimental Techniques and MC calculations, Stockholm, 18-20 October 2001.* Ed. by Otto editore. 2004, pp. 225–235.

[9] Bocker W. et al. *Pathologie*. Ed. by Elsevier GmbH. 5th edition. Urban und Fisher Verlag, 2012.

[10] Tomasetti C. and Vogelstein B. "Variation in cancer risk among tissues can be explained by the number of stem cell divisions". In: *Science* 347.6217 (2015), pp. 78–81.

[11] Owen D. Holder D. Alonso J. and Mackay R. "Technologies for delivery of proton and ion beams for radiotherapy." In: *International Journal of Modern Physics* 29.14 (2014).

[12] *The European Network for Light ion Hadron Therapy*. URL: https://enlight.web.cern.ch/what-is-hadron-therapy.

[13] Alberts B. Johnson A. Lewis J. Raff M. Roberts K. and Walter P. *Molecular biology of the cell*. 5th edition. Garland Science, 2008.

[14] Hall E.H. and Giaccia A.J. *Radiobiology for the Radiologyst*. 7th edition. Lippicott Williams and Wilkins, 2012.

[15] Lodish H. Berk A. Kaiser C.A. Krieger M. Scott M.P. and Bretscher A. *Molecular cell biology*. 6th edition. DeGruyter, 2007.

[16] Milo R. and Phillips R. *Cell biology by the numbers*. Garland Science, 2016.

[17] Lomax M.E. Folkes L.K. O'Neill P. "Biological consequences of radiation-induced DNA damage". In: *Clinical Oncology* 25.10 (2013), pp. 578–585.

[18] Hanahan D. and Weinberg R.A. "Hallmarks of cancer: The next generation". In: *Cell* 144 (2011), pp. 646–674.

[19] International Commission on Radiation Units and Measurements. *ICRU Report 85: Fundamental Quantities and Units for Ionizing Radiation (revised)*. Vol. 11. 1. Journal of the ICRU, 2011.

[20] International Commission on Radiation Units. *ICRU Report 16: Linear Energy Transfer*. 1970.

[21] Ray K.J. Sibson N.R. and Kiltie A.E. "Treatment of Breast and Prostate Cancer by Hypofractionated Radiotherapy: Potential Risks and Benefits". In: *Clinical Oncology* 27.7 (2015), pp. 420–426.

[22] International Commission on Radiological Protection. *ICRP Publication 103: The 2007 Recommendations of the International Commission on Radiological Protection*. Vol. 37. 2-4. Annals ICRP, 2007.

[23] United Nations Scietific Committee on the Effects of Atomic Radiation. *Sources, effects and risks of ionizing radiation*. UNSCEAR 2012, 2015.

[24] Bentzen S.M. and et al. "Quantitative Analyses of Normal Tissue Effects in the Clinic (QUANTEC): An introduction to the scientific issues". In: *International Journal of Radiation Oncology Biology Physics* 76.3 (2010), S3–S9.

[25] Weber W. and Zanzonico P. "The Controversial Linear No-Threshold Model". In: *The Journal of Nuclear Medicine* 58.1 (2017), pp. 7–8.

[26] Brenner D.J. and et al. "Cancer risks attributable to low doses of ionizing radiation: Assessing what we really know." In: *Proceedings of the National Academy of Sciences of the United States of America* 100.24 (2003), pp. 13761–13766.

[27] *The 1990 Recommendations of the International Commission on Radiological Protection*. Vol. 21. 1-3. ICRP Publication 60, 1991.

[28] Si-Young Chang. "Definition and Difference between Dose Equivalent and Equivalent Dose in Radiation Dose Measurement and Evaluation". In: *Journal of Radiation Protection and Research* 18.1 (1993).

[29] Sanchez-Doblado F. Domingo C. Gomez F. Sanchez-Nieto B. Bedogni R. and et al. "Estimation of neutron-equivalent dose in organs of patients undergoing radiotherapy by the use of a novel online digital detector". In: *Physics in Medicine and Biology* 57 (2012), pp. 6167–6191.

[30] Metcalfe P. Kron T. and Hoban P. *The physics of radiotherapy X-rays and electrons*. Medical Physics Publishing, Madison, Wisconsin (USA), 2007.

[31] Van Dyk J. *The Modern Technology of Radiation Oncology: A Compendium for Medical Physicists and Radiation Oncologists*. Ed. by Jacob Van Dyk. Medical Physics Publishing, Madison, Wisconsin (USA), 1999.

[32] Severgnini M. *Physics of Radiation Oncology 1: Dosimetric Properties of Clinical Beams*. PhD course.

[33] Knoll G.F. *Radiation Detection and Measurement*. 4th. WILEY, 2010.

[34] Lawrence Berkeley National Laboratory. *X-ray Data Booklet*.

[35] I. Akkurt and et al. "Photoneutron Yields from Tungsten in the Energy range of the GDR". In: *Physics in Medicine and Biology* 48 (2003), pp. 3345–52.

[36] Levinger J.S. and Bethe H.A. "Dipole transition in nuclear photo effect." In: *Physical Review* 78 (1950), p. 115.

[37] Ongaro C. and et al. "Analysis of photoneutron spectra produced in medical accelerators." In: *Physics in Medicine and Biology* 46.3 (2001), p. 897.

[38] Brown D.A. and et al. "ENDF/B-VIII.0: The 8th Major Release of the Nuclear Reaction Data Library with CIELO-project Cross Sections, New Standards and Thermal Scattering Data". In: *Nuclear Data Sheets* 148 (2018), pp. 1–142.

[39] Burn K.W. and Ongaro C. "Photoneutron production and dose evaluation in medical accelerators". In: *ENEA report RT/2002/51/FIS* ().

[40] International Commission on Radiological Protection, ed. *Conversion coefficients for radiological protection quantities for external radiation exposures.* ICRP Publication 116, 2010.

[41] NCRP Report No. 38, ed. *Protection against neutron radiation*. National Council on Radiation Protection and Measurements, 1971.

[42] Kry S.F. and et al. "AAPM TG 158: Measurement and calculation of doses outside the treated volume from external-beam radiation therapy". In: *Medical Physics* 44.10 (2017), pp. 391–429.

[43] NCRP Report No. 79, ed. *Neutron Contamination from Medical Electron Accelerators*. National Council on Radiation Protection and Measurements, 1984.

[44] Wilenzick R.M. Oliver Jr G.D. De Almeida C. and Almond P.R. "Fast neutron contamination from the 25 MV X-ray beam of a clinical linear accelerator". In: *Physics in Medicine and Biology* 17.6 (1972).

[45] Vanhavere F. Huyskens D. and Struelens L. "Peripheral neutron and gamma doses in radiotherapy with a 18 MV linear accelerator." In: *Radiation Protection Dosimetry* 110 (2004), pp. 607–612.

[46] Awotwi-Pratt J.B. and Spyrou N.M. "Measurement of photoneutrons in the output of 15 MV Varian Clinac 2100C LINAC using bubble detectors." In: *Journal of Radioanalytical and Nuclear Chemistry* 271 (2007), pp. 679–684.

[47] Alikaniotis K. and et al. "Measurements of the parasitic neutron dose at organs from medical LINACs at different energies by using bubble detectors". In: *Radiation Protection Dosimetry* (2018), DOI: 10.1093/rpd/ncx308.

[48] Locher GL. "Biological effects and therapeutic possibilities of neutrons". In: *Am J Roentgenol Radiat Therap* 36 (1936), pp. 1–13.

[49] Barth R.F. Coderre J.A. Vicente M.G.H. and Blue T.E. "Boron neutron capture therapy of cancer: Current status and future prospects". In: *Clinical Cancer Research* 11.11 (2005), pp. 3987–4002.

[50] Hawthorne M. F. and Lee M.W. "A critical assessment of boron neutron capture therapy: an overview". In: *Journal of Neuro-Oncology* 62 (2003), pp. 1–5.

[51] Bortolussi S. and et al. "Boron uptake measurements in a rat model for Boron Neutron Capture Therapy of lung tumours". In: *Applied Radiation and Isotopes* 69.2 (2011), pp. 394–398.

[52] Coderre J.A. and Morris G.M. "The radiation biology of boron neutron capture therapy". In: *Radiation Research* 151.1 (1999), pp. 1–18.

[53] Barth R.F. Mi P. and Yang W. "Boron delivery agents for neutron capture therapy of cancer". In: *Cancer Communications* 38 (2018), p. 35.

[54] Soloway A.H. Tjarks W. Barnum B.A. Rong F.G. Barth R.F. Codogni I.M. and Wilson J.G. "The chemistry of neutron capture therapy". In: *Chemical Reviews* 98 (1998), pp. 1515–1562.

[55] Coderre J.A. and et al. "Derivation of relative biological effectiveness for high-LET radiations produced during boron neutron capture iraadiation of the rat gliosarcoma in vitro and in vivo". In: *Radiat Oncol Biol Phys* 27 (1993), pp. 1121–1129.

[56] Bart R.F. and et al. "Boron neutron capture therapy of brain tumors: an emerging therapeutic modality". In: *Neurosurgery* 44.433-451 (1999).

[57] Raaijmakers C.P. and at al. "Clinical dosimetry of an epithermal neutron beam for neutron capture therapy: dose distributions under reference conditions". In: *Int J Radiat Oncol Biol Phys* 37 (), pp. 941–951.

[58] Coderre J.A. and Morris G.M. "The radiation biology of boron neutron capture therapy". In: *Radiation Research* 151 (1999), pp. 1–18.

[59] Horiguchi H. and et al. "Estimation of relative biological effectiveness for boron neutron capture therapy using the PHITS code coupled with a microdosimetric kinetic model". In: *Journal of Radiation Research* 56.2 (2015), pp. 382–390.

[60] Hopewell J.W. and et al. "The radiobiological principles of boron neutron capture therapy: A critical review". In: *Applied Radiation Isotopes* 69 (2011), pp. 1756–1759.

[61] Seppala T. and et al. "Dose planning with comparison to in vivo dosimetry for epithermal neutron irradiation of the dog brain". In: *Medical Physics* 29 (2002), pp. 2629–2640.

[62] ICRU Report 46. *Radiation Dosimetry: Electron, Photon, Electron, Proton and Neutron Interaction Data for Body Tissues*. International Commission on Radiation Units, 1992.

[63] Kankaanranta L. and et al. "Boron neutron capture therapy in the treatment of locally recurred head and neck cancer: final analysis of a phase I/II trial." In: *Int J Radiat Oncol Biol Phys* 82 (2012), pp. 67–75.

[64] Briemeister J.F. "MCNP, a general Monte Carlo N-particle transport code". In: *Los Alamos National Laboratory* ReportLA-12625-M. (1997).

[65] Shirley Lehnert. *Radiosensitizers and radiochemotherapy in the treatment of cancer*. CRC Press, 2014.

[66] Prof Bonner J.A. and et al. "Radiotherapy plus cetuximab for locoregionally advanced head and neck cancer: 5-year survival data from a phase 3 randomised trial, and relation between cetuximab-induced rash and survival". In: *The Lancet Oncology* 11.1 (2010), pp. 21–28.

[67] Butson M.J. and et al. "Radiochromic film for medical radiation dosimetry." In: *Materials Science and Engineering* 41 (2003), pp. 61–120.

[68] Karellas A. and Thomadsen B.R. *Radiochromic film: Role and applications in radiation dosimetry.* Ed. by Indra J. Das. 1st ed. CRC Press, 2017.

[69] Ashland. *Gafchromic radiotherapy films*. 2017. URL: http://www.gafchromic.com/gafchromic-film/radiotherapy-films/EBT/index.asp.

[70] Recommendations of AAPM Radiation Therapy Committee Task Group No. 55. AAPM Report No. 63. "Radiochromic Film Dosimetry". In: *Medical Physics* 25.11 (1998), pp. 2093–2115.

[71] Ashland. *Gafchromic EBT3: Scan handling guide*. P/N AM0191, 3/12, Rev 0.

[72] Micke A. and et al. "Multichannel film dosimetry with nonuniformity correction". In: *Medical Physics* 38.5 (2011), pp. 2523–2534.

[73] Devic S. et al. "Reference radiochromic film dosimetry: Review of technical aspects". In: *Physica Medica* 32 (2016), pp. 541–556.

[74] National Institutes of Health. *ImageJ: Image processing and analysis in Java*. 2004. URL: https://imagej.nih.gov/ij/.

[75] CERN. *ROOT: Data analysis framework.*

[76] PTW. *Dosimetry solutions for radiation therapy*. 2017. URL: http://www.ptw.de/acrylic_and_rw3_slab_phantoms0.html.

[77] Sipila P. and et al. "Gafchromic EBT3 film dosimetry in electron beams: Energy dependence and improved film read-out". In: *Journal of Applied Clinical Medical Physics* 17.1 (2016), pp. 360–373.

[78] Dreindl R. and et al. "Radiochromic film dosimetry: Considerations on precision and accuracy for EBT2 and EBT3 type films". In: *Journal of Medical Physics* 24.2 (2014), pp. 153–163.

[79] Campajola L. and et al. "Absolute dose calibration of EBT3 Gafchromic films". In: *Journal of Instrumentation* 12.8 (2017), pp. 1–10.

[80] Apfel A.E. "The superheated drop detector". In: *Nuclear Instruments and Methods* 162 (1979), pp. 603–608.

[81] Bubble Technology Industries Inc. *Instruction manual for the bubble detector*. Ontario, Canada: Chalk River. 1992.

[82] Portal G. and Dietze G. "Implications of new ICRP and ICRU recommendations for neutron dosimetry". In: *Radiation Protection Dosimetry* 44.1-4 (1992), pp. 165–170.

[83] Curzio G. and et al. "Sensitivity Threshold control in Superheated Drop (Bubble) detectors". In: *LNL Annual Report 1992* LNL-lNFN Rep-72/93 (1993), pp. 116–117.

[84] *Nuclear Decay Data for Dosimetric Calculations*. ICRP Publication 107, 2008.

[85] *Radionuclide Transformations - Energy and Intensity of Emissions*. Vol. 3. 11-13. ICRP Publication 38, 1983.

[86] Spurny F. and et al. "Bubble damage neutron detectors response in some reference neutron fields". In: *Radiation Protection Dosimetry* 65 (1996), pp. 393–396.

[87] Vanhavere F. and et al. "Testing the temperature compensated BD-PND bubble detector". In: *Radiation Protection Dosimetry* 65.1-4 (1996), pp. 425–428.

[88] Vanhavere F. and et al. "The Life Span of the BD-PND Bubble Detector." In: *Radiation Protection Dosimetry* 85 (1999), pp. 27–30.

[89] *Tissue Substitutes in Radiation Dosimetry and Measurement*. Vol. 23. 1. ICRU Report 44, 1989.

[90] RDS Radiology support devices. *Alderson phantoms*. 2014. URL: http://www.rsdphantoms.com/rt_art.htm.

[91] Tutt P. and Adler D. *Anthropometric Data, in New Metric Handbook*. Ed. by Oxford. The Architectural Press, 1979.

[92] Trimble Inc. *SketchUp: 3D modeling for everyone*. URL: https://www.sketchup.com/it.

[93] Zanini A. Durisi E. Visca L. Fasolo F. and Perosino M. "An anthropomorphic tissue equivalent phantom for internal radiation dosimetry." In: *IAEA, INIS Colletion* 35.50 (2004).

[94] *The Fluka web site*. URL: http://www.fluka.org/fluka.php.

[95] *The Geant4 web site*. URL: http://geant4.cern.ch..

[96] Burn K.W. Ongaro C. and Zanini A. "MCNP4B-GN, Monte Carlo Code System for (gamma,n) production and transport in high-Z materials". In: *International Atomic Energy Agency (IAEA), INIS Colletion* 40.26 (2004).

[97] Nelson W.R. and October 1995. et al. . SLAC-PUB-95-6764. "Calculation of the Giant Dipole Resonance Photoneutrons using a coupled EGS4-MORSE code". In: *SLAC-PUB-95-6764* (1995).

[98] Gudowska I. Brame A. Gudowski P. and Kierkegaard J. "Calculation of absorbed dose and biological effectiveness from photonuclear reactions in a bremsstrahlung beam of end point MeV." In: *Physics in Medicine and Biology* 44 (1999).

[99] Allison J. and et al. "Geant4 Developments and Applications," in: *IEEE Trans Nucl. Sci.* 53.1 (2006), pp. 270–278.

[100] Agostinelli S. and et al. "Geant4 - a simulation toolkit". In: *Nuclear Instruments and Methods in Physics Research, Section A: Accelerators, Spectrometers, Detectors and Associated Equipment* 506.3 (2003), pp. 250–303.

[101] *Geant4: Introductory Course*. URL: https://geant4.web.cern.ch/support/training_courses.

[102] *Absorbed Dose Determination in External Beam Radiotherapy: An International Code of Practice for Dosimetry based on Standards of Absorbed Dose to Water*. Vol. TRS-398. International Atomic Energy Agency IAEA, 2000.

[103] D'Errico F. Luszik-Bhadra M. Nath R. Siebert B.R.L. and Wolf U. "Depth dose-equivalent and effective energies of photoneutrons generated by 6-8 MV x-ray beams for radiotherapy". In: *Health Physics* 80 (2001), pp. 4–11.

[104] Hashemi S. M. Bijan H. Gholamreza R. Pervaneh S. Sharafi A. and Jafarizadeh M. "The effects of field modifier blocks on the fast photoneutron dose equivalent from two high-energy medical linear accelerator". In: *Radiation Protection Dosimetry* 128 (2008), pp. 359–362.

[105] Costa M. Durisi E. Monti V. Bedogni R. Alikaniotis K. Giannini G. and et al. "Intense thermale neutron fields from a medical-type LINAC: The e-LiBANS project". In: *Radiation Protection Dosimetry* 180.1-4 (2018), pp. 273–277.

[106] Bevilacqua R. Giannini G. Longo F. Vallazza E. Zanini A. and et al. "PhoNeS: A novel approach to BNCT with conventional radiotherapy accelerators". In: *Nuclear Instruments and Methods in Physics Research, Section A: Accelerators, Spectrometers, Detectors and Associated Equipment* 572 (2007), pp. 231–232.

[107] Giannini G. Zanini A. et al. *PhoNeR: Photo Neutron Radiotherapy*. 2004.

[108] Dawod T. Rostom Y. Abouzeid M. and Mosad M. "IMRT Commissioning and Verification Measurements on Siemens (ARTISTE) Linear Accelerator". In: *Journal of Clinical Oncology and Nuclear Medicine* 8.1-2 (2012), pp. 18–25.

[109] Caccia B. Andenna C. Cirrone G. "MedLinac2: a GEANT4 based software package for radiotherapy." In: *Annals of Istituto Superiore di Sanità* 46.2 (2010), pp. 173–177.

[110] Khue P.D. Loat V.B. "Determination of the 15 MeV bremsstrahlung spectrum from thin W target on the microtron MT-17 accelerator". In: *VNU Journal of Science: Mathematics - Physics* 24.2 (2008).